Titre: Title:	Numerical Simulations of Blood Flow in the Left Heart Hemodynamics
Auteur: Author:	Seyedsharifaldin Shahabi
Date:	2025
Type:	Mémoire ou thèse / Dissertation or Thesis
Référence: Citation:	Shahabi, S. (2025). Numerical Simulations of Blood Flow in the Left Heart Hemodynamics [Master's thesis, Polytechnique Montréal]. PolyPublie. https://publications.polymtl.ca/71956/

POLYTECHNIQUE MONTRÉAL

affiliée à l'Université de Montréal

Numerical Simulations of Blood Flow in the Left Heart Hemodynamics

SEYEDSHARIFALDIN SHAHABI

Département de génie mécanique

Mémoire présenté en vue de l'obtention du diplôme de *Maîtrise ès sciences appliquées*

Génie mécanique

Décembre 2025

POLYTECHNIQUE MONTRÉAL

affiliée à l'Université de Montréal

Ce mémoire intitulé :

Numerical Simulation of Blood Flow in the Left Heart Hemodynamics

présenté par **Seyedsharifaldin SHAHABI**

en vue de l'obtention du diplôme de *Maîtrise ès sciences appliquées*

a été dûment accepté par le jury d'examen constitué de :

Sébastien LECLAIRE , président
Delphine PÉRIÉ-CURNIER, membre et directrice de recherche
Bianca VIGGIANO, membre

DEDICATION

First, I would like to thank my supervisor, Delphine Perie-Curnier for her unwavering guidance and support. I learnt a lot by working under your supervision.

My sincere thanks also go to Zahra Mahboodi, who shared some of my difficulties as a research student. You were by my side during some of the most difficult times of my life, both personal and educational.

I also want to thank my friends: Yazdan, Alireza, Soroush, Sobhan, and Atefeh. Your support helped me through some of the darkest times of my life, and without your presence, I would never have made it this far.

Many thanks go to my cousins Dr. Faezeh Sabri (PhD), Dr. Farhad Sabri (PhD), and his wife Dr. Negar Roshan (DDS). Your support and guidance during the tough times of immigration and adjusting to life as a newcomer in Canada have been invaluable.

The presence of one of the most important role models in my life, my only brother, friend, and supporter, Mr. Shahab Shahabi, should not go unnoticed. I have always felt safe because of your unconditional love and support. You are the reason I chose the field of engineering. Missing your wedding ceremony is, by far, the greatest pain I have experienced in my life. I could never repay the sacrifices you have made for me. I wish all the best for you and your wife, Dr. Mahla Alizadeh.

Last but not least, I would like to thank my parents, Dr. Ali Shahabi (PhD) and Farahnaz Araghi. There are no words to describe your importance in my life. I am the luckiest to have you both in my life, and I hope to make you proud. The best moments of my life are those when I feel that you are proud of me. I want you to know the tears you shed at the airport watered my ambition.

RÉSUMÉ

Le monde est confronté aux maladies cardiovasculaires (MCV), principales causes de mortalité. Ainsi, la détection précoce des anomalies de la fonction cardiaque devient essentielle pour réduire les taux de décès et de morbidité. Le système des cavités gauches du cœur, comprenant l'oreillette gauche (OG), le ventricule gauche (VG) et la valve mitrale (VM), constitue le principal élément de la circulation systémique tout en étant le plus exposé au risque de dysfonctionnement. Cette région manifeste précocement des signes de modifications hémodynamiques, ce qui fait de l'analyse des écoulements une méthode diagnostique essentielle avant l'apparition de symptômes cliniquement perceptibles.

Cette recherche met en œuvre un système computationnel destiné à étudier les profils d'écoulement sanguin dans le cœur gauche à partir de modèles cardiaques spécifiques aux patients, dérivés d'images d'imagerie par résonance magnétique cardiaque (IRM). Le modèle de simulation combine un modèle à paramètres concentrés et un solveur CFD à géométrie prescrite afin d'analyser les profils d'écoulement dans les ventricules et les oreillettes tout au long du cycle cardiaque complet. La méthode permet de calculer plusieurs paramètres hémodynamiques, incluant les profils de vitesse, les cartes de pression, le cisaillement pariétal (WSS) et la dynamique des tourbillons.

Le modèle proposé a été appliqué à des données IRM issues d'un sujet sain au repos, en utilisant Segment Medviso et MATLAB pour réaliser la segmentation et la reconstruction. L'utilisation d'équations paramétriques a permis d'améliorer la forme des cavités cardiaques, tandis que la méthode de couplage a assuré la cohérence entre la circulation systémique et le fonctionnement local des cavités. Les résultats obtenus par la simulation concordent avec les données expérimentales et numériques documentées dans des études antérieures.

L'étude a révélé les différences de profils d'écoulement entre les phases systolique et diastolique, notamment par l'observation des tourbillons dans le VG et l'impact de la contraction auriculaire sur le remplissage ventriculaire. La simulation a produit des résultats conformes aux plages physiologiques normales pour les mesures de pression et de vitesse, tout en mettant en évidence des profils de WSS et de vorticité en accord avec les valeurs de référence établies. L'analyse de sensibilité a démontré la robustesse du processus de segmentation et de reconstruction tout au long de l'étude.

Ce travail démontre le potentiel de la combinaison entre la reconstruction basée sur l'imagerie et la modélisation CFD pour l'évaluation non invasive de l'hémodynamique du cœur gauche. En offrant une analyse détaillée des profils d'écoulement, ce cadre constitue une base pour la détection précoce du remodelage pathologique et contribue au développement d'outils diagnostiques personnalisés. De futures extensions pourraient inclure des simulations dans des conditions d'effort ainsi que l'intégration de modèles d'interaction fluide-structure à plus haute fidélité.

ABSTRACT

Cardiovascular diseases (CVD) are the world's leading cause of death, so improving early-stage detection of cardiac function abnormalities is essential for reducing mortality and morbidity. The left heart (LH) system, consisting of the left atrium (LA), the left ventricle (LV), and the mitral valve (MV), is a key component of systemic circulation and is particularly vulnerable to dysfunction. This region often shows early dynamic changes in hemodynamics, making flow analysis important for clinical assessment before visible symptoms appear in patients.

We use a computational system to investigate left heart blood flow patterns by building individual patient heart models from cardiac magnetic resonance imaging (MRI) data. The model combines a lumped parameter model with a prescribed-geometry computational fluid dynamics solver to study blood flow patterns in both the ventricles and atria over the full cardiac cycle. This approach allows the analysis of several hemodynamic parameters, including velocity patterns, pressure mapping, wall shear stress (WSS), and vortex dynamics.

The proposed model was applied to MRI data from a resting healthy participant, using Segment Medviso and MATLAB to perform the segmentation and reconstruction steps. Parametric equations were used to improve the chamber shapes, while the coupling method maintained proper connections between systemic circulation patterns and local chamber operations. The simulation results matched experimental and numerical data reported in previous studies.

The study showed how blood flow patterns differ between systolic and diastolic periods through observations of LV vortices and how atrial contractions affect ventricular filling. The simulation produced results within normal physiological ranges for pressure and velocity, and the WSS and vorticity patterns agreed with established benchmarks. The sensitivity analysis demonstrated that the segmentation and reconstruction process remained stable throughout the analysis.

This work demonstrates the potential of combining imaging-based reconstruction with CFD modeling for non-invasive assessment of left heart hemodynamics. By offering detailed insights into flow patterns, the framework provides a foundation for early detection of pathological remodeling and contributes to the development of personalized diagnostic tools. Future extensions may include simulations under exercise conditions and integration with higher-fidelity fluid–structure interaction models.

TABLE OF CONTENTS

DEDICATION III

RÉSUMÉ IV

ABSTRACT VI

LIST OF TABLES IX

LIST OF FIGURES X

LISTE OF SYMBOLS AND ABBREVIATIONS XII

CHAPTER 1 INTRODUCTION 1

CHAPTER 2 LITERATURE REVIEW 3

2.1 Cardiac Physiology 3

2.1.1 Anatomy and the Cardiac Cycle 3

2.1.2 Hemodynamic Parameters 5

2.1.3 Characteristic of Blood Flow 8

2.2 Cardiac Magnetic Resonance Imaging 9

2.2.1 Conventional MRI 9

2.2.2 Multi-Parametric MRI 10

2.2.3 Cine MRI 10

2.2.4 Tagging and Phase-Contrast MRI 11

2.2.5 Blood flow Within the Heart 11

2.3 Acquiring Left Ventricular Hemodynamics 13

2.3.1 Numerical Model of Blood Flow in the Left Ventricle 14

2.3.2 Applications of Numerical Methods in Left Ventricular Hemodynamics 18

2.4 Modeling Left Atrium Hemodynamics 23

2.5 Lumped Parameter Model 26

2.5.1 Lumped Parameter Modeling of the Circulation....26
2.5.2 Time-Varying Elastance Modeling....29
CHAPTER 3 OBJECTIVES....32
CHAPTER 4 METHODOLOGY....34
4.1 Geometry Acquisition....34
4.2 Lumped Parameter Modeling....36
4.2.1 Assumptions....38
4.3 CFD Simulation....40
4.3.1 Governing Equations....44
4.3.2 Numerical Implementation....45
4.4 Coupling Strategy....47
CHAPTER 5 RESULTS....49
5.1 Solver Validation....49
5.2 Simulation Results....51
5.2.1 Geometrical Analysis....51
5.2.2 LMP Results....53
5.2.3 CFD Results....57
5.3 Sensitivity Study....66
5.4 Validation....69
CHAPTER 6 DISCUSSION....76
6.1 Choice of Modeling Approach....76
6.2 Limitations of the Study....77
CHAPTER 7 CONCLUSION....80
REFERENCES....83

LIST OF TABLES

Table 2.1 Reference Cardiac Physiological Values 8

Table 2.2 MRI sequences for blood flow analysis 12

Table 2.3 Hemodynamics analysis literature review 20

Table 2.4 Lumped parameter literature review 29

Table 5.1 Used parameters in Womersley problem 49

Table 5.2 Geometrical Parameters 52

Table 5.3 Summary of mesh configurations used in the grid-independence study 68

Table 5.4 Comparison of peak vortex intensity with literature 74

Table 5.5 Comparison of key hemodynamic parameters with Fyrenius et al. 75

LIST OF FIGURES

Figure 2.1 Cross sectional view of the heart shows the normal direction of the blood flow. Taken from [9] 4

Figure 2.2 Wiggers diagram in a healthy subject. Taken from [11] 6

Figure 2.3 Pressure-volume loop during the cardiac cycle. (1) End of systole and beginning of diastole: the heart relaxes at a constant volume (isovolumetric relaxation), and the pressure decreases until reaching point (2). The mitral valve opens, and the ventricle 7

Figure 4.1 Workflow of patient-specific geometry extraction and MATLAB-based reconstruction 35

Figure 4.2 Flowchart of Lumped parameter modeling 40

Figure 4.3 Examples of applied mesh 42

Figure 4.4 Flowchart of CFD simulation 43

Figure 4.5 Flowchart of coupling strategy 48

Figure 5.1 Results of CFD solver in Womersley problem 51

Figure 5.2 Results obtained from LPM (for LV) 53

Figure 5.3 Results obtained from LPM (for LA) 56

Figure 5.4 Temporal variations in velocity, pressure, WSS, and vorticity within LH Chambers 58

Figure 5.5 Contour maps of fluid dynamic metrics in the LV (t = 70 ms to t = 700 ms) 60

Figure 5.6 Evolution of intraventricular streamlines showing vortex formation during diastolic filling 61

Figure 5.7 Left Atrium Hemodynamic and Temporal Analysis 62

Figure 5.8 Contour maps of fluid dynamic metrics in the LV (t = 0 ms to t = 633 ms) 64

Figure 5.9 Mesh independence study for Left Ventricle (LV) simulations 67

Figure 5.10 Comparison of the inlet and outlet flow conditions (evolution of the average velocity over time). The figure on the left is the simulated result of Bedoux [136], the middle figure is results of 4D MRI and figure in the right, is the result of this study..... 71

Figure 5.11 Temporal comparison of maximum WSS: this study (left) versus 4D MRI (right) .. 72

Figure 5.12 Comparison of WSS spatial distribution maps between 4D MRI (left), Study of Bedoux et al. [136] (middle and this study (right)..... 73

LISTE OF SYMBOLS AND ABBREVIATIONS

The list of acronyms and abbreviations presents, in alphabetical order, the acronyms and abbreviations used in the thesis and their meaning. Examples:

CFD Computational Fluid Dynamics

CMR Cardiac Magnetic Resonance Imaging

CVD Cardiovascular Diseases

EDV End-diastolic volume

ESV End-systolic volume

LA Left Atrium

LH Left Heart

LV Left Ventricle

LPM Lumped Parameter Model

MRI Magnetic Resonance Imaging

MV Mitral Valve

PV Pressure Volume

SV Stroke Volume

WHO World Health Organization

CHAPTER 1 INTRODUCTION

World Health Organization (WHO) estimates that cardiovascular diseases (CVD) are accounted for 31% of global death in 2023, making it the leading cause of mortality worldwide. In Canada, heart failure affects approximately 20% of the population and effect the country's economy by more than 22 billion dollars each year [1]. It is the leading cause of hospitalization and a major cause of death, with more than 20,000 cases reported annually. Thus, early detection and appropriate management of individuals suffering from cardiovascular diseases or those at high risk is extremely important. A condition in which the heart is unable to meet the body's demands is called heart failure. Triggered by muscle or valve dysfunction, heart failure can ultimately lead to the patient's death. Early detection and treatment of CVD can assist lower the disease's high death and morbidity rates. To improve our understanding of the cardiac physiological phenomena and processes that contribute to the development and progression of different CVDs, it is essential to develop appropriate investigative tools. The formation of the circulatory system during the embryonic stage, as well as any later changes in its structure or function after birth, depends strongly on flow-induced, or hemodynamic, loads [2]. In this context, numerical models have been increasingly developed to study intraventricular flow. These models, which are sometimes patient-specific, provide the benefit of improved temporal and spatial resolution. By improving our understanding of blood flow, they highlight common hemodynamic phenomena across individuals, which is helpful for identifying reliable diagnostic markers such as pressure gradients or the development of recirculation during ventricular diastole [3]. Unfortunately, if these models become too complex in terms of data specificity or the computational resources required, their usability for statistical studies or as clinical tools becomes significantly limited. The thesis presented here aims to model the left heart using Computational Fluid Dynamics (CFD) to create a model that helps and give doctors valuable insights into the risk factors for the disease. The left side of heart is the powerhouse of circulation and is responsible to pump oxygenated blood into aorta and, consequently to muscles, organs, and tissues and thus works under higher pressure then the right side of the heart [4]. The most dangerous heart failures occur in this region. It is consistent of Left Atrium (LA), Left Ventricle (LV), and Mitral Valve (MV) which connects LA to LV. In patients with heart failure, cardiac wall remodeling is observed, along with changes in its mechanical properties.

For example, an increase in the stiffness of left ventricular cardiac tissue in the presence of heart failure, associated with diastolic dysfunction was investigated by Liu and Wang (2019) [5] and Roe et al. (2017) [6]. However, these symptoms often become apparent only once heart failure is already established, making them unsuitable for early diagnosis.

The long-term hypothesis motivating this research is that early pathological remodeling of the cardiac wall and alterations in cardiac function, before the onset of clinical symptoms, may lead to measurable changes in blood flow patterns within the heart chambers, particularly in the left heart. Such remodeling effects could become more apparent during physical exertion, when cardiovascular adaptation is more demanding and closely linked to cardiac health. However, in this study, the object is not to validate this physiological hypothesis directly, but to develop and evaluate a computational method capable at analyzing blood flow inside the left heart at rest. The hypothesis for this study is that the proposed modeling and analysis framework can accurately reproduce physiologically realistic flow fields and quantify key hemodynamic parameters, such as velocity distribution, vortex structures, and wall shear stress, that are sensitive to morphological and functional variations in the left heart.

First, a literature review on the topic will be presented on Chapter 2, followed by an outline of the scientific approach adopted in this thesis and its objectives. Next on Chapter 3, a patient specific model will be described which is used for the results of this study. The following chapter will describe the various steps taken to develop a numerical model with a prescribed geometry, enabling patient-specific modeling of blood flow in the left ventricle. Finally, a comprehensive discussion of the obtained results will be provided before concluding.

CHAPTER 2 LITERATURE REVIEW

This chapter provides the context for studying hemodynamic flow in the left ventricle. It first presents an overview of cardiac physiology, with a particular focus on cardiac anatomy, the hemodynamic parameters that characterize heart function, and the specific features of blood flow in the left heart. The second part addresses the use of Cardiac Magnetic Resonance Imaging (CMR) for cardiac structure analysis. It begins with an explanation of how CMR works and a description of the acquisition sequences relevant to this study and to blood flow analysis, then reviews its applications in the early diagnosis of heart failure. Finally, the last section examines approaches for modeling cardiac hemodynamics using a numerical model of the left heart.

2.1 Cardiac Physiology

To begin, it is necessary to review the characteristics of the biological structure of the cardiovascular system. The literature review in this study is divided into three parts. First, a detailed overview of the heart's structure and the phases of the cardiac cycle is presented (Anatomy and the Cardiac Cycle). Next, the key physiological indicators used to assess heart function are examined (Hemodynamic Parameters). Finally, the way blood circulates within the heart is discussed, with a focus on flow patterns in the left heart (Characteristics of Blood Flow in the Heart).

2.1.1 Anatomy and the Cardiac Cycle

The heart is a complex vital organ that acts as a pump, driving blood through the body to supply organs and tissues with oxygen and nutrients and to remove waste products [7]. This muscular organ is located in the center of the chest cavity, between the two lungs, within the mediastinum [8]. It is divided into two parts: the right heart, which is responsible for pulmonary circulation, and the left heart, which is responsible for systemic circulation [7]. Working together as a single structure, these two sides ensure synchronized blood circulation and the continuous delivery of oxygen and nutrients throughout the body. Each of these two sections consists of an atrium (Figure 2.1) the upper chamber connected to the venous system, and a ventricle, the lower chamber connected to the arterial system, separated by an atrioventricular valve. The atrioventricular valves have an anatomical structure composed of papillary muscles and chordae tendineae that connect them to the ventricular wall, preventing blood from flowing back into the atria. The aortic and pulmonary valves separate the ventricles from the arteries and do not have this anti-reflux

mechanism; instead, pressure variations during the cardiac cycle prevent blood from flowing back into the ventricles. The mitral valve is characterized by its two leaflets (bicuspid valve), while the other three valves have three leaflets (tricuspid valves). The septum separates the right and left ventricles. Figure 2.1 shows the main cardiac structures mentioned above plus how blood flows inside the heart.

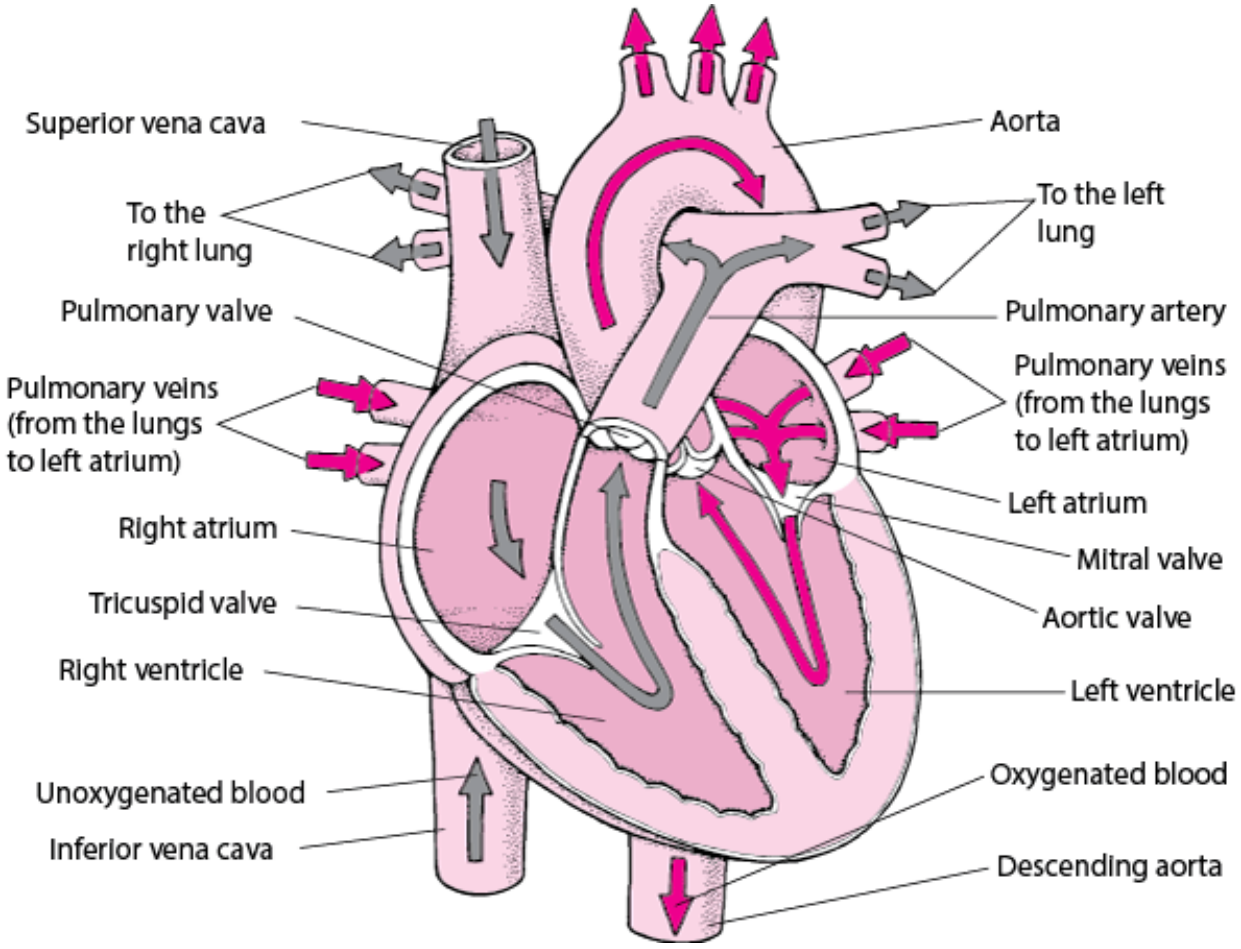

Figure 2.1 Cross sectional view of the heart shows the normal direction of the blood flow. Taken from [9]

The heart wall is composed of three layers, from the outside to the inside: the epicardium, the inner layer of the pericardium; the myocardium, composed of myocytes, the cells responsible for cardiac contraction; and the endocardium, which is in contact with the blood. These three layers are present in the walls of all cardiac chambers but differ in thickness, particularly at the level of the myocardium. The development of the circulatory system's structure during the embryonic stage

and any subsequent changes to its structure or functionality after birth depend heavily on the flow-induced, or hemodynamic, loads [2].

2.1.2 Hemodynamic Parameters

Cardiac hemodynamics refers to the science of the physical properties of blood and its circulation within the heart. From a macroscopic point of view, blood circulation in the heart is defined by phases of ventricular and atrial relaxation and contraction, known respectively as diastole and systole. This entire process is governed by two main phenomena: the contraction and relaxation of cardiac muscle fibers, triggered by electrical impulses, and the resulting pressure variations within the heart chambers. The electrical impulse originates in the sinoatrial node (Figure 2.1), is first conducted through the atria, then relayed by the atrioventricular node (Figure 2.1), and finally transmitted to the myocytes along the septum. This slight delay in conduction allows coordinated contraction of cardiomyocytes, the muscle cells of cardiac tissue, in both the atria and ventricles. The progressive and controlled propagation of the electrical signal ensures efficient ejection of blood from the heart chambers. It is then the pressure difference between the various heart chambers that causes the opening and closing of the heart valves. Figure 2.2 shows the relationship between left ventricular volume, electrocardiogram signals, and pressure, illustrating the different stages of the cardiac cycle in the form of the Wiggers diagram [10].

We can describe the cardiac cycle more precisely using quantitative data. Here, we focus on systemic circulation. At the very end of systole, the ventricle begins to relax while maintaining a constant blood volume, this is called isovolumetric relaxation (c). At this stage, the blood volume is at its lowest and is referred to as the end-systolic volume (ESV). Ventricular diastole then begins, and the ventricle fills progressively, first rapidly in a passive manner (d), then more slowly (e). Finally, the atrium contracts, this corresponds to atrial systole (f), and the ventricle continues to fill until the mitral valve closes and the end-diastolic volume (EDV), which is the maximum blood volume in the ventricle, is reached. The beginning of ventricular systole is characterized by isovolumetric contraction (a), and then, when the ventricular pressure exceeds the pressure in the aorta, the aortic valve opens, and blood is ejected into the aorta (b). The blood volume then returns to a baseline level, and a new cycle begins. The duration of a cycle is determined by the heart rate (beats per minute, or bpm), which decreases with the patient’s age. The stroke volume (SV)

corresponds to the difference between the EDV and the ESV. From this, we can calculate the ejection fraction, which is the SV divided by the EDV. Diastolic and systolic blood pressure in the aorta can be measured using a blood pressure cuff. Cardiac output is calculated by multiplying the stroke volume by the heart rate.

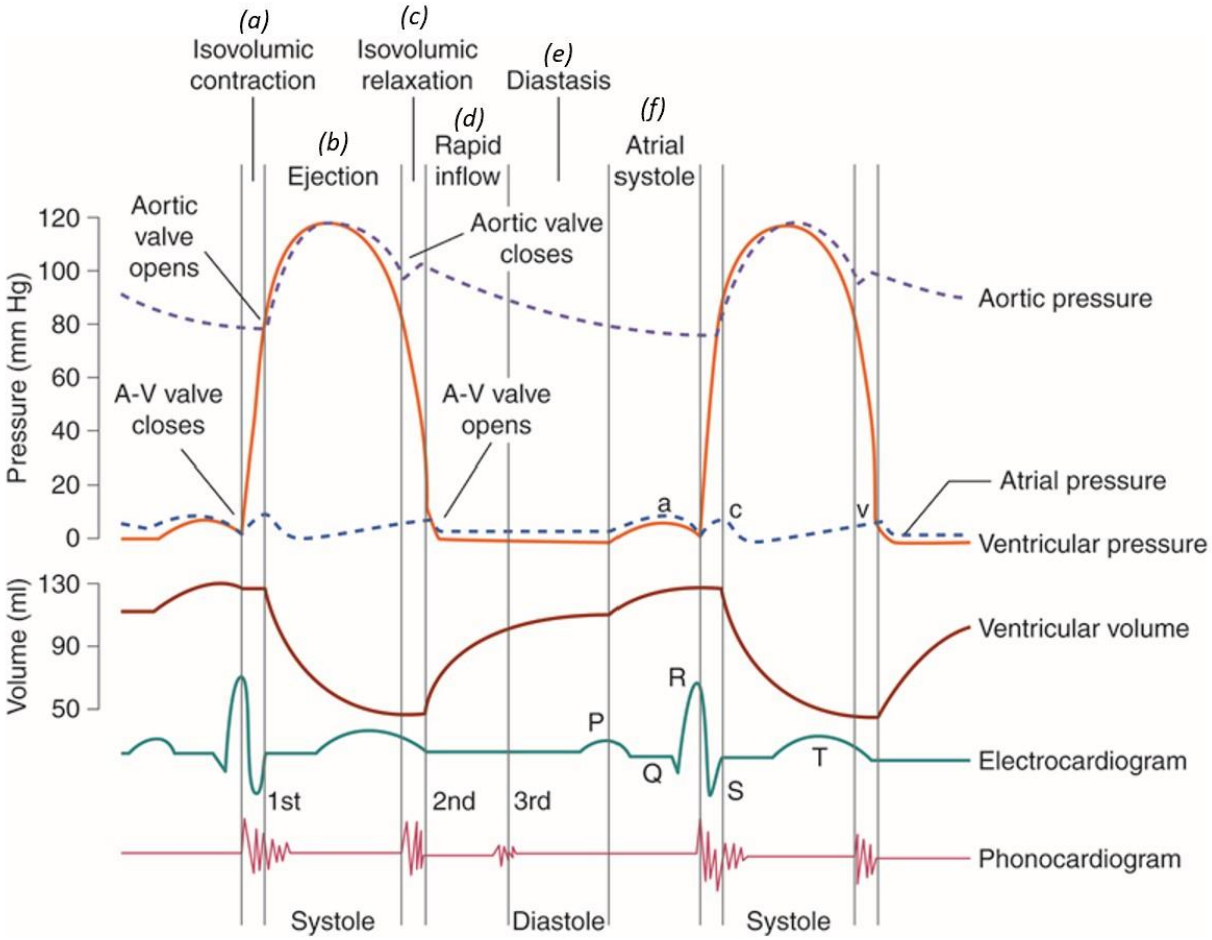

Figure 2.2 Wiggers diagram in a healthy subject. Taken from [11]

The cardiac index (CI) corresponds to the cardiac output divided by the body surface area. Table 2.1 summarizes the reference physiological values for a resting adult human. The volumes are indexed to body surface area. Understanding the evolution of ventricular pressure and volume throughout the cardiac cycle makes it possible to plot a patient-specific pressure volume (PV) curve and to identify preload, afterload, EDV, ESV, and the levels of ventricular compliance and contractility. These various elements are presented in Figure 2.3. Preload is related to SV: increasing preload results in an increase in SV, while decreasing preload leads to a decrease in SV.

Preload follows the end-diastolic pressure-volume relationship (EDPVR). Compliance, the inverse of stiffness, defines a structure's ability to deform under stress. In the case of the ventricle, compliance influences the EDV: increasing compliance increases EDV, which characterizes a positive lusitropic effect. This effect becomes negative when compliance decreases. The inotropic effect, on the other hand, is related to contractility and ESV. A positive inotropic effect leads to an increase in both parameters. Afterload refers to the pressure at EDV. The higher the afterload, the less the ventricle can contract, and the lower the SV will be, its increase is associated with a decline in cardiac performance. Afterload follows the end-systolic pressure-volume relationship (ESPVR).

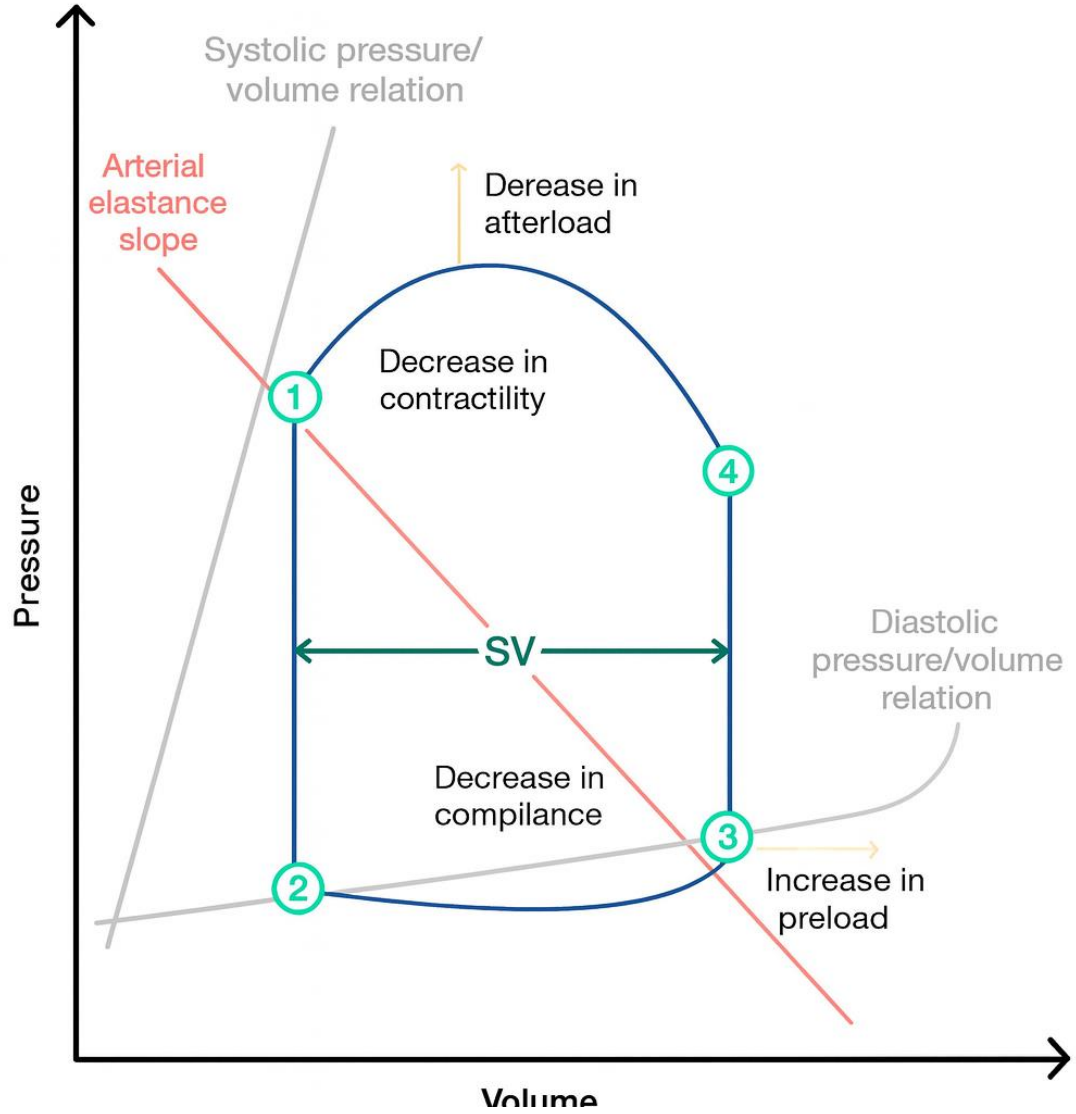

Figure 2.3 Pressure-volume loop during the cardiac cycle. (1) End of systole and beginning of diastole: the heart relaxes at a constant volume (isovolumetric relaxation), and the pressure decreases until reaching point (2). The mitral valve opens, and the ventricle

The stroke work corresponds to the area enclosed by the PV loop, while the potential energy is represented by the area bounded by the end-diastolic and end-systolic pressure-volume relationships, and the upper right end of the PV loop. These two parameters allow for the analysis of cardiac efficiency, which serves as a clinical indicator of heart health.

Table 2.1 Reference Cardiac Physiological Values

Parameters	**Normal physiological values**	**Reference**
Heart Rate	60 to 100 bpm	[12]
EDV	50 to 90 $mL.m^{-2}$	[13]
ESV	18 to 32 $mL.m^{-2}$	[13]
SV	50 to 65 $mL.m^{-2}$	[13]
Ejection fraction	55 to 70%	[14]
Systolic blood pressure	< 120 mmHg	[15]
Diastolic blood pressure	< 80 mmHg	[15]
Cardiac output	5 to 6 $L.min^{-1}$	[16]
Cardiac index	2.5 and 4 5 to 6 $L.min^{-1}.m^{-2}$	[16]

In clinical practice, these hemodynamic parameters are obtained using a variety of diagnostic techniques. Such measurements not only support the diagnosis of cardiovascular disease but also provide physicians with valuable insights into patient-specific risk factors. Section 2.3 discusses more about ways of acquiring hemodynamic parameters.

2.1.3 Characteristic of Blood Flow

The sequence of the different stages shown in Figure 2.3 highlights a blood circulation that depends on synchronized and perfectly controlled phenomena. The characteristics of blood flow within the heart thus serve as particularly valuable indicators of cardiac function [17]. The distribution of pressure curves and velocity fields within the heart chambers, the normal and shear wall stresses, as well as the kinetic study of blood flow (energy transfer and loss) [18], are all variables that

characterize blood flow and can provide valuable information about cardiac health. In healthy subjects, Khalafvand et al. (2015) [18] and Hung et al. (2015) [19] developed a 2D numerical model of the left ventricle based on cardiac MRI, showing that blood flow is optimally transported both during diastole (from the left atrium to the left ventricle) and during systole (from the left ventricle to the aortic sinus). Energy is nearly conserved, with only a 2% energy loss during the diastolic phase. The authors also demonstrate that during both diastole and systole, the work associated with shear stress and energy loss, though minimal, is balanced by optimal contraction and dilation of the ventricle. Moreover, it has been repeatedly suggested that blood flow within the heart plays a crucial role in embryonic heart development [20, 21], cardiac remodeling throughout life [22], and the onset of cardiac pathologies [23-26].

2.2 Cardiac Magnetic Resonance Imaging

Cardiac magnetic resonance imaging (CMR) and echocardiography are preferred medical imaging techniques for diagnosing and monitoring heart diseases. They are also highly valuable for visualizing and studying blood flow within the heart. In this study, we will focus on principle of MRI and the acquisition sequences commonly used in a clinical setting.

2.2.1 Conventional MRI

MRI is a non-invasive, non-radiating analysis tool that provides anatomical, structural, biochemical, and dynamic information. MRI uses the phenomenon of nuclear magnetic resonance to obtain cross-sectional images of the object being examined. This principle is based on the excitation of protons placed in a uniform magnetic field (B0) through electromagnetic pulses of appropriate frequency, delivered on a specific plane. This generates a temporary change in the orientation of the magnetization vectors of the targeted nuclei, also known as the proton spin, along the direction of the magnetic field. As the system returns to equilibrium, or relaxes, it releases energy in the form of characteristic radiofrequency waves, which make up the signal detected by the scanner [27]. This raw signal is stored in K-space, a frequency domain from which two-dimensional images are reconstructed using an inverse Fourier transform. The aim is to obtain sufficient contrast between different tissues to characterize them, while keeping noise, artifacts, and acquisition time as low as possible. To extract information specific to the tissue or fluid being analyzed, predefined sequences of radiofrequency pulses and magnetic field gradients are applied. A sequence consists of radiofrequency excitations, a gradient for spatial encoding (which

determines the encoding in K-space), and acquisition of the resulting signals in that same space. One common sequence is the spin echo MRI sequence, characterized by echo time (TE) and repetition time (TR). This sequence is carried out as follows: a 90-degree radiofrequency pulse is emitted, followed by a 180-degree refocusing pulse halfway through the echo time (TE), with signal readout occurring at TE. This process is repeated at each repetition time (TR), during which one line of K-space is filled using variable phase encoding. Other sequences exist as well, such as fast spin echo sequences, inversion recovery sequences (characterized by the inversion time, TI), and gradient echo sequences [27]. In the case of cardiac MRI, the sequences are regularly synchronized with signals recorded by electrocardiograms (ECG-gated sequences) in order to obtain high-quality images that capture the entire cardiac cycle.

2.2.2 Multi-Parametric MRI

This imaging technique uses different magnetic resonance sequences to identify parameters specific to the tissues being studied. These parameters provide information for morphological analysis (through mapping) and also reflect various biochemical and biomechanical properties of the tissue. The weighted sequences make it possible to measure intrinsic tissue parameters such as longitudinal relaxation time (T1), transverse relaxation times (T2 and T2*), and proton density. The detailed meaning of these parameters is not discussed in this thesis, as they are not explored further. Relationships have been reported between the Young's modulus of bone tissue and combinations of MRI parameters, as well as between relaxation times and the density of trabecular bone tissue [28]. In the heart, these intrinsic MRI-derived parameters help reveal structural changes in cardiac tissue. For example, Huang et al. (2022) [29] found significantly higher native T1 and T2 values in patients with idiopathic inflammatory myopathy compared to healthy subjects. Additional sequences such as diffusion imaging, tractography, perfusion, spectroscopy, and elastography can also be used to assess parameters such as the diffusion tensor, elasticity, biochemical composition, or magnetization transfer of tissues.

2.2.3 Cine MRI

The cine MRI sequence is an imaging technique that is particularly well suited for analyzing organs that undergo cyclical motion and their associated dynamics. It is therefore especially useful for studying the cardiac cycle. It relies on ultra-fast gradient echo sequences and makes it possible to visualize a series of image slices of the organ over time.

2.2.4 Tagging and Phase-Contrast MRI

Tagging consists of imprinting geometric patterns on the tissue before cine MRI acquisition, using spatially selective presaturation pulses. This makes it possible to perform a more detailed motion analysis by tracking the deformation and evolution of these patterns over time.

Phase-contrast MRI, in contrast, is particularly well suited for studying fluid motion, such as blood flow. This technique allows visualization of blood flow and encoding of the velocity fields that characterize the flow, either in the direction perpendicular to the imaging plane or within the plane itself. These sequences are also used to analyze tissue displacement and deformation. 4D flow MRI is based on a similar principle but encodes velocities in all three spatial directions over a given time interval.

2.2.5 Blood flow Within the Heart

MRI is now widely used as a powerful, non-invasive method for assessing intracardiac blood flow dynamics. Wong et al. (2009) [30] proposed a method called Magnetic Resonance Fluid Motion Tracking (MRFMT), which uses steady-state free precession (SSFP) MRI to visualize intracardiac blood flow by analyzing intensity variations caused by turbulent, asynchronous proton spins. Unlike conventional phase-contrast MRI, which directly encodes velocity but requires longer scan times, MRFMT shifts part of the computation to the post-processing stage, allowing faster image acquisition. When applied to patients with atrial septal defects, this technique was able to detect changes in atrial vortex patterns before and after surgical closure, providing a non-invasive tool for assessing flow abnormalities. Although it is less precise than velocity-encoded approaches, MRFMT remains a promising method for rapid assessment and visualization of cardiac flow.

Kilner et al. (2000) [17] used magnetic resonance phase-velocity mapping to identify asymmetrical and chiral blood flow patterns within the human heart, offering insight into how the complex cardiac geometry supports efficient flow redirection. They showed that blood streams entering the atria and ventricles follow sinuous paths, with rotational and asymmetric motion that helps direct flow toward the atrioventricular valves and outflow tracts. These patterns, visualized using 3D and animated streamlines, suggest that cardiac looping and curvature may reduce flow separation, improve ventricular filling, and enhance hemodynamic efficiency, particularly during exercise.

This study highlights the diagnostic value of MRI for analyzing intracardiac flow topology and its functional implications.

Building on these earlier advances, more recent work in cardiac MRI has focused on comprehensive visualization and quantification of blood flow using phase-contrast cine MRI (PC-MRI) and 4D flow MRI. PC-MRI encodes velocity information into phase images, enabling measurement of cardiac output, valve regurgitation, and shunt ratios, while 4D flow MRI extends this principle by acquiring three-directional, time-resolved velocity fields. This technique allows detailed assessment of intracardiac hemodynamics, including vortex formation, turbulence, wall shear stress, and abnormal flow jets linked to valvular or congenital defects. Clinical studies have shown its usefulness in characterizing eccentric flow in bicuspid aortic valves and altered hemodynamics in complex congenital heart disease. By combining functional measures with anatomical imaging, 4D flow MRI has become an important research and diagnostic tool for investigating the relationship between cardiac geometry, blood flow, and disease progression [31].

More reviews on MRI-based blood flow assessment have been conducted and can be found in Table 2.2.

Table 2.2 MRI sequences for blood flow analysis

Sequence	Usage	Characteristics	References
Cine MRI	Velocity fields within the ventricle were estimated from cine images using an optical-flow framework based on the Lucas–Kanade algorithm [32], with performance inherently tied to the sequence's spatial and temporal resolution	Acquisition requires more time than echocardiography, offers limited temporal resolution, and produces only planar data (restricted to the selected slices). As a result, the validity and accuracy of the measurements are constrained and may often be unreliable	[30, 33]
Phase-contrast MRI	Two-dimensional velocity encoding during MRI acquisition provides planar measurements of inflow and outflow across the cardiac	Acquisition time is comparable to cine-MRI, with data restricted to the selected imaging planes. Although temporal resolution remains low, this method generally provides greater validity and	[17, 30, 31]

	chambers, enabling the evaluation of potential intracardiac shunts and the interpolation of local velocity distributions.	accuracy than optical-flow–based approaches.	
4D flow MRI	Velocity encoding is performed in three dimensions during MRI acquisition, producing volumetric datasets that provide detailed information on velocity fields in both space and time.	Acquisition times are relatively long, depending on the desired spatial and temporal resolution. Data quality is strongly influenced by patient compliance, such as maintaining steady respiration and minimizing motion. The method generates three-dimensional datasets but requires complex post-processing.	[31, 34]

These techniques are notably used for the characterization of congenital heart diseases [27, 31, 34], as well as for studying blood flow in the heart of healthy subjects [30, 35]. However, during velocity encoding, the temporal resolution of the acquisition limits more advanced analysis of blood flow. The quality of the acquisition is also affected by the aliasing phenomenon (which occurs when the velocity encoding parameter is set below the maximum velocity in the ventricle), while an excessively high encoding velocity limits the resolution of the velocity field (resulting in low accuracy for slower velocities). Lastly, 4D flow analysis is not suitable for clinical assessment of blood flow during physical exertion, due to the long acquisition time and the requirement to remain still with constant breathing for several tens of minutes.

2.3 Acquiring Left Ventricular Hemodynamics

The most reliable diagnostic tool for cardiomyopathies is cardiac catheterization for performing an endomyocardial biopsy, in order to perform a histological study, and the measurement of intracardiac hemodynamic parameters (pressure gradients, blood velocity, and cardiac output). However, this tool is limited because it is expensive, invasive, and sometimes risky for the patient, and often unavailable [36]. Non-invasive medical imaging methods like echocardiography (ECG), magnetic resonance imaging (MRI), and computed tomography (CT) are another strong set of clinical cardiovascular assessment tools. These methods can provide important information about the heart without the risks associated with traditional clinical tools. However, despite the

widespread use of medical imaging technologies, there are still limitations and challenges in the prognosis and detection of heart pathologies in clinical practice. For example, many essential hemodynamic features of blood flow patterns that are useful for the early detection of CVD cannot be obtained from computed tomography (CT) [37]. The spatiotemporal resolution of magnetic resonance imaging (MRI) is sufficient to capture small-scale and time-resolved hemodynamic properties of the heart. Three-dimensional (3D) flow evolution over the cardiac cycle can be visualized using 4D MRI, a state-of-the-art technique that combines 3D velocity-encoded phase contrast with 3D spatial encoding [38]. With spatial and temporal resolutions of 2–3 mm and 40–50 ms, respectively, these scans are relatively long, typically lasting around 20 minutes or more. A significant limitation of 4D MRI, however, is its inability to accurately capture certain hemodynamic parameters, such as wall shear stress (WSS), due to its low resolution [39], even though computational fluid dynamics (CFD) simulations can estimate these quantities with sufficient accuracy. When assessing heart function, CFD is often used together with invasive clinical instruments and medical imaging techniques. CFD can provide detailed hemodynamic information that is useful for the early detection of heart failure and for clinical evaluation of cardiac performance [40]. CFD is a computational technique that models fluid flow, such as blood flow in the cardiovascular system, using computer simulations and mathematical algorithms. For the purpose of diagnosing and treating cardiovascular disorders, CFD can offer comprehensive information on blood flow patterns, velocity, pressure, and other factors. Because biological systems have non-rigid limits, CFD models of biological systems are difficult. Similar to cardiac hemodynamics, the forces exerted on these borders by the movement of the surrounding fluid are what move them [41]. Since reduced myocardial contractility is linked to abnormal left ventricle (LV) flow patterns, which prevent the heart from ejecting enough cardiac output to cause heart failure (HF), it is thought that early cardiac dysfunction can be identified by examining the hemodynamics within the LV chamber [42].

2.3.1 Numerical Model of Blood Flow in the Left Ventricle

A numerical model is fundamentally based on a mathematical model that describes the real phenomenon of interest. The equations that characterize fluid flow within a given structure are the continuity equation (or conservation of mass) and the Navier–Stokes equations (which represent the conservation of momentum and energy). Computational fluid dynamics (CFD) for the study of

blood flow most commonly relies on the finite volume method (FVM), which ensures local conservation of the aforementioned quantities.

Bellhouse [43] first examined blood flow dynamics in the left ventricle in 1970, sparking the first attempts to investigate LV hemodynamics and many other studies followed this path [44]. However, The Computational Fluid Dynamic (CFD) simulation of the blood flow in the heart has advanced significantly in recent years and has become a vital tool for studying heart function [45]. In these studies, three broad categories can be used to categorize CFD approaches to cardiac flow simulation: geometry prescribed CFD methods, finite volume method (FVM), fictitious fluid structure interaction (FSI) methods, and realistic FSI methods.

Geometry Prescribed CFD Methods

The geometry prescribed technique simulating problems on prescribed boundaries or predefined moving meshes made mostly using MRI/tomography or computerized tomography data is a one-way strategy that ignores the fluid's contribution to the structure. The inner ventricular wall's movement is used as a boundary condition in this method, which alone solves the fluid domain. Simply expressed, this type of CFD approach is known as Image-Based CFD (IB-CFD) or geometry prescribed methods if patient-specific real-time data is employed as input for numerical simulations. In this method, the geometry of the heart chamber, which represents the boundary of the fluid domain, can be obtained in various ways. One method involves modeling a simplified structure of the heart. This geometry can, for example, be represented as a cone [46], a truncated ellipsoid [47], or an elongated spheroid [48] to study blood flow in the left ventricle. The characteristics of these geometries (length, diameter variation, truncation planes, etc.) can be adjusted to reflect the anatomical features of each patient. These models are relatively simple to implement, as they require creating a single primary geometry that can then be adapted over the cardiac cycle using data extracted from medical imaging. A user-defined formulation in standard simulation software can be used to generate a time-varying geometry that reproduces the cardiac cycle [49]. This simplification also reduces the computational cost of the simulations. However, oversimplifying the anatomy may limit the ability to visualize effects related to doxorubicin-induced cardiotoxicity and may not provide sufficiently detailed information to detect early signs of such toxicity. It also constitutes a highly reductive representation of ventricular anatomy, which requires careful validation of the results obtained.

Another approach is to segment the acquired cardiac images to obtain an accurate model of the heart chamber under study. Once the images are segmented, it is possible to extract the chamber shape throughout the cardiac cycle and perform interpolations to improve temporal resolution. This method is more difficult to implement, as it requires specific expertise in image segmentation (knowledge of cardiac anatomy or access to specialized cardiac image processing software). In addition, during the discretization step, ensuring correspondence between the different temporal meshes is more challenging due to the increased geometric complexity. A structured mesh is therefore better suited to obtaining matching nodes throughout the cardiac cycle [50-52].

Using a dynamic heart phantom, Hvid et al. (2023) [53] evaluated the accuracy of blood flow velocities obtained from a geometry-prescribed computational fluid dynamics (CFD) pipeline. In their study, the experimental setup defined the inlet and outlet conditions, and the motion of the fluid domain was prescribed using volumetric image registration based on Computed Tomography Angiography (CTA) data. To compare vector flow imaging (VFI) with the corresponding planes in the simulated time-dependent three-dimensional velocity field, VFI was systematically measured in parallel planes. Their results showed that, qualitatively, the flow patterns from the CFD simulations and the VFI measurements were similar. A direct comparison of the flow fields also indicated that, in a carefully controlled experimental setting, the proposed CFD pipeline produced realistic flow patterns.

FSI methods

Before FSI methods were introduced to model the cardiovascular system, a framework based on the immersed boundary method was developed. Charles Peskin [76] specifically described this approach for studying blood flow in the heart, with the aim of analyzing the interaction between the ventricular wall and the fluid in more detail. In this method, the ventricular wall is represented by elastic fibers immersed at discrete points within the fluid [54]. The interaction with the fluid is then approximated using interpolation functions based on a Dirac delta distribution. The governing equations of the fluid domain are solved on a Cartesian grid, and the point forces generated by the ventricular walls are treated as fictitious forces whose magnitudes represent physiological conditions. The Arbitrary Lagrangian-Eulerian (ALE) formulation is no longer suitable for simulating fluid dynamics in this context, and the governing equations must be adapted to the

employed method. The fluid is described using Eulerian velocities and a pressure calculated at each element of the mesh.

The advantage of this method is that it uses heart chamber geometries extracted from medical imaging but requires meshing only the Cartesian grid. The boundaries, modeled as elastic fibers, generate forces as they move, which are applied to neighboring nodes in the fluid domain and approximated using functions based on the Dirac delta distribution. This induces fluid motion. The wall velocities are then interpolated from the fluid dynamics using the no-slip condition, and the resulting displacement is computed to update the boundary. This procedure is repeated at each time step to simulate the cardiac cycle [49].

The FSI model is particularly well suited for studying the motion of heart valves, which is mainly governed by fluid movement and pressure variations. However, its limited accuracy in applying boundary conditions, since these are interpolated rather than directly extracted from imaging, restricts its use in clinical settings and for patient-specific analysis [44]. Similar models have been adapted from this method (e.g., immersed objects, curvilinear immersed boundaries), collectively referred to as fictitious fluid-structure interaction models [49].

In the context of cardiac modeling, FSI numerically solves the governing equations of both the fluid (blood) and structure (heart tissue) domains by coupling CFD and structural mechanics solvers. Typically, the fluid dynamics are addressed using the Finite Volume Method (FVM), while the solid mechanics, such as myocardial or valvular deformation, are modeled using the Finite Element Method (FEM). These two domains are then coupled using algorithms that account for the unique material properties of both the blood and cardiac tissues.

FVM consists of dividing the global volume into control volumes. This step introduces a discretization error due to the transformation of the integral forms of the governing equations into algebraic equations at the centers of the control volumes. Since these equations are nonlinear, a linearization error is also introduced. This error depends on the tolerance threshold chosen during the iterative solution of the algebraic equations. Therefore, a convergence study must be conducted, both to assess the impact of discretization (mesh refinement) and to evaluate the acceptable residual error (by reducing the tolerance). In any casdependsolution of these equations depends on the properties of the fluid which in this case is blood, as well as on boundary and initial conditions.

here are two main approaches to FSI: realistic FSI [55] and fictitious FSI [56]. In realistic FSI, separate solvers are used for the fluid and structural domains, allowing detailed and accurate simulation of the coupled system. In contrast, fictitious FSI methods aim to improve numerical stability and convergence by modifying existing solvers. These approaches introduce artificial mass, damping, or pressure terms into either the fluid or structural equations to facilitate coupling.

In cardiac applications, the initial geometry of the heart chambers is usually obtained from medical imaging, either through direct segmentation or by adapting a simplified anatomical model. This geometry is often used as the initial condition for simulating ventricular diastole, the phase during which the ventricle relaxes and fills with blood. Simulating diastole is relatively more straightforward, as it involves a pre-stressed myocardial wall undergoing passive deformation. By contrast, modeling systole, the active contraction phase driven by myocyte activity, is much more complex and requires advanced mathematical models to accurately capture myocardial mechanics. Additionally, matching the simulated wall motion to that observed in imaging data is challenging and often necessitates optimization of the structural model parameters. FSI simulations also require that the software handle convergence studies at every time step. If the model is overly complex or poorly parameterized, this can cause divergence of residuals during iterative solving or substantially increase the computational time required to achieve convergence.

Lopes et al. (2021) [57] qualitatively and quantitatively compared finite element and finite volume approaches for simulating the fluid–structure interaction of blood flow through a real stenosed artery. They found a reasonable overall agreement between the hemodynamic predictions obtained with the two methods. An additional observation was that the finite volume–based software, Ansys, showed higher efficiency in terms of both computation time and memory usage.

2.3.2 Applications of Numerical Methods in Left Ventricular Hemodynamics

To simplify the literature review, and avoid dispersing the reported results, a database was formed based on the following criteria: geometry type, image processing methods, viscosity models, and CFD approaches is conducted.

By combining CFD with medical images, Doost et al. (2017) [58] used image-based computational fluid dynamics (IB-CFD) to evaluate the left ventricle (LV) and proposed a semi-automated method for simulating LV hemodynamics. The model geometry was reconstructed from MRI images of a healthy individual. Their study visualized the formation and propagation of

intraventricular vortices using two physiological time-resolved 2D models of a patient-specific LV, each with a different aortic and mitral valve configuration (orifice-type and integrated rigid leaflets). To assess the effect of valve type on vortex formation, they analyzed the blood flow patterns in both models over the cardiac cycle. The integrated valve model produced intraventricular flow patterns that more closely matched physiological flow and performed better than the orifice-type model in predicting complex flow structures. In this work, blood density and viscosity were assumed to be 1050 kg/m³ and 0.0035 kg/ms, respectively.

In another study, aimed at confirming abnormal flow patterns in diseased hearts, Bavo et al. (2016) [59] used a patient-specific CFD model of the left ventricle and mitral valve, with prescribed moving boundaries derived from transesophageal ultrasound data for three cardiac pathologies. Their results showed that the disease state, ventricular shape, and mitral valve geometry all influence the LV flow field, leading to distinct flow characteristics. The pattern of vortex formation and evolution, which depends on ventricular geometry and valve orifice, was of particular interest. The maximum base-to-apex pressure difference of 2 mmHg was consistent with previously reported values. In their simulations, blood was modeled as a Newtonian, homogeneous fluid with a density of 1060 kg/m³ and a viscosity of 0.0035 Pa·s.

Alharbi et al. (2022) [60] investigated the LV and idealized mitral valve (MV) leaflets in a 3D FSI computational model. The mechanical behavior of the MV leaflets was modeled using an experimentally based hyperelastic isotropic material, and the model also included chordae tendineae and papillary muscle attachment points. Their results showed that the generic LV–MV model could reproduce both normal and prolapsed MV states, as well as physiological leaflet opening and closing driven by time-varying atrial and ventricular pressures. The model was also able to replicate blood flow patterns after implantation of a prosthetic MV, both with and without left ventricular outflow tract flow restriction. The CFD simulation results were compared with echocardiography data for validation.

Based on the pressure difference across the valve, valve opening, and velocity in the flow domain, Christierson et al. (2024) [61] developed an FSI model that simulates five different cases and compares them with in vitro data. Their findings showed that, relative to catheter measurements, the simulations underestimated the transvalvular pressure difference by 6.8–14%. When valve opening was compared with cine MRI, 2D Echo, and 3D Echo data, an underestimation of 5.47–

7.3% was observed. Furthermore, there was an underprediction of 7.9–8.4% in the simulated velocity across the valve as compared to the Doppler Echo data. A qualitative analysis of the ventricle's velocity profile and the domain's streamlines of flow revealed a good degree of concordance between the two flow characteristics. Water with Newtonian characteristics was utilized in this study; its density was 998 kg/m3 and its viscosity was always 1.002 mPas

In another study, based on patient-specific data, Bryon et al. (2023) [62] demonstrated an automated process for simulating left ventricular (LV) flow patterns. The pipeline that is being shown includes phases for preprocessing, CFD simulation, and postprocessing. During these stages, blood was treated as an incompressible Newtonian fluid with a density of 1105 kg/m³ and a constant viscosity of 0.004 kg/ms. Deep learning was used to segment the mitral and LV valves, reducing the amount of manual work required. However, the overestimation of velocity caused by the 2D assumption underlined the need for improved segmentation and more precise measurements. This study represents a step forward in the development of automated 2D patient-specific simulations for cardiovascular evaluation.

The goal of Esfahani et al. (2019) [63] was to model the progression of Mitral Regurgitation (MR) from mild to severe stages. To extract hemodynamic parameters of blood flow during MR in systole, a Fluid–Structure Interaction (FSI) model was developed. Using dimensional measurements obtained from Magnetic Resonance Imaging (MRI), a two-dimensional (2D) geometry of the mitral valve was constructed. The leaflets were assumed to be flexible. Hemodynamic characteristics such as pressure, velocity, and Von Mises stress contours were obtained by moving an arbitrary Lagrange–Euler mesh using COMSOL software. The effects of the unusual spacing between the leaflets on the volume of returning flow were demonstrated by the results. In addition, the measurement of the leaflet deformation during systole was in line with the pertinent literature.

Table 2.3 presents the models described in the literature for hemodynamics analysis along with their specific features and the validation methods used.

Table 2.3 Hemodynamics analysis literature review

Reference	**Geometry Types**	**Imaging Technique**	**Method**	**Viscosity Model**	**Result Validation**

Loke et al. [64]	3D	MRI	FSI	Newtonian	Compared with 4D flow MRI
Kannojiya et al. [65]	3D	CT	CFD	Bird-Carreau Model	N/A
Zuo et al. [66]	3D	N/A	CFD	N/A	Compared with Clinical Echocardiography
Leinan et al. [67]	3D	Transthoracic echocardiography	CFD	N/A	Compared with US and PIV
Zingaro et al. [68]	3D	CT	CFD	N/A	N/A
Xu et al. [69]	2D	CT	CFD	Newtonian	Tomographic PIV
Chen et al. [70]	2D	Dynamic contrast-enhanced ultrasound	CFD	Newtonian	N/A
Lantz et al. [71]	3D	MRI	CFD	N/A	4D flow MRI
Itatani et al. [72]	3D	C/A	CFD	N/A	N/A
Dahl et al. [73]	2D	Ultrasound	FSI	Newtonian	N/A
Long et al. [50]	3D	MRI	CFD	Newtonian	Compared with MRI velocity mapping
Bennati et al. [74]	3D	Cine-MRI	IB-CFD	Newtonian	Compared with echo color Doppler (ECD)
Bennati et al. [75]	3D	Cine-MRI	IB-CFD	Newtonian	N/A

Feng et al. [76]	3D	N/A	FSI	N/A	N/A
Fumagalli et al. [77]	2D	Cine-MRI	CFD	Newtonian	Compared with literature
Miyauchi et al. [78]	2D	MRI	CFD	Newtonian	Compared with 4D Flow MRI
Sacco et al. [79]	3D	MRI	CFD	Newtonian	N/A
Yamada et al. [80]	3D	MRI	CFD	N/A	N/A
Gao et al. [81]	3D	MRI	FSI	N/A	Qualitive comparison with in vivo MRI derived mapping
Imanparast et al. [82]	3D	Cine-MRI	FSI	Newtonian	Compared with MRI velocity, pressure and WSS mapping
Doost et al. [58]	2D	MRI	CFD	Newtonian	N/A
Imanparast et al. [83]	3D	MRI	CFD	Newtonian	N/A
Doost et al. [84]	3D	MRI	CFD	Newtonian	N/A
Boyang et al. [85]	3D	MRI	CFD	Newtonian	N/A
Khalafvand et al. [18]	3D	MRI	CFD	Newtonian	N/A

2.4 Modeling Left Atrium Hemodynamics

The left atrium (LA) is a vital aspect of cardiac physiology as it works passively during ventricular diastole and actively during atrial systole, as it contributes to ventricular filling [86]. Abnormal LA hemodynamics are often associated with a great number of cardiovascular diseases, particularly atrial fibrillation (AF), a specific arrhythmia that is associated with an increased risk of stroke due to potential thrombus creation in the left atrial appendage (LAA) [87].

Numerous numerical studies have been carried out throughout the years to investigate the possible relationship between left intraventricular flow and heart function. Pursuing a deeper comprehension of intraventricular hemodynamics [88]. The mitral valve (MV) was first simplified as an orifice, and an idealized LV (such as a truncated prolate spheroid) was first modeled without the left atrium (LA). Since then, improvements in imaging methods have made it possible to numerically simulate patient-specific research, with the majority of these simulations concentrating on left hearts that are in good health [85, 89]. It has proven difficult to rebuild the LA from standard cardiac magnetic resonance (CMR) images with wide spacing because of its complexity [90]. Furthermore, when the physiological LA is added without the MV, irrational flow patterns may emerge because the intraventricular flow is sensitive to the inlet boundary condition, or atrial flow. In CMR-based numerical studies, a tube-shaped LA is frequently used as a solution, with a uniform or zero normal gradient condition applied at the input.

Recently, there has been a focus on utilizing numerical methods including Computational Fluid Dynamics (CFD), Fluid-Structure Interaction (FSI) and image-based models for their potential to assess left atrial (LA) hemodynamics. Furthermore, when combined with lumped-parameter or electromechanical models, these modeled equations are capable of modeling physiologically and producing pressure-volume relationships, as well as predicting thrombus-prone areas in LAA, especially in atrial fibrillation scenarios [91].

Medical imaging techniques such as computed tomography (CT) and magnetic resonance imaging (MRI) are valuable sources of patient-specific geometries of the left atrium (LA) and left atrial appendage (LAA). For example, Alinezhad et al. (2022) [87] reconstructed LA and LAA geometries from cardiac CT scans of two patients with different anatomical morphologies to study intra-atrial flow fields using computational fluid dynamics (CFD) simulations. Similarly, Otani et al. (2016) [86] used cardiac CT and nonrigid image registration to estimate the endocardial wall

motion of the LA, therefore allowing for patient-specific flow simulation studies under sinus rhythm conditions. However, despite recent advancements in spatiotemporal resolution, both MRI and CT imaging still have some limitation to capture flow structures at small scales, and especially velocity fields of flow, in the LAA [92]. Limitations in imaging methods are especially meaningful in estimating hemodynamic quantities in the LAA, such as vortex formation, wall sheer stress, and areas of blood stagnation in lower flow regions, like distal LAA. For these reasons, numerical modeling techniques, particularly for solving governed equations by CFD, have become crucial tools for assessing LA function and predicting thrombus prone areas for clinical and research needs, especially with the include patient-specific spatial and computational data.

Atrial fibrillation (AF) initiates a drastic alteration in the flow dynamics of the LA by removing the atrial kick and superimposing high frequency fibrillatory wall motion. Computational studies have shown that combining the loss of atrial kick with high-frequency wall motion during AF leads to a marked increase in relative residence time (RRT) in the superior regions of the LAA, which is strongly correlated with clinically observed thrombus-prone areas [93]. Consequently, clarifying these complex phenomena using validated numerical models is very important for practical applications such as improving risk stratification, optimizing LAA occlusion therapies, and enhancing patient-specific diagnosis and treatment planning [91].

The numerical modeling of blood flow in the left atrium (LA) is based on the same foundational equations of fluid dynamics as ventricular modeling, which are the incompressible Navier-Stokes equations for the conservation of momentum and the continuity equation for the conservation of mass. Generally, the equations are established using the finite volume method (FVM), which will guarantee local conservation of mass and momentum over discretized control volumes [91]. In most cardiac studies, these models will rely on patient-specific geometries as cited previously, and will apply temporally-resolved boundary conditions based on anatomical data to reproduce physiologic flow conditions [92]. Image-based modeling approaches referencing a patient's own anatomy will be particularly applicable to simulating LA flow due to the chambers complex geometry and the importance of left atrial appendage (LAA) in stroke pathophysiology [87]. In this framework, the detail with which flow behavior can be characterized (e.g., vortex activity, wall shear stress (WSS), and relative residence time (RRT) will lend numeric simulations and supporting role as a mechanism for functional assessment of the LA [93].

Koizumi et al. (2015) [93] developed numerical models of a healthy LA and conditions reflecting two forms of AF (loss of atrial kick, fibrillatory wall motion) from MRI imaging and their results indicated that high frequency motion of the atrial wall dramatically enhanced blood stasis in the LAA measured by relative residence time (RRT) which is related to thrombus risk.

Additionally, Otani et al. (2016) [86] developed a clinically practical workflow for patient-specific LA blood flow analysis with 4D CT imaging and nonrigid image registration. They treated the motion of the endocardial wall as a prescriptive boundary condition and therefore did not need to include complex FSI coupling.

An alternative methodology is through geometric multiscale models. Zingaro et al. (2022) [91] combined a 3D Navier-Stokes solver with a lumped parameter model (0D) for circulation and electromechanical modeling of the left ventricle to propagate wall motion into the LA--enabling physiologically plausible boundary motion while retaining computational efficiency.

Dahl (2012) [92] also studied LA modeling through coupling image-based FSI simulations with physiologically realistic mitral valve motion, showing that the boundary conditions imposed by pulmonary vein inflow and mitral valve opening have a strong impact on the vortex structures and velocity fields inside the LA cavity.

Modeling of the LAA in particular has attracted a great deal of attention because of its important clinical relevance in AF (Atrial Fibrillation). Alinezhad et al. (2022) investigated the impact of morphological variations of the LAA on local flow and the risk of thrombus formation, showing using CFD simulations (on geometries reconstructed from CT data) that both the LAA shape and volume have strong influences on vorticity and velocity distributions, especially at the distal locations [87].

With regards to boundary conditions, the literature presents a range of approaches, some utilizing a time-varying mitral valve velocity profile, some with inflow profiles from the pulmonary veins derived from MRI, and others that adopt a pressure-based lumped outlet condition. Some studies even include dynamic mitral valve leaflets, and even chordae tendineae, in order to increase physiological fidelity [90].

2.5 Lumped Parameter Model

Lumped parameter models are effective approaches to modeling cardiovascular hemodynamics in a range of hemodynamic situations, specifically complex congenital heart diseases. These models abstract blood flow and cardiac function into electrical components that symbolize numerous physiologic elements [94]. Also, they have the capability to introduce time-varying elastance of the myocardium and valve dynamics to model normal and pathological states [95]. Dispositions of lumped parameter models have been utilized to investigate left ventricular remodeling through adjustment of elastance parameters [94] and to study hybrid palliation for hypoplastic left heart syndrome by examining the effect induced from typical variations in several surgical variables [96]. Specifically, lumped parameter models are beneficial for real-time bedside simulation of congenital heart diseases, possessing an advantage in computation time when compared to more complex multi-scale models [97]. Due to cardiovascular system's intricacy and the prohibitively high computing cost of modeling hemodynamics across the circulatory system, only models that can currently quantify both local and global hemodynamics are lumped parameter models [1].

2.5.1 Lumped Parameter Modeling of the Circulation

The following is a simplified method, based on a lumped parameter model, where desired blood parameters, such as flow rate, pressure, and volume, vary over time. By using a hydraulic-electric analogy, blood flow is modeled as an electrical circuit, where the fluid dynamics are analogous to the behavior of electrons in an electrical circuit. By using the governing equations of the electrical systems, researchers can derived mathematical models that can analyze and predict blood behaviors in the cardiovascular system [98].

The quantitative modeling of the arterial system began with the work of Otto Frank in 1899, who introduced the original two-element Windkessel model. This basic framework used a parallel arrangement of a resistor and a capacitor to mimic the arterial load on the heart and describe aortic hemodynamics [99]. As researchers became aware of the limitations of the original Windkessel model, particularly its inability to simulate high-frequency dynamics, more complex versions were proposed [100]. Adding a characteristic impedance to the aortic system led to the development of the three-element Windkessel model, which could better reproduce the oscillatory behavior of aortic input impedance at high frequencies [101]. To increase accuracy in the Windkessel model's performance at low frequency, a fourth inductive element was added to the model [102]. This

inductive component permitted the incorporation of the inertial effects of blood flow in the arterial system and reduced errors in input impedance over a full frequency range. However, the addition of the inertive element complicated the estimation of the parameters in the Windkessel model, as the model had more components than before [101]. Over the years, many adaptations of the Windkessel models have been proposed [103, 104], to more accurately replicate other physiological processes including microcirculation [105].

These modeling approaches have recently been used to assess artificial heart devices [106, 107], analyze hemodynamic responses to surgical interventions [108], and help greatly in developing personalized diagnostic methods [109]. In general, a lumped parameter model includes heart chambers that serve as pumping elements or prescribed pressure and flow waveforms, with paired vascular segments that mimic the transport of fluids throughout the circulatory system [98]. Within the electrical analogy framework, the typical configuration is illustrated as a composite of resistive, capacitive, and inductive components that embody different physical aspects of cardiovascular dynamics. Resistors, in particular, represent resistive opposition due to blood viscosity while flowing through vessels, capacitors represent elastic storage capacity of compliant vessels, and inductors serve to model inertial effects resulting from blood mass movement [110]. By manipulating the number of components utilized and varying the types, models can be built to vary complexities and resolution. Additionally, this modeling approach can be modulated to characterize a myriad of cardiovascular states, including peripheral and vascular disease [111], coronary artery disease [112], valvular disorders [113], and many more.

Essential physical laws are applied in order to accurately model physiologically correct system behavior. In the realm of hemodynamics, the laws of mass and momentum conservation are represented by the continuity equation, Poiseuille’s Law, and the Navier-Stokes equations, which describe how pressure and flow are distributed throughout the cardiovascular system [114]. By drawing parallels between electrical circuits and fluid dynamics, where fluid flow is akin to electric current and pressure is akin to voltage, the principles of fluid mechanics can be transitioned to the electrical domain. With this definition, Ohm’s and Kirchhoff's laws can be used to describe voltage and current behavior in the circuit representation of the previously mentioned principles of fluid mechanics [114].

By integrating these governing principles, each compartment in the model is described using a set of ordinary differential equations, along with an algebraic equation that defines the pressure–volume relationship through vessel compliance [115]. Whether the form of these equations will be linear or nonlinear is dependent on the complexity of the model, as well as the physiological factors included in the model. The same modeling approaches have been used to represent the dynamics of cardiac chambers and valves (e.g., computational hemodynamics). The computer must use numerical solvers to solve the system of equations, which then allow you to examine key hemodynamic variables (e.g., pressure, flow) at multiple locations in the vascular network. One of the foremost advantages of lumped parameter modeling is that it is computationally efficient, as these types of mathematical models usually only require solving ordinary differential equations and algebraic equations. Moreover, the model structure is likely simple enough to automate patient-specific versions of the simulations because of that efficiency. These advantages make lumped parameter modeling a reasonable approach to be used in high-throughput clinical workflows [116]. Lumped parameter modeling also provides a unique advantage for circulatory mechanics specifically, because it allows for simultaneous assessment of cardiac performance as well as systemic hemodynamics, supporting performance of the entire system in a single framework. Since cardiovascular components, such as the heart and vascular tissues are interactive components of which transfer functionality to entire circulatory system, capturing both the local and global dynamics will lead to a better capacity to afford for proper prediction and diagnosis of disorders of the cardiovascular vestibular system. While the method performed well alone, when combined with higher-fidelity models, it can provide a better representation of localized flow behavior [117]. Despite these strengths, challenges still remain, especially when it comes to aligning each of the model components to physiologically relevant values. Many parameters that exist in lumped parameter models cannot be directly tied to observed physiological parameters, and, as a result, estimates or inferences are used. Furthermore, even for parameters that it is mathematically possible to obtain values for, obtaining the values typically requires somewhat invasive or relatively cumbersome processes [114]. To circumvent this issue, it is common practice for investigators to summarize the existing literature, previous studies, population average values, or use information from involved animal studies [115]. Another way of getting around this issue is to combine parameters for the individual subject, through manipulation through a non-invasive process, to verify the model simulations [117]. adjusting the model parameters to present data

obtained from a specific patient enhances the personalization of the simulation. This patient-specific modeling approach is very important for creating accurate diagnostic and predictive tools that closely match to individual clinical needs.

2.5.2 Time-Varying Elastance Modeling

A commonly utilized method for simulating the contraction of heart chambers, is based on a concept referred to as time-varying elastance [118]. The initial description of the time-varying elastance concept was provided by Suga et al. (1973) [119], who analyzed the mechanical properties of the myocardium with a time-varying pressure-volume relationship which captures variations of myocardial stiffness during the cardiac cycle. Their studies were based on analysis of pressure-volume (PV) loops, representing heart function at some of phases of ejecting and isovolumetric (non-ejecting) contractions [120]. These studies demonstrated that pressure-volume obtained during any of a series of events in the cardiac cycle stacked along straight lines [119, 120].

While lumped parameter models provide substantial advantages to assess global hemodynamics and cardiac performance, there are also higher order modeling approaches that can enable more detailed modeling as one-dimensional wave propagation models, as well as three-dimensional CFD approaches. CFD modeling relies on the numerical discretization of the Navier–Stokes equations, including the with finite difference, finite volume and finite element techniques [121]. The main difference between lumped and higher order models is the spatial resolution. Whereas lumped (0D) models treat variables like pressure and flow as functions of time only, in 3D models the same variables are functions of spatial position. The consequence is a much greater level of detail and analysis of the local behavior of flow in the cardiovascular system. Mathematically, this means that higher order models are ultimately derived using systems of nonlinear partial differential equations (PDEs), while lumped parameter models are derived using ordinary differential equations (ODEs). Due to its structure, lumped parameter modeling serves as an effective method for simulating both the heart and the broader circulatory system, along with their related pathologies. Continued refinement and individualization of these models may contribute to advancing cardiovascular simulations as a valuable tool in addressing the worldwide burden of cardiovascular diseases. Table 2.4 illustrates the application of Lumped parameter modeling in some of the scientific literature.

Table 2.4 Lumped parameter literature review

Reference	Heart Region Modeled	Application Focus	Model Type	Personalization Method	Validation Approach
Shimizu et al. [97]	Whole circulation (all 4 chambers + systemic/pulmonary)	Simulation of congenital heart diseases (e.g. Hypoplastic LH Syndrome, Fontan circulation), perioperative hemodynamic management	Lumped Parameter Model (Time-varying elastance model + modified Windkessel vascular model)	Uses patient-specific anatomical and physiological inputs (MRI, CT when available)	Comparison with known physiological expectations and prior clinical knowledge
Garber et al. [1]	Systemic circulation (review paper, broad coverage)	Review of LPM in digital twins & clinical translation	Lumped Parameter Model +	Clinical inputs, patient-specific data, and optimization algorithms	Comparison to clinical data (MRI, DE, catheterization)
Ali et al. [94]	Left Ventricle	Remodeling assessment under pathological states	Lumped Parameter (time-varying elastance + Windkessel)	Clinical measurements integrated into parameter tuning	Comparison with published hemodynamic data and trends from literature
Zhou et al. [122]	Systemic arteries (not chambers)	Central aortic pressure estimation	Lumped (0D), 1D, Tube-load models	Uses arterial compliance/resistance from clinical data	Comparison with catheter data and echocardiography
Di Molfetta et al. [96]	Systemic & pulmonary circulation in HLHS	Surgical planning for hybrid palliation (ASD, PAB,	Lumped Parameter Model	Patient-specific newborn HLHS measurements used to initialize	Comparison of simulated outputs (Qp/Qs, CO, stroke work) with measured

		PDA stent, RevBT)			baseline in a patient
Segers et al. [120]	LV + systemic and pulmonary arteries	Heart-arterial interaction (ventricular-arterial coupling)	Lumped Parameter (LV elastance + 4-element Windkessel)	Derived from experimental pig (systemic) and dog (pulmonary) data	Direct comparison with measured animal data (pressure, flow)
Korakianitis et al. [123]	All four chambers + systemic & pulmonary circulation	Heart valve dynamics (mitral stenosis, aortic regurgitation)	Lumped/Concentrated Parameter with detailed valve sub-model	Literature-based parameters and valve motion equations	Reproducing textbook PV loops and valve pathologies
Zingaro et al. [68]	Large systemic arteries + coupling to heart/arterial junctions	Developmentof multiscale framework linking 3D CFD with 1D/0D LPM models	Hybrid Multiscale (3D CFD + 1D models + 0D Windkessel)	Geometric models derived from MRI/angiography, physiological parameters from literature and clinical data	comparison with clinical pressure/flow waveforms in systemic arteries

CHAPTER 3 OBJECTIVES

As discussed in chapter two, the current method to collect hemodynamic parameters could be, intensive, expensive and time-consuming. Thus, performing regular clinical methods such as catheterizations for therapeutic monitoring becomes unfeasible [124] and imaging techniques have certain limitations that prevent precise analysis of cardiac flow such as temporal resolution and spatial resolution. Therefore, this thesis focuses on developing a patient-specific CFD framework coupled with an elastance model, validated against MRI data, to characterize LV and LA hemodynamics at rest. The approach is designed to balance physiological accuracy with computational feasibility. Previous computational studies of cardiac hemodynamics have provided valuable insights into ventricular and atrial flow patterns, yet they also reveal several limitations. Fully coupled fluid–structure interaction (FSI) models can reproduce realistic wall motion but are extremely computationally expensive and impractical for patient-specific or clinical applications. On the other hand, while simplified CFD simulations with rigid or quasi-rigid walls reduces simulation time but overlook certain aspects of wall–flow interaction and dynamic ventricular deformation.

In this thesis, a patient-specific program was developed in MATLAB to simulate blood flow within the left heart across 25 cardiac phases extracted from MRI image of patients. A lumped parameter elastance model was used to generate realistic time-varying pressure and boundary conditions. Then, the solver couples LPM with CFD module, and each chamber was discretized using an unstructured triangular mesh, which made computation of spatial flow features such as velocity, wall shear stress, and vorticity possible using a 2D CFD simulation. This hybrid modeling approach bridges the gap between simplified rigid-wall CFD models and computationally intensive FSI simulations by incorporating realistic wall motion extracted from MRI while maintaining numerical efficiency suitable for clinical research.

The objective of this thesis is to propose a method for analyzing blood flow in the left heart at rest and the following are the sub objectives of this study:

1. Develop an elastance model to simulate the blood flow in the left heart
2. Couple the elastance model with CFD model to calculate WSS and vortex intensity
3. Verify and validate the model

To achieve the first sub objective, it's possible to use cardiac MRI to extract the geometry of the left heart over time in order to conduct an in-silico study of blood flow. Since the imaging provides sufficiently precise information on the left heart's geometry in a patient-specific manner, the prescribed-geometry numerical model described in the previous chapter is particularly well-suited for studying blood flow. Building upon this, a lumped parameter model can be developed to provide essential hemodynamic quantities such as velocity throughout the cardiac cycle. The second sub objective requires coupling the elastance-based model with CFD to determine wall shear stress and vortex intensity measurements. In most studies that only used CFD simulation, fixed or idealized inlet and outlet were often imposed as boundary conditions. However, in this study LPM was integrated into the CFD framework to provide physiologically consistent boundary conditions that cannot be obtained from imaging alone. The LPM generates time-varying pressure and flow profiles derived from the global elastance behavior of the cardiac chambers. This allows the CFD solver to capture the interaction between global cardiac function (modeled through the LPM) and local hemodynamics within the left heart. As a result, the coupled LPM–CFD approach produces more realistic pressure gradients, velocity fields, and wall shear stress distributions than CFD simulations driven solely by prescribed boundary conditions.

The explanation of the complete method for coupling these models can be found in Chapter 4. The simulation results undergo validation against 4D MRI data and existing literature to fulfill the third sub-objective. The validation process described in Chapter 5 verifies that the proposed framework maintains both physiological accuracy and consistency with experimental and numerical research findings.

CHAPTER 4 METHODOLOGY

In this chapter, the scientific methodology adopted in this thesis is presented. The chapter begins with a description of patient-specific geometry extraction from MRI, followed by the development of the lumped model and CFD framework. The coupling strategy between the two domains is then explained in detail.

4.1 Geometry Acquisition

A cardiac MRI analysis was performed on a healthy 34-year-old woman (height: 1.60 meters and weight: 71 kg) with no underlying cardiovascular pathology. The acquisitions included an ECG-gated cine TruFISP sequence at 3T (Siemens Skyra™) using an 18-channel RF coil, allowing the capture of 25 phases of the cardiac cycle. The acquisition was performed at rest, with the subject lying down and remaining still before and during the scan. The three-chamber view was used to extract the 2D geometry.

By using MRI images, it is possible to extract the geometry of the left heart over a full cardiac cycle (25 Phases). Since the image gives us sufficiently precise information on the geometry of the left heart in a patient-specific manner, the prescribed geometry CFD method, described in the previous sections, is particularly suitable for studying blood flow. The model's contour was developed by using Segment (Medviso) software [125]. Then after extracting the coordinates (x,y) of the obtained contour into an excel file, the geometry was reconstructed by ®MATLAB R2021b (©The MathWorks, Inc.). The following procedure is illustrated in Figure 4.1.

To ensure reliability and repeatability of the segmentation process, each geometry reconstruction was performed three times using identical procedures. The repeated geometries showed negligible variation in spatial dimensions and derived flow fields, confirming the robustness of the manual segmentation protocol. This analysis also served as a part of the model sensitivity study (detailed in Chapter 5).

For more realistic shape of left heart chambers especially around the valves, parametric equations were used. These equations are sine and cosine functions which were used to generate a shape resembling the natural curvature of the left heart. For example, to better shape LV cross-section, trigonometric functions 4.1 were used.

$$x\,(\theta) = a.\cos(\theta) + b.\cos(2\theta) y(\theta) = c.sin(\theta) \qquad 4.1$$

Where θ ranges from 0 to 2π, and a, b and c are constants controlling the LV's width, curvature, and height.

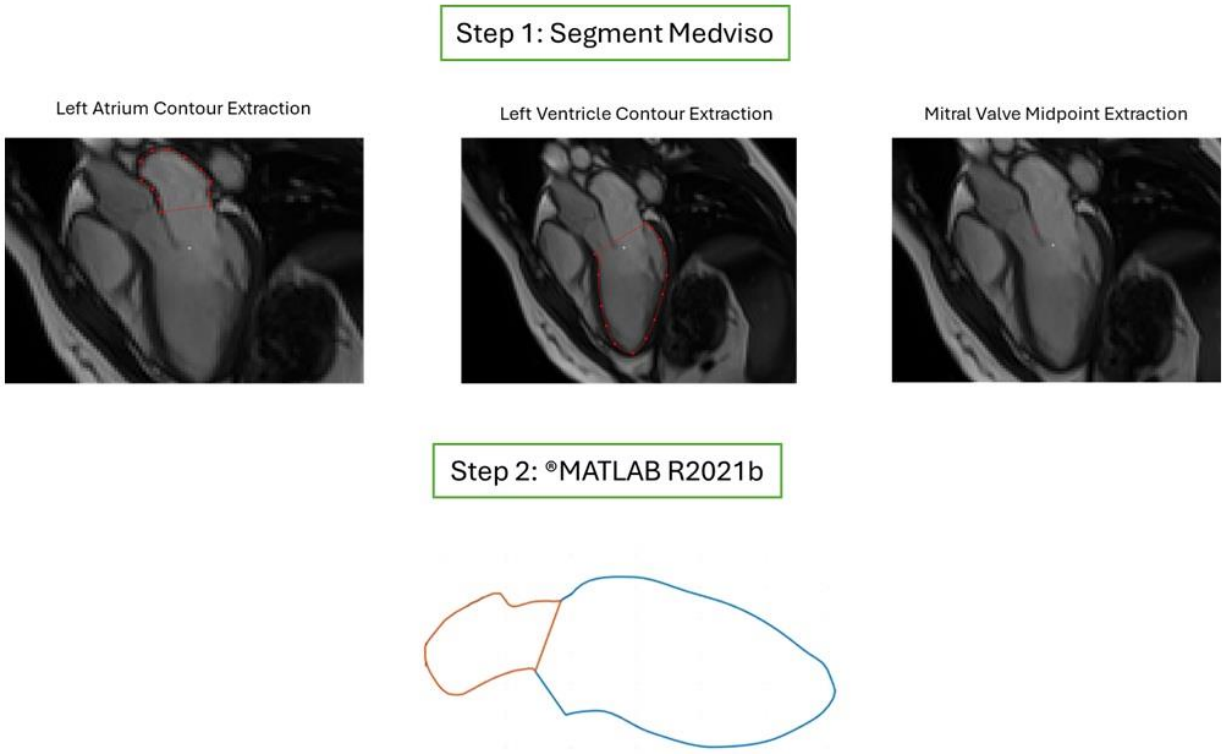

Figure 4.1 Workflow of patient-specific geometry extraction and MATLAB-based reconstruction

Using MATLAB, for each of 25 cardiac phase the following parameters were calculated to provide mathematical definition used to compute geometric metrics [126].

Area was calculated using Shoelace formula (equation 4.2) with n being the number of boundary points, i the index current vertex, x_i, y_i are cartesian coordinates of vertex i.

$$A = \frac{1}{2}\left|\sum_{i=1}^{n}(x_i y_{i+1} - x_{i+1} y_i)\right| \quad 4.2$$

The perimeter was obtained by summing the Euclidean distance between consecutive contour points (Eq 4.3) in which once again n is the number of boundary points, i, the index current vertex, x_i, y_i are cartesian coordinates of vertex i.

$$P = \sum_{i=1}^{n}\sqrt{(x_{i+1} - x_i)^2 + (y_{i+1} - y_i)^2} \quad 4.3$$

Hydraulic radius was calculated using equation 4.4

$$R_h = \sqrt{\frac{A}{\pi}} \tag{4.4}$$

And finally, centroid was obtained by the following equations (eq 4.5 and 4.6)

$$\bar{x} = \frac{1}{6A}\sum_{i=1}^{n}(x_i + x_{i+1})(x_i y_{i+1} - x_{i+1} y_i) \tag{4.5}$$

$$\bar{y} = \frac{1}{6A}\sum_{i=1}^{n}(y_i + y_{i+1})(x_i y_{i+1} - x_{i+1} y_i) \tag{4.6}$$

With A in equation 4.4-4.6 being the area which was calculated using equation 4.2.

4.2 Lumped Parameter Modeling

In this part of the simulation, a time-varying elastance model is used to describe the mechanical behavior of heart chambers. Elastance is defined as the ratio of pressure to volume and models the contractile behavior of the myocardium throughout the cardiac cycle.

Elastance (E) is a concept from cardiovascular physiology used to model how "stiff" or "contractile" a heart chamber is at any moment in the cardiac cycle. This concept was developed by Sagawa et al. (1973) [119]

$$E(t) = \frac{P(t)}{V(t) - V_0} \tag{4.7}$$

In the equation above E(t) is the time dependent elastance, P(t) is the pressure in the heart chamber at time t, V(t) is the volume of the chamber at time t, and V_0 is volume at zero pressure.

As explained by Sagawa et al. [119] a time varying elastance model which can be describe as how the stiffness of the ventricle or atrium changes over one heartbeat. The elastance curve rises during contraction and falls during relaxation. Equation 4.8 was used to model the dynamic change in stiffness over the cardiac cycle.

$$E(t) = E_{min} + (E_{max} - E_{min}).\, e(t) \tag{4.8}$$

Where, E_{min} is diastolic elastance, E_{max} systolic elastance, and e(t) is normalized activation function, often defined using sine or exponential functions, ranging from 0 to 1 over the cardiac cycle.

To implant this model to the study presented here, for each time step t, first the phase of the cardiac cycle (e.g. systole or diastole) needs to be determined then the time varying elastance was calculated with key factors of:

E_la_min and E_la_max: Minimum and maximum elastance of the left atrium. E_lv_min and E_lv_max: Minimum and maximum elastance of the left ventricle.

After implementing of this into the model, we can understand whether the mitral valve is open or closed. For example, when P_{atrium}>$P_{\text{ventricle}}$, the mitral valve opens. Finally, the blood flow can be calculated at each time step of t. These time-varying pressure and flow values are then transferred as boundary conditions to the CFD solver, which computes the detailed velocity and pressure distributions inside the chambers. In other words, the LPM acts as a hemodynamic driver for the CFD model that provides consistent inlet and outlet conditions.

As Owashi et al. (2020) [127] explained in their research, another parameter must be defined in the model named P_systemic. P_{Systemic} refers to the mean systemic arterial pressure, which is the average blood pressure in the systemic circulation this is a constant between 90-100 mmHg. In the left heart, blood is ejected from the LV into the aorta, which is the start of systemic circulation. The importance of this parameter is to understand when the blood flows out through the aortic valve into the body. For example, when P_{LV}>P_{Systemic}, the aortic valve opens.

As described by Westerhof et al. (2009) [128] in the simplified Windkessel model, mean systemic pressure serves as a downstream boundary condition. It's used to compute the outflow from the left ventricle through the aortic valve like eq. 4.4.

$$Q_{ao} = \frac{P_{LV} - P_{\text{Systemic}}}{R_{ao}} \tag{4.9}$$

Where, Q_{ao} is the blood flow through the aortic valve, and R_{ao} is the resistance of the aortic valve.

For more accurate calculation of P_{Systemic} eq. 4.10 can be used.

$$P_{\text{Systemic}} = \frac{1}{3}\, Systolic + \frac{2}{3}\, Diastolic \tag{4.10}$$

The same logic was used for the blood flow through the mitral valve (eq. 4.11) so two new parameters are needed as R_mv: Resistance of the mitral valve and R_ao: Resistance of the aortic valve.

$$Q_{mv} = \frac{P_{LA} - P_{LV}}{R_{mv}} \tag{4.11}$$

The cardiac cycle was divided into 25 temporal phases, consistent with the temporal resolution of the MRI acquisition (approximately 40 ms between frames). Each phase was treated as a quasi-steady state, meaning that the flow field was solved independently for that geometry. For each phase:

- The time-varying elastance was computed based on the current cardiac phase.
- Pressures in the left atrium and ventricle were determined from the elastance–volume relations.
- Valve states (open or closed) and the corresponding flow rates were calculated using Equations (4.4) and (4.5).
- These pressures and flow rates served as boundary conditions for the CFD solver, which computed the spatial distribution of velocity, pressure, and wall shear stress within the chamber.

Figure 4.2 illustrates this workflow.

4.2.1 Assumptions

Multiple physiological and mechanical variables must be provided as inputs to the simulation. Since the exact patient specific values are not available, they were selected based on commonly reported ranges in the literature for healthy adults at rest or based on assumptions made to ensure numerical stability and physiological realism. The assumptions made are summarized below:

- The simulation showcases a single cardiac cycle segment split into 25 phases, each with a Δt of 10 ms which reflects a heart rate of $\approx$ 75 BPM. This time resolution aligns the LPM and CFD solvers and preserves the temporal synchrony of pressure, flow, and geometry updates.

- the mitral valve resistance was set to 0.5 mmHg·s/mL, which is a commonly used value in lumped cardiovascular models [123] and provides physiologically plausible flow during the filling phase.
- The blood was assumed as a Newtonian fluid with viscosity of 0.0035 Pa.s which is approximation used in cardiac models for large vessels and chambers [49]. This value corresponds to standard physiological conditions at 37°C and normal hematocrit.
- The chamber walls were treated as quasi-rigid (no FSI), with motion prescribed directly from MRI-derived contours over 25 phases. This kinematic approach reproduces measured shape changes of the left atrium and ventricle while neglecting dynamic myocardial elasticity.
- Based on normal ranges documented in the literature [123], elastance values for the left ventricle and atrium were assumed in this simulation. Normal systolic function is reflected in the LV elastance, which ranges from 0.5 mmHg/mL during diastole to 2.0 mmHg/mL during systole. In accordance with simplified lumped-parameter models [123], which do not explicitly include atrial contraction, the LA elastance was maintained at 0.5 mmHg/mL.
- The simulation was conducted in 2 dimensions.
- The time-varying elastance function was defined using a normalized activation profile consistent with the Suga–Sagawa [129] formulation, ensuring physiologically accurate timing of contraction and relaxation.
- Valve flow is calculated by pressure difference divided by resistance; inertial and capacitance effects are ignored.

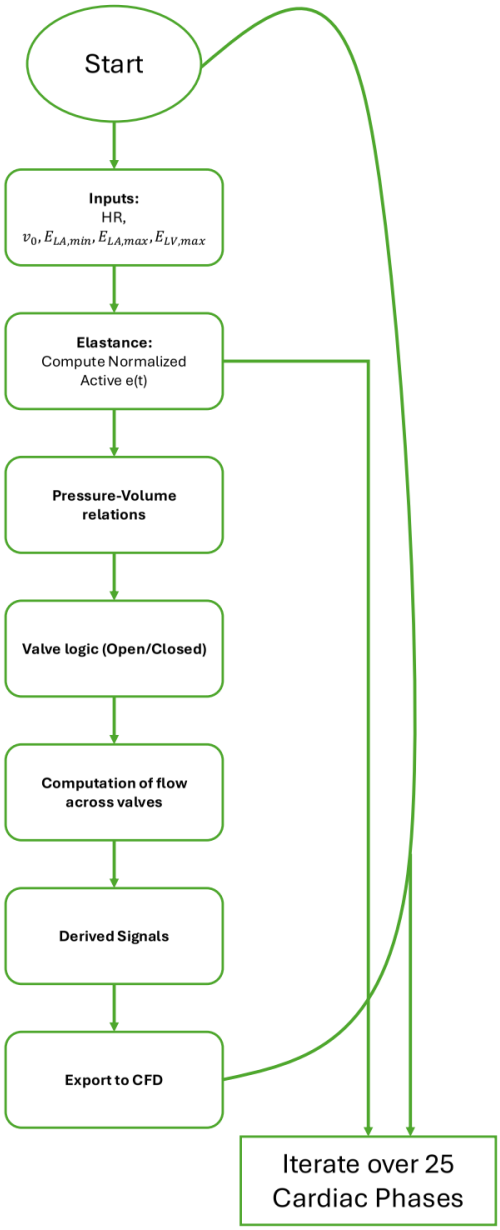

Figure 4.2 Flowchart of Lumped parameter modeling

4.3 CFD Simulation

As explained in previous sections, the CFD module was used to simulate blood flow within the 2D patient-specific geometry of the left heart over 25 cardiac phases which were extracted from MRI. All CFD simulations in this thesis were carried out with an in-house finite-volume solver implemented in MATLAB; no commercial CFD software (such as Ansys Fluent) was used. The

simulation tries to capture key hemodynamic parameters such as velocity fields, WSS and vorticity patterns, using physiological boundary conditions imported from the LPM model.

To address the difference between the fast fluid response timescale and the slow wall motion timescale in cardiac hemodynamics and allowing the flow field to reach local equilibrium at each geometry configuration before advancing the next phase, a multi phase quasi steady method was used to balance computational efficiency and physiological realism. At a given time step, the wall boundary is assumed rigid and fixed during the CFD inner iterations (predictor–Poisson–corrector loop), and a no-slip condition is imposed on that boundary. The wall position is then updated at the next time step by mapping the simulation time to the corresponding MRI contour frame; therefore, the computational domain evolves over time while remaining rigid within each time step (quasi-static moving boundary).

For every phase, the chamber geometry was updated according to the volumes computed by the elastance model, and inlet velocity or pressure at the pulmonary veins and outlet pressure at the aortic valve were imported from time-varying values derived from the LPM. This method guarantees consistency between large-scale cardiac dynamics and local flow simulation. Importantly, the no-slip condition was also imposed at all wall boundaries. This treatment is consistent with common computational fluid dynamics (CFD) practices in cardiac mechanics and makes an insignificant contribution to overall computation cost while providing physical realism [130].

In this thesis, pressure recovery was done through the local treatment of continuity and momentum balance, where pressure at every node is updated one at the time to ensure a divergence-free velocity field. This numerical process is the same from a mathematical perspective as solving the Poisson equation iteratively with Jacobi or Gauss–Seidel updates in physical space [131]. The key difference of this approach with other studies that used projection or pressure-correction methods, where the Poisson equation for pressure is solved globally across the entire computational domain at each iteration, is that the method implemented in this study enables local corrections to be applied in succession based on the mass conservation constraint, instead of solving and inverting a large matrix for the entire domain, as in traditional implementations. This local correction approach comes with better numerical stability when working with complex curved boundaries at much lower computational costs than solving Poisson equations globally.

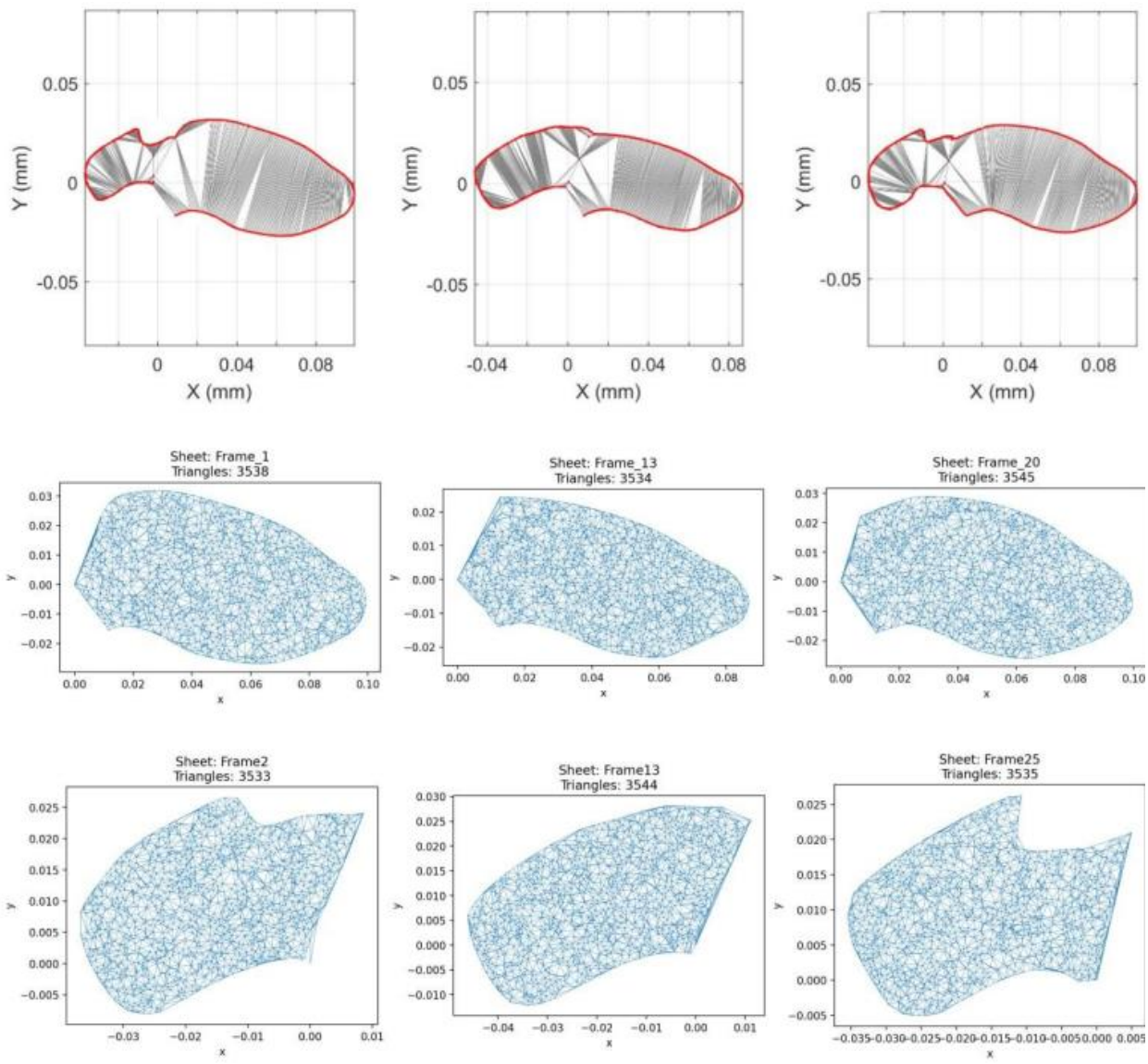

Figure 4.3 Examples of applied mesh

Spatial discretization applied using an unstructured triangular mesh that was generated for each cardiac phase using Delaunay triangulation algorithm [132]. Average element number was 1850 ± 230 and minimum metric quality was 0.65. Top row of figure 4.3 shows four contours of LV that extracted from MRI, while the bottom row presents the applied mesh for the same cardiac phase. and its corresponding mesh. The element quality criteria were defined using the following equation.

$$q = \frac{4\sqrt{3}.A}{h_1^2 + h_2^2 + h_3^2} \qquad 4.12$$

Where A is element area and h_i is the length of each side of triangle (q=1 shows an equilateral triangle). To apply boundary layer refinement in sections with high curve such as those near mitral valve, nodes density was multiplied by 2.5 to ensure more accurate resolution of flow gradient.

Figure 4.4 provides detailed information about the workflow that was implemented in the CFD simulation.

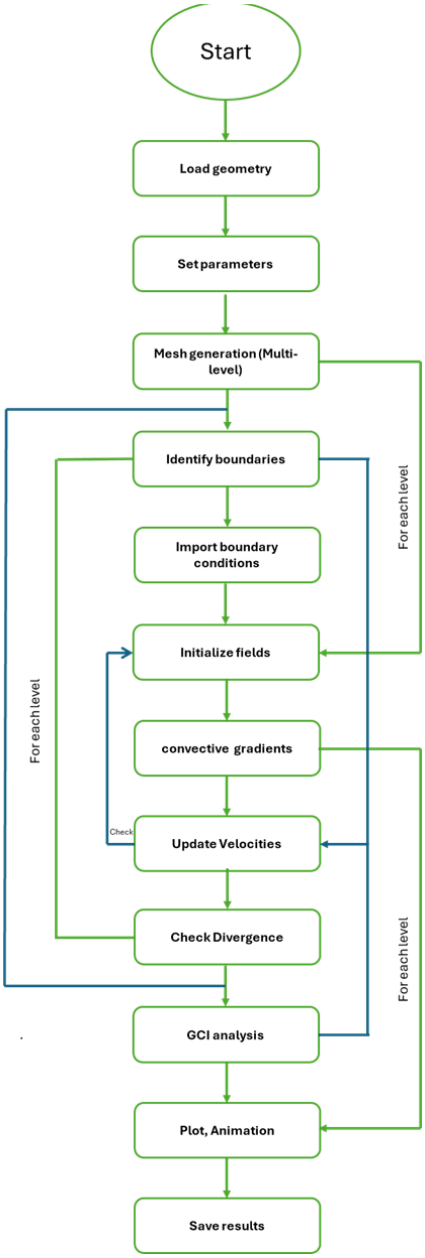

Figure 4.4 Flowchart of CFD simulation

4.3.1 Governing Equations

The continuity equation and the Navier-Stokes Equations (momentum and energy) govern numerical models used to simulate heart flow; however, these equations take on unique forms in the context of heart flow. Many numerical studies and tools for modeling the fluid flow in the LV use the Arbitrary Lagrangian–Eulerian (ALE) formulation of Navier–Stokes for solving the fluid flow domain by finite volume method (FVM). The integral form of the continuity equation for an arbitrary volume V and surface S moving at a local surface velocity v_b is:

$$\frac{\partial}{\partial t}\int_V \rho dV + \int_S \rho(\vec{v} - \vec{v}_b).\vec{n}dS = 0 \tag{4.13}$$

Where, $\vec{n}$ is the vector normal to dS that is directed outward, ρ is the fluid's density, $\vec{v} = (u, v)$ is the fluid's velocity vector in the fixed coordinate system, and $\vec{v}_b = (u_b, v_b)$ is the moving boundary's velocity (the velocity of boundary S of control volume V) velocity vector [44]. Given in integral form, the momentum equation is:

$$\frac{\partial}{\partial t}\int_V \rho\vec{v}dV + \int_S \rho\vec{v}(\vec{v} - \vec{v}_b).\vec{n}dS = -\int_S P\vec{n}dS + \int_S \bar{\tau}.\vec{n}dS \tag{4.14}$$

where $\bar{\tau}$ is the viscous stress tensor and P is the pressure. The body forces are not considered in the calculation above.

The expression $\bar{\tau}$ for an incompressible Newtonian fluid is:

$$\bar{\tau} = 2\mu\bar{\Gamma} = \mu(\nabla\vec{v} + \nabla\vec{v}^t) \tag{4.15}$$

$$\tau_{ij} = \mu\left(\frac{\partial u_i}{\partial x_i} + \frac{\partial u_j}{\partial x_i}\right) \tag{4.16}$$

Since the blood is thought to be a Newtonian fluid in certain investigations, μ in Equations 4.15 and 4.16 is constant. However, in other studies, blood is modeled as a non-Newtonian fluid, in which case the viscosity μ varies with the local shear rate and is defined by specific constitutive models such as the Carreau–Yasuda or Casson formulations.

The velocity field in this study is imposed based on volume conservation assumptions and elastance-calculated flows. That is, for each time step: the instantaneous flow rate (e.g., from mitral or aortic valve) is converted to a velocity field distributed over the chamber walls. These velocities are used to calculate spatial gradients, particularly velocity derivatives near the wall, to calculate WSS:

$$\tau_{\omega} = \mu . \left.\frac{\partial u}{\partial n}\right|_{wall} \quad 4.17$$

Boundary conditions of this simulation are as follows:

At Pulmonary Vein Inlet a time-dependent parabolic velocity profile was prescribed to represent physiologically realistic inflow conditions. The velocity distribution was defined as

$$u(r,t) = u_{max}(t)\left[1 - \left(\frac{r}{R}\right)^2\right] \quad 4.18$$

Where r is the radial coordinate and R is the inlet radius. The maximum velocity $u_{max}(t)$ was obtained from the instantaneous volumetric flow rate Q(t) provided by the LPM according to

$$u_{max}(t) = \frac{2Q(t)}{\pi R^2} \quad 4.19$$

At the mitral valve outlet, a time-varying pressure boundary condition was applied, prescribed directly from the left atrial pressure obtained from LPM as

$$p = p_{LA}(t) \quad 4.20$$

This approach ensures that the outlet pressure dynamically follows the physiological atrial waveform and remains coupled to the LPM during each cardiac phase.

Along the atrial wall boundaries, a no-slip and no-penetration condition was enforced, defined by

$$u = 0 \quad 4.21$$

implying zero tangential velocity and zero normal flux at the wall surface. This ensures realistic interaction between the blood flow and the endocardial surface.

4.3.2 Numerical Implementation

The incompressible Navier–Stokes equations are solved on the unstructured triangular mesh (Fig. 4.3), generated by Delaunay triangulation for each cardiac phase. A projection (pressure-correction) scheme is used to enforce incompressibility, consistent with the pressure-recovery description given in the CFD section. For each time step (and for each inner coupling iteration), the algorithm proceeds as follows:

Step 1 — Momentum predictor

Given $\mathbf{u}^k$ and p^k, an intermediate velocity u* is obtained by advancing the momentum equation with convection, diffusion, and the pressure-gradient term treated explicitly:

$$u^* = u^k + \Delta t[-(u^k.\nabla)u^k + \nu\nabla^2 u^k - \frac{1}{\rho}\nabla p^k] \quad 4.22$$

On the unstructured mesh, spatial derivatives are evaluated using piecewise-linear (P1) triangular reconstruction: gradients are constant per triangle and then averaged to nodes using area-weighted accumulation. This same operator is used consistently for ∇p, $\nabla p'$, and $\nabla \mathbf{u}$

Step 2 — Pressure-correction Poisson equation.

To enforce $\nabla \cdot \mathbf{u}^{n+1} = 0$, a pressure correction $p'$is introduced such that:

$$\nabla^2 p' = \frac{\rho}{\Delta t}\nabla.u^* \quad 4.23$$

Discretization on the unstructured mesh yields a sparse linear system:

$$Kp' = b \quad 4.24$$

where K is the assembled Laplacian/stiffness matrix and $b \propto (\rho/\Delta t)\nabla \cdot u^*$. Rather than solving this system via direct inversion, it is solved iteratively using Jacobi or Gauss–Seidel relaxation, which is mathematically equivalent to the local pressure-recovery description already stated. he Jacobi update at node i is:

$$P'^{(k+1)}_I = \frac{1}{k_{ii}}\left(b_i - \sum_{j\neq i} K_{ij} p'^{(k)}_j\right) \quad 4.25$$

and Gauss–Seidel uses the same update sequentially while immediately incorporating newly updated neighbor values.

Step 3 – Velocity correction

After convergence of the Poisson iterations,

$$u^{n+1} = u^* - \frac{\Delta t}{\rho}\nabla p' \quad 4.26$$
$$p^{n+1} = p^k + \alpha_p p'$$

Boundary conditions (no-slip walls and valve-driven inflow/outflow) are re-applied after predictor and corrector updates.

The velocity gradients required for the viscous stress tensor (Eq. 4.16) are evaluated from the converged velocity field using the same unstructured gradient operator. These gradients are then used for computing shear-related quantities (e.g., WSS), consistent with Eq. (4.17). Importantly, these velocity gradients are not part of the Jacobi/GS pressure iterations themselves; the pressure iterations solve $\mathrm{K}p' = b$, after which $\nabla p'$is evaluated to project the velocity field.

4.4 Coupling Strategy

Within this thesis, a one-way phase synchronized coupling method was utilized to integrate LPM with the CFD simulation. Using this approach, LPM provides time-dependent pressures and flow rates for each cardiac phase while the chamber geometries for each of those phases are taken directly from MRI data. This is an essential coupling to ensure physiologically consistent global elastance-based ventricular dynamics with local intracardiac flow behavior. For each of the 25 cardiac phases and at each time step, the following procedure is performed:

1. Lumped Parameter Computation

   The LPM computes the instantaneous chamber pressures, and inflow/outflow rates based on elastance functions and valve flow resistance.

2. Geometry Selection for CFD

   The left heart geometry which was extracted from MRI is selected for this phase, consistent with the chamber volume obtained from LMP.

3. Boundary Condition Assignment

   Inlet velocity and outlet pressure are specified based upon the LPM results. A no-slip boundary condition is specified at the wall boundaries to allow the flow to develop in a realistic fashion.

4. CFD Simulation Step

   The CFD solver uses an iterative approach to calculate the velocity and pressure fields, until local mass and momentum conservation are achieved, which is generally interpreted as a quasi-steady state for that phase.

5. Repeat for all phases

   The process is repeated for each phase of the cardiac event to reconstruct the flow field over time across the cardiac cycle.

This strategy allows for representation of dynamic blood flow patterns and wall interaction while maintaining numerical stability of the model. Figure 4.5 Illustrates this workflow. In this study, a prescribed-geometry CFD approach was used. Chamber deformation was derived from elastance-driven radial contraction mechanics and applied as boundary motion. These boundary conditions were then used by the CFD solver to compute intraventricular velocity fields, wall shear stress, and vortex intensity. Thus, velocities were not imposed throughout the domain but calculated based on the prescribed boundary kinematics.

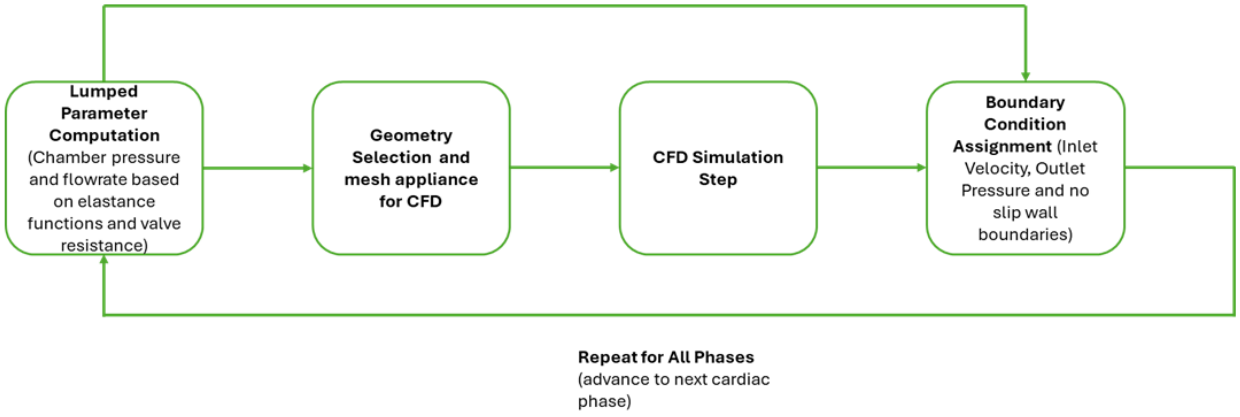

Figure 4.5 Flowchart of coupling strategy

CHAPTER 5 RESULTS

This chapter presents and analyzes the key findings obtained from the computational simulations of left heart hemodynamics. The results include spatial and temporal distributions of velocity fields, pressure, wall shear stress (WSS), and vortex structures over the cardiac cycle. These outcomes are derived from the coupled LPM–CFD model described in the previous chapter.

To assess the model's reliability, the simulated data are validated against published experimental and computational studies. Quantitative comparisons are performed where possible, particularly for WSS, to evaluate the agreement with literature-reported values. Additionally, a sensitivity study is conducted to explore the influence of key modeling parameters such as blood viscosity and temporal resolution on the simulation outputs.

The chapter concludes with a discussion of the physiological relevance of the results, the strengths and limitations of the modeling approach, and potential directions for future work.

5.1 Solver Validation

Before applying the CFD solver for the simulation of complex cardiac flows, the accuracy and numerical stability of the solver were first established by comparing the solver's results to the analytical solution of the classical Womersley oscillatory flow problem. The Womersley flow problem has an analytical solution and it is common to benchmark solvers against this flow problem in biomedical fluid mechanics [133] so using this test it's possible to declare that the solver used in this study is capable of accurately simulating oscillatory flow characteristics similar to those in the heart.

The Womersley flow describes pulsatile motion of an incompressible Newtonian fluid driven by a sinusoidal pressure gradient in a rigid channel. The parameters used in this validation are listed in table 5.1.

Table 5.1 Used parameters in Womersley problem

Channel height	h = 1cm
Blood density	$\rho = 1060\frac{kg}{m^3}$

Dynamic viscosity	μ = 0.0035 Pa.s
Heart rate	HR = 72 bpm
Pressure gradient amplitude	$\frac{dP}{dx}$ = $100^{Pa}/_{m}$

These values correspond to a Womersley number $\alpha = 7.56$, which lies within the physiological range for cardiac blood flow.

The simulation was conducted in a 2D channel with 200 grid points in the vertical direction and a conservative Courant number (CFL = 0.05) to ensure stability. The time step was $\Delta t = 3.8 \times 10^{-5}$s, and the simulation was run over three full cardiac cycles to reach a periodic steady state.

The results of simulation, which can be found in Figure 5.1, showed that the centerline velocity closely matched the analytical Womersley solution in both amplitude and phase. The relative error was 2.7%, which is well below the acceptable limit of 5%.

The computed WSS waveform exhibited excellent agreement with analytical profile, with a maximum deviation of 2.72% and a mean amplitude of approximately 0.06 Pa.

The velocity profile across the channel height showed the expected parabolic shape. The no-slip condition at the walls was fully satisfied, confirming correct boundary implementation.

Finally, both velocity and WSS errors decreased over successive cycles, indicating convergence toward a periodic steady-state solution.

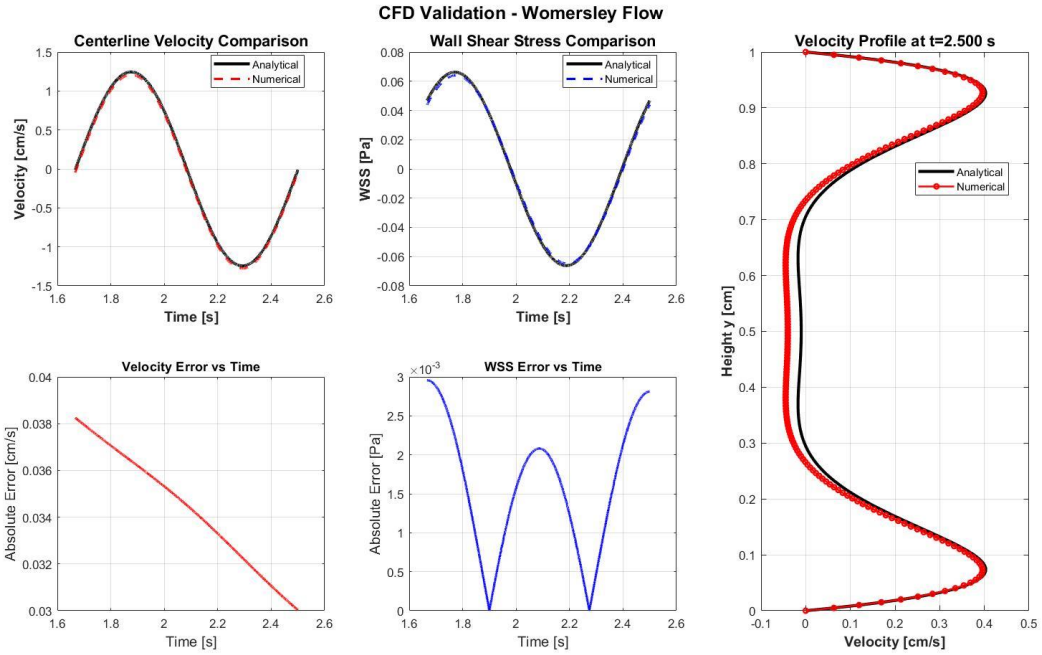

Figure 5.1 Results of CFD solver in Womersley problem

This validation confirms that the implemented CFD solver accurately reproduces oscillatory flow dynamics with high numerical stability and precision. Therefore, the solver used in this study is scientifically validated and suitable for simulating patient-specific hemodynamics in the left heart geometry.

5.2 Simulation Results

As described in Chapter 4, intracardiac flow patterns in the left atrium (LA) and left ventricle (LV) were simulated using LPM-CFD solver. This section presents the main numerical results obtained from the simulation. The results were categorized into three different parts. The first part would present the geometrical analysis, the second part provides an understanding of the global hemodynamic parameters calculated by LPM and the detailed flow field characteristics computed by CFD solver across cardiac phase is presented in third part.

5.2.1 Geometrical Analysis

As described in depth in chapter 4, parameters of R_h, perimeter and area were calculated using MATLAB. These parameters provide a valuable information that could be used to measure the physiological accuracy of the solver. Table 5.2 provides a summary of these parameters based on

the four critical cardiac cycles showed in figure 4.3. In this table t/T is non-dimensional time variable that represents the normalized cardiac phase, where T is the total duration of one cardiac cycle. Thus, $t/T = 0$ corresponds to end-diastole and $t/T = 1$ to the beginning of the next cycle."

Table 5.2 Geometrical Parameters

Physiological Interpretation	R_h (cm)	P (cm)	A (cm^2)	t/T	Time (ms)	Phase
End of atrial contraction – minimum volume	0.12	0.89	0.42	0.035	28	1
Mid-diastole – rapid filling phase	0.28	1.76	2.18	0.315	252	9
Ventricular diastasis – full relaxation	0.33	2.29	3.68	0.840	672	20
Late diastole – maximum atrial volume	0.36	2.29	3.68	0.840	672	24

One of key findings of table 5.2 is that left atrial cross-sectional area varied between 0.42 and 3.68 cm² throughout the cardiac cycle, corresponding to an approximately 8.7-fold change in projected area. Based on this information, Atrial Ejection Fraction (AEF) can be calculated using the following equation.

$$AEF = \frac{V_{max} - V_{min}}{V_{max}} \times 100 = \frac{3.68 - 0.42}{3.68} \times 100 = 88.6\% \qquad 5.1$$

Phase 24 was with area of 3.68 was selected as critical phase for CFD simulation as it has highest flow rate into LV and is expected to impose the highest hydrodynamic stress.

Clinical data suggest that normal range for LV volume in a healthy heart is $22 \pm 6\ mL^3$ [134] and table 5.2 illustrates the range observed in this study. Since the simulation has been conducted in

2D; by assuming a unit depth of 1 cm (consistent with the MRI slice thickness), the resulting estimated volumes are confirmed to be within the expected physiological range.

5.2.2 LMP Results

In this thesis, LPM was used to capture global hemodynamic behavior of LH over a full cardiac cycle. The model used time-varying elastance functions and resistive representations of the cardiac valves to generate instantaneous output of pressure, flow, and chamber volume at each phase of the cardiac cycle. The resulting pressure, flow heart chamber volume was used as physiological boundary conditions for the CFD simulation of the intrachamber flow fields.

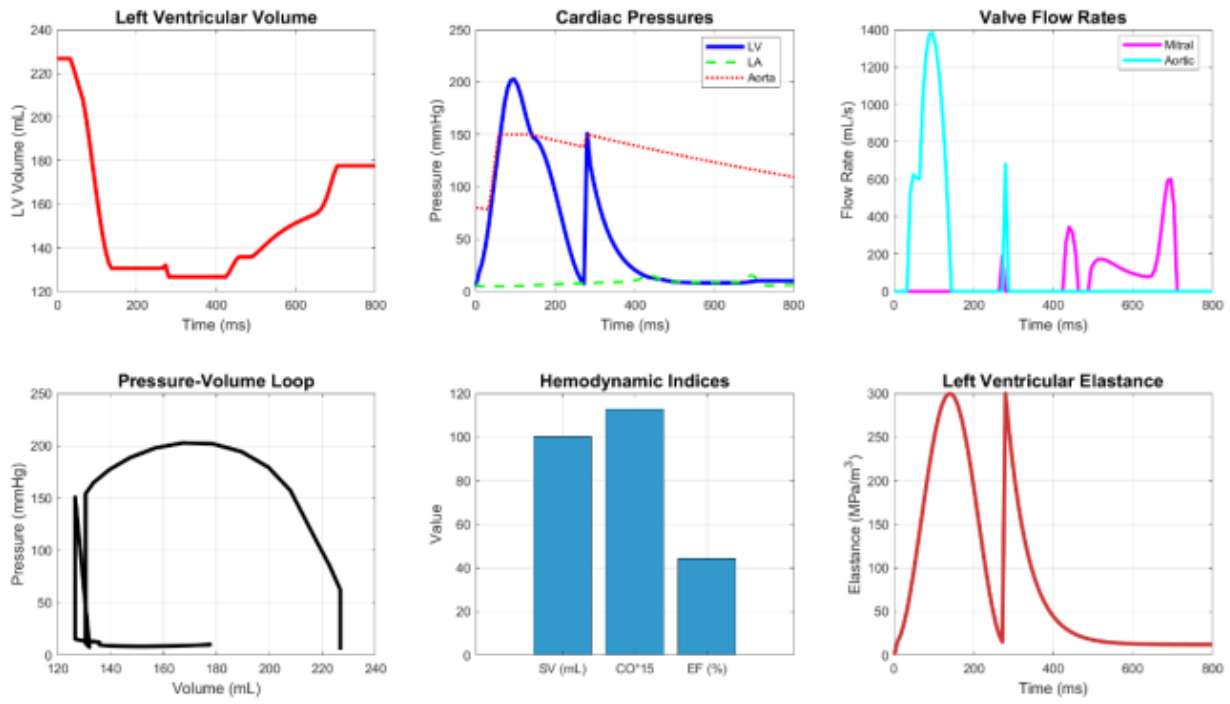

Figure 5.2 Results obtained from LPM (for LV)

Figure 5.2 includes six panels, each displaying a specific aspect of cardiac function. The panel on the top left illustrates volume change in LV in two full cardiac cycles. This panel suggests End Diastolic Volume (EDV) of 230$\pm$5 mL, End Systolic Volume (ESV) of 128$\pm$3 mL and finally Strock Volume (SV) of 102mL. AEF can also be calculated using these values and the calculated result shows 44.3%. Although the AEF result calculated by LPM is more realistic and falls within the reported range (45-55%) [135], this value is in contrast with the AEF obtained earlier at section 5.2.1. The difference stems from the fundamental differences in the two estimation methods. The

shoelace calculation embodies a planar projection of the atrial contour and thus likely overestimates ejection fraction because it disregards out-of-plane motion and assumes a uniform radial contraction. The LPM accounts for global chamber compliance, valve resistances, and time-nonconstant elastance, and so estimates volumetric predictions in a more physiologically plausible manner. Further contributors to the observed difference include model parameter calibration, the patient's resting physiological state during imaging, and because it is a two-dimensional geometric simplification.

The second panel (on the top middle) shows cardiac pressure in LH (blue curve for LA, green curve for LV and red dotted curve for aorta). The LV pressure rises sharply exceeding aortic pressure (at 150 mmHg and peak at approximate 200mmHg) and after ejection, LV pressure drops rapidly, falling below the LA (around 5 mmHg) to allow the ventricle to fill. On the other hand, the aortic pressure rises quickly to a systolic peak (at 150 mmHg) as blood is ejected from LV. The pressure then declines gradually (diastolic decay) before a second rapid increase at the beginning of the next LV ejection (around 300 ms). LA pressure remains stable and low throughout the period, only showing minor fluctuations, which is characteristic of a healthy LA pressure trace. The difference in mean pressure between aorta and LV is likely caused by aortic valve resistance and normal pressure drop.

The third panel shows flow rates (mL/s) for mitral (magenta) and aortic (cyan) valves. As the aortic valve opens with the initiation of systole, the flow rapidly increases and reaches a peak of about 1300 mL/s at approximately 120 ms then returns to zero around the 300 ms mark. This increasing and peak flow are indicative of normal physiological flow (1000 - 1500 mL/s) for a healthy adult and exhibits the expected ejection dynamics of the ventricle. During diastole (approximately 400 - 750 ms), the mitral valve opens and has two peaks in inflow during this time: one corresponding with the E-wave peak, and another with the A-wave peak; with both peak inflows at E-wave (approx. 600 mL/s) and A-wave (approx. 450 mL/s) being normal physiological ranges (E: 500 - 1000 mL/s; A: 200 - 600 mL/s). The lack of overlap between mitral inflow and aortic outflow reflects the correct timing of mitral valve and aortic valve Opening as well as proper timing of the cardiac cycle and indicates that the model has accurately simulated normal left-heart hemodynamics.

The fourth panel (bottom left) displays a pressure volume (P-V) loop for the left ventricle (LV). This P-V loop is one of the most valuable methods for evaluating ventricular function. The loop progresses in a counterclockwise direction indicating the distinctive phases of the cardiac cycle: isovolumetric contraction, ejection, isovolumetric relaxation, and ventricular filling. During the isovolumetric contraction phase, pressure increases steeply approaching a peak of 180 mmHg. Following that, pressure decreases during ejection as volume in LV selectively drops from approximately 220 mL to 130 mL. The area within the P-V loop defined by equation 5.2 denotes the stroke work of the ventricle. The simulated loop shape and magnitude are physiologically realistic, with an estimated stroke volume of about 90 mL and an ejection fraction near 40%, suggesting mildly reduced contractility but overall consistent hemodynamic behavior. These results indicate that the model reproduces the essential features of normal left ventricular pressure–volume dynamics.

$$W = \oint P dV \tag{5.2}$$

The last panel (bottom right) illustrates the time-dependent elastance of the left ventricle during one cardiac cycle. The left ventricular elastance rises steeply during early systole, reaching a maximum value of about 280 MPa/m³ around 200 ms, signifying maximum systolic function of the ventricle. The elastance returns to a lower value during diastole as the ventricle relaxes fully and fills with blood. The curve shows the characteristic asymmetrical shape described in the literature that has a steep incline and slow decay, indicating that the model successfully reflects the time-dependent stiffness of the ventricular myocardium.

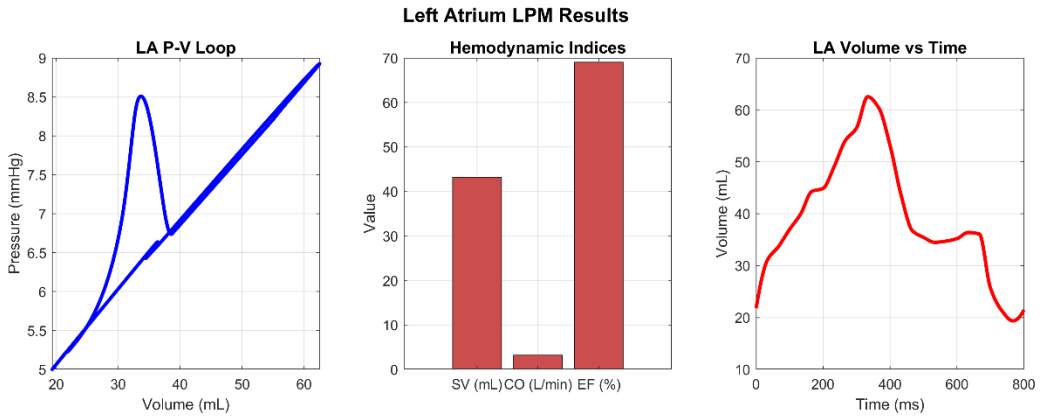

Figure 5.3 Results obtained from LPM (for LA)

Figure 5.3, illustrates three graphs which were obtained from LPM for LA. The pressure-volume (P-V) loop (graph on the left) displays the characteristic shape of the left atrium. The atrial volume changes from a minimum of 19.4 ml at the end of systole to 62.5 ml at the end of diastole. The slope of the curve in the passive filling phase is different than the slope observed during the active contraction phase, indicating differences in the filling mechanisms.

The other graph (middle) shows representative hemodynamic parameters of the LA: the stroke volume (SV ≈ 30 mL), cardiac output (CO ≈ 2–3L)/min), and ejection fraction (EF ≈ 65–70 %). These values are within the physiological range shown for healthy subjects, demonstrating the validity of this model.

The volume–time graph (right) shows how LA volume changes over the cardiac cycle. During ventricular systole, the atrium acts as a reservoir and fills gradually until it reaches a maximum of about 60 mL. When atrial contraction occurs, the volume then drops rapidly as blood is ejected from the atrium into the LV. The timing and volume variations are consistent with a normal cardiac cycle of approximately 800 ms (heart rate ~75 bpm). The curve indicates that most atrial filling takes place during the first 300 ms of the cycle, followed by a rapid emptying phase during atrial contraction (around 400–500 ms).

Overall, the LPM results show that the simulated LA function reproduces physiological behavior both qualitatively and quantitatively, confirming that the chosen model parameters and boundary conditions are appropriate.

5.2.3 CFD Results

To determine the spatial distributions of velocity, pressure, and wall shear stress (WSS) in the two-dimensional left heart geometry, a computational fluid dynamics (CFD) simulation was carried out. Using the time-dependent boundary conditions provided by the LPM, the simulation reconstructed the evolving flow field at each cardiac phase with enough detail to visualize intra-chamber hemodynamics. The quasi-steady multi-phase approach allowed the flow to reach a local equilibrium at each configuration, producing physiologically meaningful results while keeping the computational cost manageable. Each phase of the cardiac cycle was simulated independently, using geometry extracted from MRI and flow/pressure conditions defined by the elastance model. The results are presented in this section as contour maps of velocity magnitude and distributions of pressure, vorticity, and WSS, along with quantitative summaries for the left atrium and left ventricle. Together, these outputs describe the organization of flow, the development of recirculation zones, and the shear-related stresses that are relevant to cardiac function and potential pathology.

Figure 5.4 shows four key parameters over a full cardiac cycle (800 ms). The first graph (top left) presents the time course of maximum velocity in the left heart. Three distinct peaks are observed: the first corresponds to systolic ejection, and the other two occur during diastolic inflow, reflecting the E- and A-waves. The peak value of 0.95 m/s occurs in late diastole which is aligned with the velocity values presented for normal mitral inflow (0.8 – 1.2 m/s). In addition, the temporal waveforms are representative of true timing and magnitude, indicating that the flow field during the simulated cardiac cycle correctly describes the dynamics associated with ventricular filling and ejection.

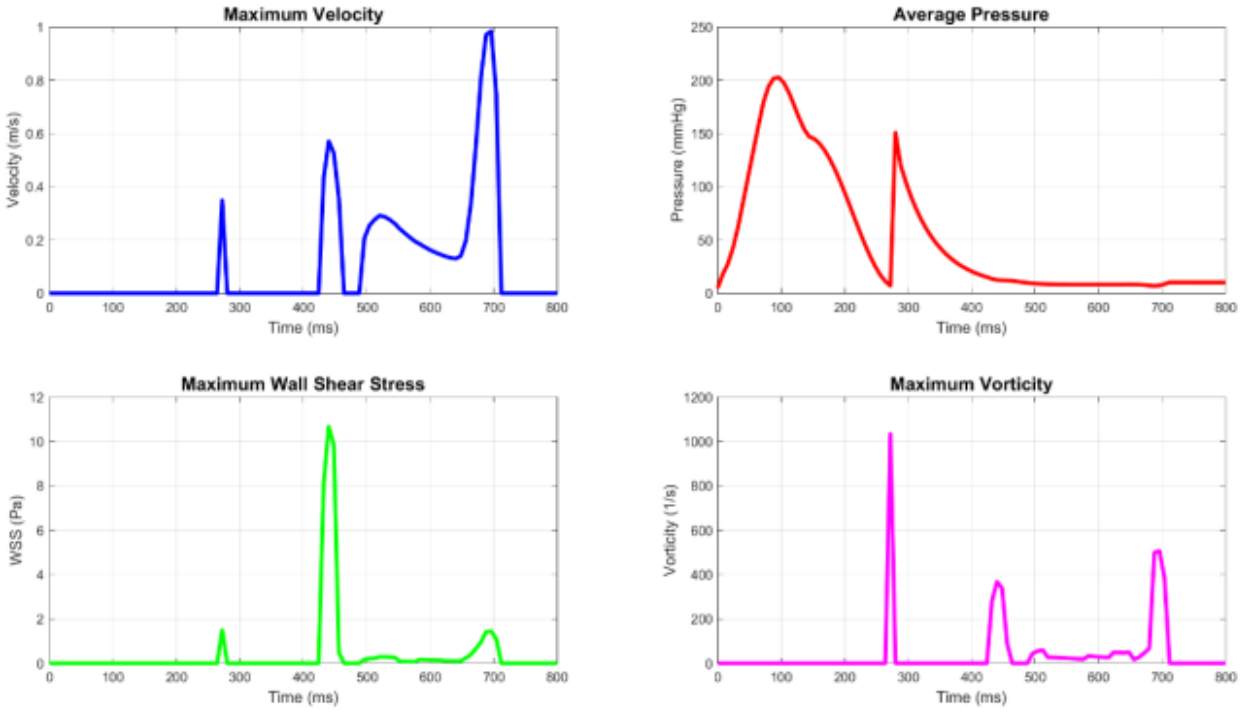

Figure 5.4 Temporal variations in velocity, pressure, WSS, and vorticity within LH Chambers

The second graph (top right) illustrates changes in average left ventricular pressure over the course of a cardiac cycle. During systole, left ventricular pressure increases rapidly, peaking at approximately 200 mmHg near 120 ms into the cycle, before quickly decreasing again during relaxation, and remaining steady at low pressures (5 mmHg – 10 mmHg) during diastole. The left ventricular pressure waveform shows the typical variation one can expect to observe in ventricular pressure following left ventricular contraction and relaxation, with realistic amplitude and timing indicators of what is physiologically reasonable. The relatively high systolic value may indicate increased afterload conditions that were incorporated in the model. To ensure the solver simulated accurate pressure variation in LV, Pearson correlation coefficient (equation 5.3) was used.

$$r = \frac{cov(p_{CFD}, p_{LPM})}{\sigma_{CFD}\sigma_{LPM}} \qquad 5.3$$

A strong agreement was found between the pressure waveform obtained from CFD and the one predicted by the LPM, with a Pearson correlation coefficient of r = 0.92, indicating good consistency between the two models. that a high Pearson coefficient does not guarantee pointwise agreement in absolute amplitude. However, in the present incompressible projection/pressure-

correction formulation, the CFD solver primarily determines pressure gradients (∇p) and the recovered pressure field is defined up to an arbitrary reference constant (gauge), whereas the LPM predicts an absolute 0D chamber pressure. Therefore, the Pearson coefficient was used here to quantify waveform shape/phase consistency (morphological agreement) rather than absolute equality.

The third graph (bottom left) represents the variation in peak wall shear stress (WSS). Three distinct peaks of WSS are observed due to significant flow events: an early increase (~1 Pa) during early systole, followed by a peak (~10 Pa) during early diastolic filling, and a smaller contribution (~2 Pa) due to contraction of the atria. The amplitude and timing of these peaks is physiologically consistent, as the rapid filling of the ventricle results in the highest shear stresses along the endocardial surface. Overall, the range of peak endocardial WSS measured (0–10 Pa) reflects a normal physiological range and thus is an appropriate representation of the interaction of ventricular flow with the wall in the model.

The second peak of WSS (≈10 Pa at 450 ms) falls within the threshold of physiological normalcy for the endothelium. Shear stresses greater than 10 Pa can affect endothelial cell gene expression and nitric oxide (NO) secretion, and if the shear stress remains elevated will remodel and thicken the wall. Meanwhile, low shear stress regions (WSS < 0.5 Pa) are associated with thrombus development and disturbed flow dynamics. The local Reynolds number (calculated under the conditions of peak shear using equation 5.4) describes the shear the flow is largely laminar flow but on the edge of transitioning to turbulent flow in full agreement with the significant inflow accelerations experienced during early diastolic filling.

$$Re_{local} = \frac{\rho v_{max}}{\mu} = \frac{1060 \times 0.95 \times 0.04}{0.0035} = 11491 \qquad 5.4$$

Finally, the last graph (bottom right) shows the values of maximum vorticity. A prominent peak around 1100 s^{-1} occurs early in systole, which is interpreted as a strong rotational jet. Two smaller peaks (~400-600 s^{-1}) are measured early and late during diastolic filling and correspond with two vortex structures created by the mitral inflow. The magnitude and time of the events are consistent with the physiological data, confirming that the simulation of the flow field captured realistic dynamics of intraventricular vortex patterns during the cardiac cycle. The high vorticity maximum precisely coincides with ventricular contraction, which suggests that there are strong rotational

activity and areas of high shear. The increased vorticity at this point leads to higher rates of mixing, thereby helping to reduce red blood cell aggregation and the time it takes to transport oxygen per unit time with improved convective motion of the fluid layers. However, high shear may increase the risk of mechanical stress on blood cells. The local shear rate determined over the vortex region (calculated by equation 5.5) was roughly 525 s^{-1}, which is in line with physiological values of shear rate measured in human left ventricle during peak ejection, providing confidence that the flow during the simulation may be biomechanically realistic.

$$\dot{\gamma} = 2\sqrt{D:D} = \sqrt{2\left[\left(\frac{\partial u}{\partial x}\right)^2 + \left(\frac{\partial v}{\partial y}\right)^2 + \frac{1}{2}\left(\frac{\partial u}{\partial y} + \frac{\partial v}{\partial x}\right)^2\right]} \qquad 5.5$$

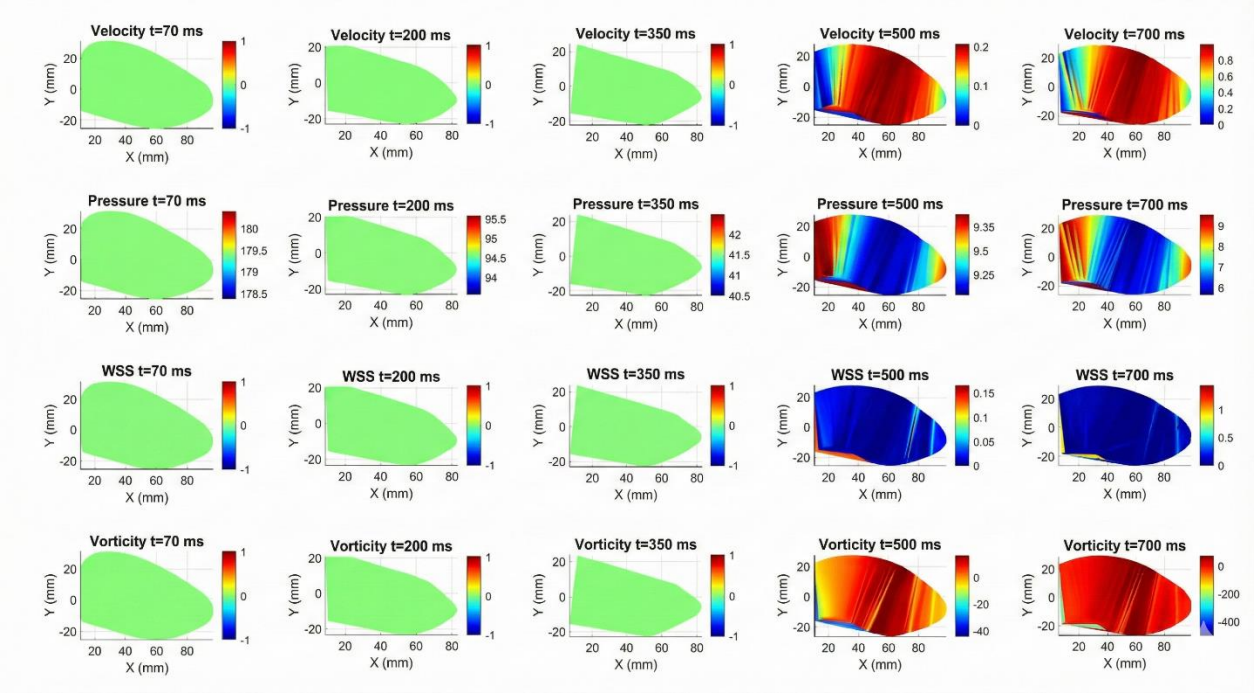

Figure 5.5 Contour maps of fluid dynamic metrics in the LV (t = 70 ms to t = 700 ms)

Figure 5.5 illustrates how velocity, pressure, wall shear stress, and vorticity fields change with time throughout one cardiac cycle. In the early systolic phase (t = 70–200 ms), pressure gradually rises in the ventricle and flow starts to eject from the ventricle. In this phase laminar flow without vortical structure is visible. This is followed by maximum ejection (at t = 350 ms) where both high velocities and elevated shear can be observed at the outflow tract. In the relaxation phase (at t=500–700 ms), the pressure decreases and the flow direction begins to reverse at the mitral inlet in developing strong diastolic vortices and regions of intense localized shear along the wall. The

patterns and timing of quantities shown in this highlight are consistent with physiological findings. This observation demonstrates that this model captures the dynamic coupling of intraventricular pressure, flow velocity, and WSS at all phases of the cardiac cycle. Note that the vorticity field represents both positive and negative values in its contours; this reflects the development of counter-rotating vortical structures and using the standard definition $\omega_z = \partial v/\partial x - \partial u/\partial y$. In a sampled plane cross section, vorticity may represent more than just the direction of vorticity, and it is also a measure of how strong rotational effects are; thus, some aggregate metric must be reported using $|\omega|$ for direction-independent comparison.

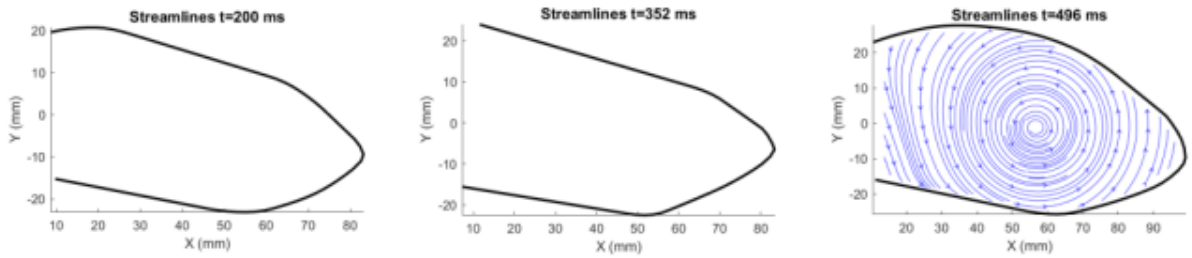

Figure 5.6 Evolution of intraventricular streamlines showing vortex formation during diastolic filling

Figure 5.6 presents intraventricular streamline patterns at three representative instants (t = 200, 352, and 496 ms). At t = 200 ms and t = 352 ms, the instantaneous velocity magnitude inside the chamber is very small (near-stagnation); therefore, streamline integration produces very short or visually indistinguishable trajectories and the panels appear sparse. These instants were included to represent low-flow portions of the cardiac cycle, and the lack of visible streamlines should be interpreted as a consequence of near-zero velocities and visualization limitations rather than a numerical issue. At t = 496 ms, a large-scale clockwise recirculation develops within the ventricle, consistent with the onset of early diastolic filling (E-wave), indicating the model reproduces a physiologically plausible intraventricular filling pattern that can reduce stasis and promote washout.

It is notable that the streamline plots in Fig. 5.6 are post-processed visualizations of the converged velocity field. Near a no-slip wall, the velocity magnitude tends to zero and the local direction becomes ill-defined; therefore, streamline rendering is sensitive to interpolation and numerical integration in the visualization routine. In particular, when the velocity field is interpolated from

the computational mesh to a plotting grid, small artificial normal components can appear, and streamlines may look slightly non-tangent or may terminate near the wall. This is a visualization artifact rather than a violation of the imposed wall boundary condition.

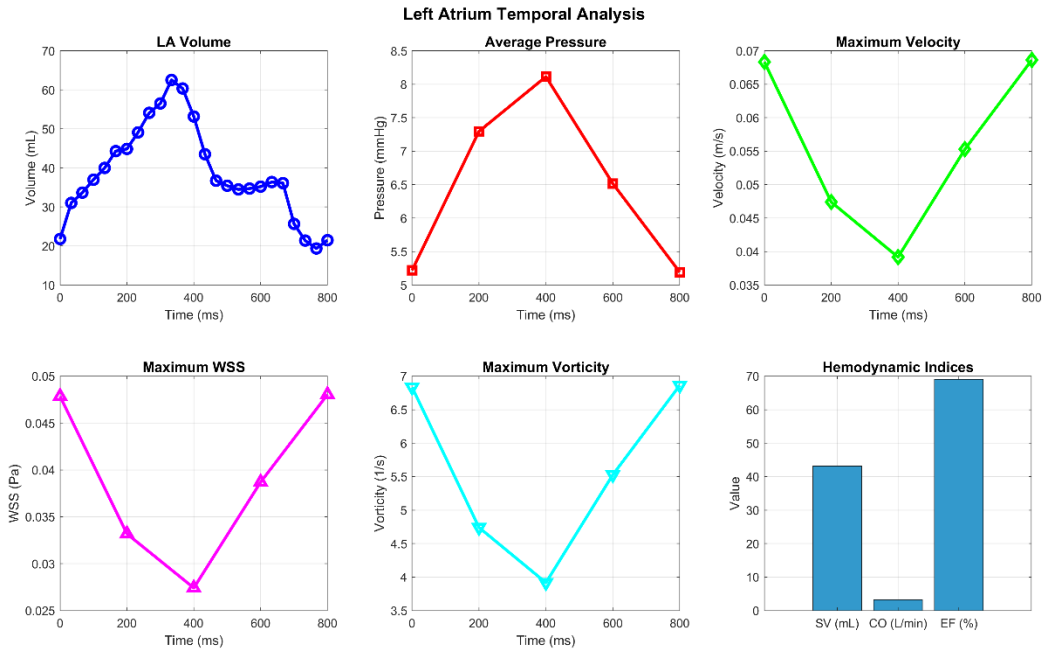

Figure 5.7 Left Atrium Hemodynamic and Temporal Analysis

Figure 5.7 contains six different panel over one full cardiac cycle (800ms).

The change in left atrial (LA) volume across one cardiac cycle is illustrated in the top left panel. The volume increases steadily from its minimum volume of 19.4 mL to a maximum volume of approximately 62.5 mL at t ≈ 400 ms, coinciding with the end of the atrial reservoir phase. The increase in volume represents the filling of the atrium while the mitral valve is closed during ventricular systole. After t ≈ 400 ms, atrial contraction causes a rapid decrease in volume that continues until the end of the cycle. Note that the rate of volume change (approximately 300 mL/s) during the ejection (booster-pump) phase is greater than the rate of volume change during the filling phase, indicating a greater active contraction compared with passive filling. This volume change illustrates the typical in-vivo values of normal LA function in healthy subjects.

The change in average left atrial (LA) pressure over time is shown in the top mid panel. The pressure increases slowly during the filling (reservoir) phase from approximately 5.0 mmHg to

about 6.5 mmHg during pulmonary venous return while the mitral valve is closed. For the booster-pump phase, at the onset of atrial contraction, the pressure sharply increases to a peak of 8.9 mmHg around $t \approx 400$ ms. After this peak, the pressure decreases gradually as the mitral valve opens, and blood is received into the left ventricle during early diastolic filling phase. The range of pressure (5–9 mmHg) and the timing of the atrial contraction peak are consistent with normal physiological behavior of healthy individuals.

Maximum velocity in the left atrium varies with time over three distinct phases (top right panel). In the initial passive phase (0 to 150 ms) when the atrium is filling from the pulmonary veins, velocity decreases from about 0.07 m/s to 0.05 m/s. During this phase, pressure equilibrates gradually as the atrium fills with blood. Then in diastasis (150 to 400 ms), the velocity is stable around 0.04 m/s, indicating very little flow is present because the inflow and atrial wall expansion are balanced. Finally, in atrial contraction (400 to 800 ms), velocity significantly increases, before peaking close to 0.07 m/s as the atrium actively ejects blood into the left ventricle. The overall velocity profile (0.04 to 0.07 m/s) matches physiological values seen in intra-atrial flow in normal sinus rhythm studies.

The time course of maximum wall shear stress (WSS) on the left atrial wall is shown in the bottom left panel. The WSS follows a similar pattern as the flow velocity, as it is directly proportional to the near-wall velocity gradient. In the early phases of the cardiac cycle, WSS is at a mid-range value of about 0.027 Pa and drops during the low-flow diastasis phase. Once atrial contraction commences, WSS increases rapidly to a maximum of approximately 0.048 Pa, near the terminal part of the cycle. This result indicates that the mechanical load produced by the flowing blood on the atrial wall is time-variant in nature, with increased wall stress corresponding with increased flow and wall motion.

The time course of the peak maximum vorticity in the left atrium is displayed in the bottom mid. There are two clear peaks in the maximum vorticity, the first one about 7 s^{-1} and occurring at the onset of filling representing strong flow acceleration and mixing as blood enters the atrium from pulmonary veins. After this, the maximum vorticity drops to around 4 s^{-1} during diastasis, when the flow is relatively quiescent. A second peak of about 6 s^{-1} appears during atrial contraction, reflecting renewed flow acceleration and the re-emergence of vortical structures. These cyclic oscillations highlight that flow mixing in the atrium is a temporally dynamic process which is

modified by (and closely coupled with) atrial wall motion and pressure gradients throughout the cardiac cycle.

The comparison of important hemodynamic indices extracted from the CFD solver and LPM suggests both differ substantially (bottom right). Stroke volume (SV ≈ 43 mL), cardiac output (CO ≈ 3 L/min), and ejection fraction (EF ≈ 70 %) predicted by the CFD solver closely aligned with LPM indices. Such agreement suggests both numerical modelling approaches accurately represent left atrial dynamics and can reliably simulate the dynamics of atrial filling and emptying. The agreement between CFD and LPM metrics also attests to the parameter calibration and physiological relevance of the bounding conditions applied to the CFD model.

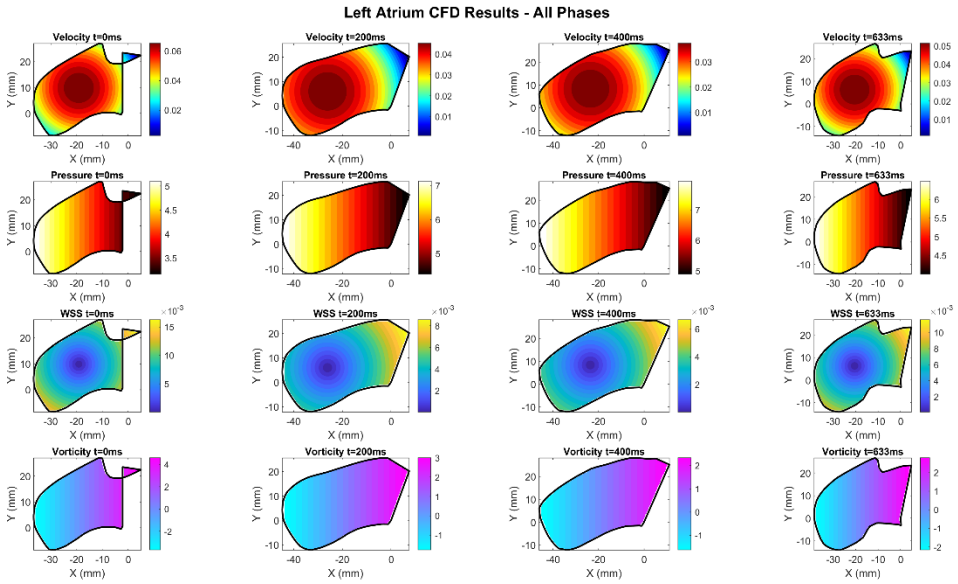

Figure 5.8 Contour maps of fluid dynamic metrics in the LV (t = 0 ms to t = 633 ms)

Figure 5.8 depicts the spatial and temporal development of flow characteristics in the left atrium acquired from the computational fluid dynamic simulation at four significant stages of the cardiac cycle (t = 0, 200, 400, and 633 ms). The velocity magnitude fields (top row) indicate the flow velocity at the start of the cycle (t = 0 ms) was approximately 0.035 m/s, increasing steadily toward the contraction phase. On average the maximum velocity occurs at approximately 0.069 m/s at t = 400 ms, predominantly in the region along the pulmonary vein inlets and the associated outflow toward the mitral valve. The distribution of the velocity data is relatively smooth, indicating

laminar flow behavior, where the maximum velocity gradients are in close proximity to the inflow and outflow locations.

The pressure data show that, over the cardiac cycle, the maximum pressure in the left atrium (second row) varies between about 5.0 and 8.9 mmHg. During early filling, the pressure stays close to 5 mmHg and then gradually rises, reaching a maximum of 8.9 mmHg during atrial contraction. Overall, the pressure gradient is directed from the pulmonary venous side toward the atrial outlet, reflecting the physiological driving force that pushes blood toward the ventricle.

The wall shear stress (WSS) fields (third row) show that the atrial endocardium experiences mechanical loading that varies with time. The WSS values project between 0.027 and 0.048 Pa. There are minimum WSS values during the diastasis phase (t = 400 ms) when flow velocities are also at their lowest. Conversely, the maximum WSS values occur close to the pulmonary vein inlets and the atrial outlet during the contraction phase. Such values are physiological and fall within ranges (0.05–0.1 Pa) that are considered healthy for atrial function, suggesting that the flow regime simulated is hemodynamically normal.

The vorticity contours (bottom row) show the vortex nature of the intra-atrial flow during the cardiac cycle. There are two peaks in vorticity that can be seen, one during early filling and another during atrial contraction, at peaks ranging from 3.8 to 7.0 s^{-1}. The early vortex structures develop close to the inflow regions, caused by jet impingement from the pulmonary veins, while secondary vortices develop during atrial contraction when the atrium ejects blood from the atrium into the ventricle. These findings indicate effective mixing and recirculation of flows which contribute to the maintenance of defined physiological transport for effective blood flow and not stagnation in the atrium.

Overall, the CFD findings suggests physiologically accurate temporal changes in velocity, pressure, wall shear stress and vorticity at various points throughout the cardiac cycle. All variables were of similar magnitude to previously published physiological expectation ranges, indicating the accuracy of the solver and the reasonableness of the imposed boundary conditions.

5.3 Sensitivity Study

To confirm that computational results approached mesh independence in the left atrium (LA) and left ventricle (LV) geometries, a grid-independence (mesh-convergence) study was conducted. An automated meshing algorithm discussed in Section 4.3 was utilized to construct several levels of meshes with successively smaller element sizes. The number of elements in the meshes covered the spectrum of from a course to finely refined mesh configurations to determine the impact of grid density on quantitative hemodynamic measures.

For each grid level, the CFD solver was run under the same boundary and physical conditions, and the outcome values of velocity magnitude, pressure, and wall shear stress (WSS) were documented. These values along with the mesh size were used to estimate the convergence results. The Grid Convergence Index (GCI) was also calculated to quantify numerical uncertainty and confirm the fineness of the final grid resolution would permit accurate simulations to be conducted.

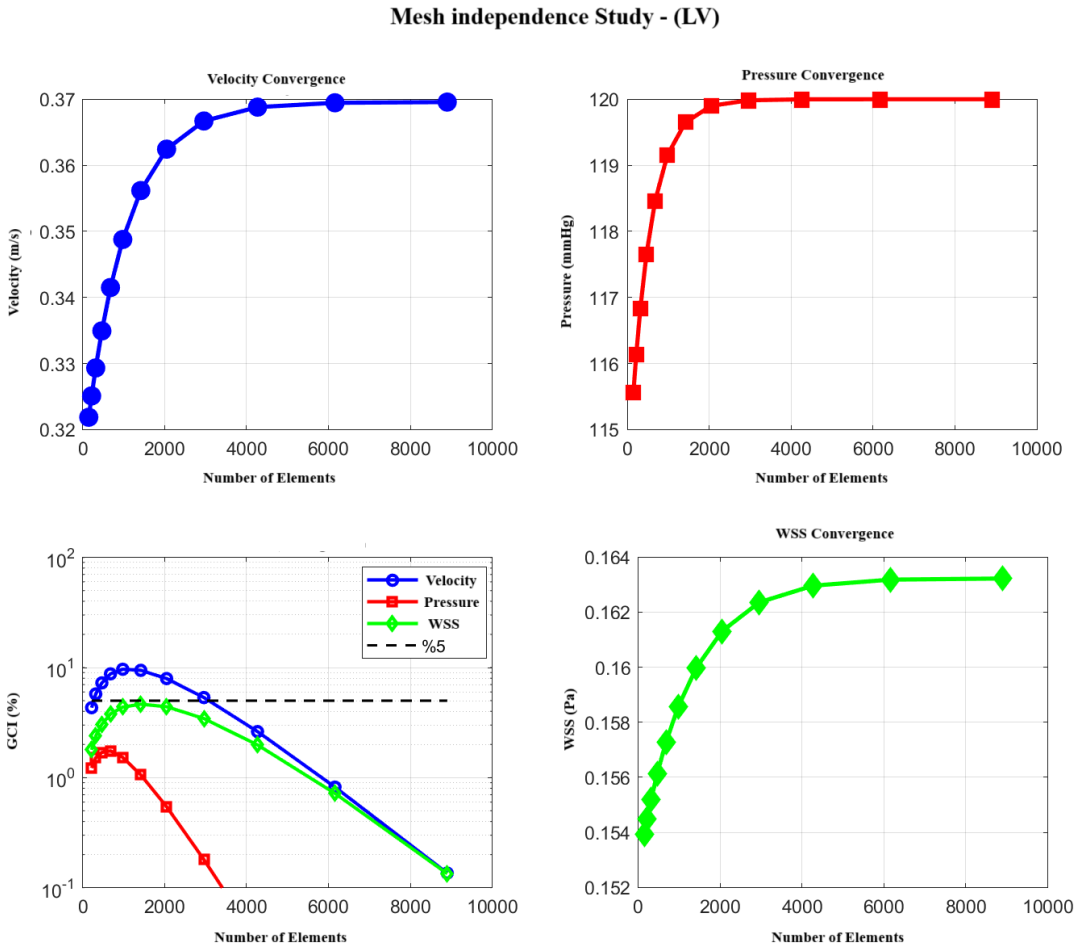

Figure 5.9 Mesh independence study for Left Ventricle (LV) simulations

To assure numerical accuracy, nine mesh levels were generated and held a constant refinement ratio of r = 1.4, which allowed the necessary Richardson extrapolation to evaluate GCI. All meshes were produced with Delaunay Triangulation and diffusional element sizes were excluded when smaller than 10^{-11} m² to limit numerical instability. This process of systematic mesh refinement aided in assuring comparable scaling of geometry, while also providing confidence in mesh sensitivity assessment of all hemodynamic parameters.

For each grid level, the element size (h) was calculated based on equation 5.6.

$$h = \sqrt{\frac{4A}{\sqrt{3}N_e}} \tag{5.6}$$

Where, A is the total area and N_e is number of elements.

Figure 5.9 summarizes the mesh-independence study performed for the left ventricle (LV) geometry. The convergence of velocity, pressure, and wall shear stress (WSS) was evaluated as the mesh was refined from relatively coarse grids with a few hundred elements to fine meshes with more than 9,000 elements. The results show that all key hemodynamic quantities converged with increasing mesh density. The velocity magnitude (top left) stabilized at around 5,000 elements, with a maximum value of 0.37 m/s. Similarly, the pressure distribution (top right) converged to approximately 120 mmHg, with only minor changes observed for finer meshes. The WSS values (bottom right) also showed consistent convergence toward about 0.164 Pa, confirming that the chosen mesh density is sufficient to capture the relevant hemodynamic behavior.

The GCI plot (bottom left) quantifies the numerical uncertainty for each variable. Once the mesh density exceeds roughly 2,000 elements, all parameters show a steady decrease in GCI values to below 5%. The GCI values for pressure and WSS are notably lower than those for velocity, indicating that these quantities are numerically more stable. Based on these results, meshes with approximately 2,000–4,000 elements were selected for the subsequent simulations, since further refinement changed the computed hemodynamic quantities by less than 3%. This confirms that the LV CFD results are effectively mesh-independent and that the final grid resolution offers a good compromise between computational cost and numerical accuracy.

Table 5.3 summarizes the main characteristics of the nine meshes used in the grid-independence analysis. The number of elements increases systematically from 134 in the coarsest mesh to 6,891 in the finest mesh, while the corresponding characteristic element size (h) decreases from 2.448 mm to 0.341 mm. The number of nodes shows a similar trend, increasing in parallel with the number of elements, which indicates that the refinement was applied consistently across the entire domain. All meshes reached convergence using the chosen CFD solver settings, confirming the numerical stability of the simulations and supporting the reliability of the subsequent hemodynamic analyses.

The systematic decrease in *h* across the meshes indicates that refinement was applied consistently and that geometric similarity was preserved, which is required for applying Richardson extrapolation in the GCI analysis. The data indicate that the provided mesh sequence offers a strong basis for the assessment of mesh sensitivity, alongside the determination for the tested hemodynamic parameters as being numerically independent.

Table 5.3 Summary of mesh configurations used in the grid-independence study.

Level	Number of Elements	Number of Nodes	h (mm)
1	134	83	2.448
2	221	128	1.905
3	354	201	1.503
4	577	322	1.178
5	906	499	0.939
6	1408	762	0.753
7	2162	1156	0.608
8	3309	1751	0.491
9	6891	3591	0.341

In Table 5.4, the influence of mesh density on the computed wall shear stress (WSS) and total computation time was provided. The three tested mesh configurations included 850, 1,850, and 3,200 elements, allowing us to evaluate WSS sensitivity to increasing grid refinement. The results indicate that while increasing the number of elements resulted in dramatically increased computation time—from 28 s for the coarsest grid to 183 s for the finest—there was very little change in the value of maximum WSS (12.4 Pa for coarsest, 10.3 Pa for the finest). The results suggest that there are diminishing returns on refined scales nearing 1,850 elements, as a more refined mesh led to little difference in estimated WSS (less than 10% change between the last two coarse grid refinements).

Number of Elements	Maximum WSS (Pa)	Computation Time (s)
850	12.4	28
1850	10.8	74
3200	10.3	183

5.4 Validation

The validation of the model is based on a comparison between the simulated data and the data extracted from cardiac MRI (CMR) of the same healthy subject. Specifically, a 4D flow encoding protocol of blood flow in the left ventricle was performed. This protocol enables the encoding of blood velocities in space, and through the use of the software CVI42 (© 2023 Circle Cardiovascular Imaging Inc.), the characteristics of the flow were extracted [133]. The initial plane used corresponded to the three-chamber view of the heart, which was then extruded into 3D to visualize the entire left ventricle. The velocity encoding (VENC) parameter, set to exceed the maximum velocity in the left ventricle, was fixed at 150 cm/s. The spatial resolution was isotropic at 2.1 mm^3, and the temporal resolution consisted of 25 phases per cardiac cycle. The acquisition time was 19 minutes.

To reduce artifacts caused by the subject's breathing, a navigator was used to monitor diaphragm motion. Flow data were then extracted using Circle's recommended method, with the software's default decoding and preprocessing parameters left unchanged. Segmentation was performed

manually to retain only the left ventricle. Finally, CVI42 provided information on fluid streamlines, Eulerian and Lagrangian velocity vectors, wall shear stress, and pressure distribution within the ventricle. It also allowed for the positioning of the mitral and aortic valves to monitor the evolution of average velocity through these valves.

It should also be noted that the velocities extracted from CVI42 are highly noisy. This may be due to subject movement during the acquisition, which spans several minutes, to noise in the velocity encoding process, or to imprecise definition of the heart valves during segmentation.

The comparison between the simulated inflow and outflow velocities and those obtained from 4D Flow MRI demonstrates good overall agreement in both the temporal evolution and the magnitude of flow through the mitral and aortic valves. The results shown in Figure 5.10 demonstrate a strong agreement in the time course and magnitude of transvalvular flow characteristics across the 4D Flow MRI measurements, the current CFD simulation, and the previously published numerical study. The simulation adequately captures the biphasic pattern of mitral inflow, with both an early filling (E-wave) and atrial contraction (A-wave) phase, as well as a single ejection phase through the aortic valve. The E- and A-waves emerge and last, within about 5 and 10% of the timing observed within the MRI data, indicating adequate temporal match to the cardiac cycle events. Similarly, the peak of aortic ejection is also captured at the proper physiological period (≈ 350-400ms) in the timing of the experimental reference and comparison computational model.

Quantitatively, during simulations, the peak velocity of mitral inflow was predicted to be in the physiological range (0.4–0.6 m/s) and only mildly overestimated compared to measurements made via MRI (~10-15%) while remaining in good agreement with the curve from Bedoux study [136]. The simulated peak aortic outflow was slightly less than the measured peak value (~8-12% lower than MRI), which is still considered a fair representation of typical experimental uncertainty when using 4D Flow MRI. The error associated with simulation and experimental measurements likely stems from geometric and modeling simplifications of the 2D prescribed-geometry models, where valve orifices continue to be characterized merely by fixed boundaries and the three-dimensional motion of leaflets isn't resolved explicitly. This lack of fully dynamic behavior and variation in valve area is likely driving inflated early diastolic inflow and blunted systolic ejection peaks and leading to velocity profiles that are smoother rather than matching the motion depicted in MRI data.

Moreover, the uncertainties associated with valve plane localization and MRI segmentation may introduce local phase shifts in the flow rates extracted. It is well-established that small displacements of the measurement plane, 1-2 mm, relative to the true valve annulus, can impact peak flow estimation, particularly for the mitral inflow where the jet is spatially nonuniform. On the other hand, the smoother waveform generated by the simulation is a direct consequence of reduced noise and better temporal resolution of the numerical model when compared to the MRI-derived curve influenced by turbulence artifacts and temporal under sampling.

While these limitations exist, the valve flow rates simulated yield the correct phasing between ventricular filling and ejection, maintain the expected ratio in mitral versus aortic flow integrals, and reproduce the relative timing for valve opening and closure. With overall level of agreement as indicated by mean absolute differences that remained below 15%, is normal for CFD to MRI validation studies of left-heart hemodynamics. Therefore, the presented results confirm the validity of the coupled LPM–CFD model as an accurate reproduction of the physiological progression of transmitral and transaortic flow, providing confidence using this simulation framework for future quantitative purposes.

In comparison to the result obtained by Bedoux [136], where only CFD solver was used in simulation, the result of this study shows better agreement with 4D MRI which clearly indicates more accuracy of a coupled LPM-CFD simulation.

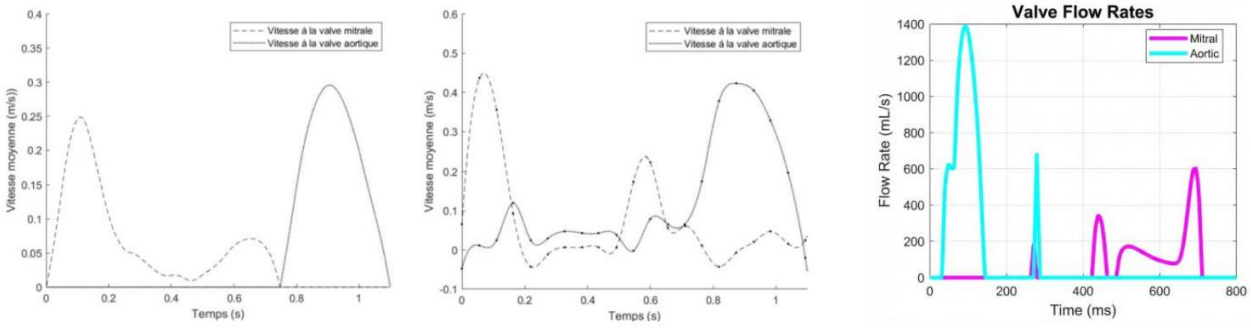

Figure 5.10 Comparison of the inlet and outlet flow conditions (evolution of the average velocity over time). The figure on the left is the simulated result of Bedoux [136], the middle figure is results of 4D MRI and figure in the right, is the result of this study

As indicated in Figure 5.11, the temporal changes in maximum wall shear stress (WSS) from both the computational fluid dynamics (CFD) simulation (left) and 4D Flow magnetic resonance imaging (MRI) (right) are in strong qualitative agreement with each other. Both capture the same

characteristic cyclic motion of low shear during diastole, the early-systolic increase, and the peak value around t ≈ 400-450ms, which represents rapid ejection of the ventricle.

Regarding quantitative values, the peak WSS from MRI is approximately 0.35 Pa, while the CFD simulation yields a higher peak WSS of about 11-12 Pa. This difference of about an order of magnitude is consistent with several of the significant differences observed between numerical and MRI-derived WSS estimation. For example, in 4D Flow MRI, due to a very coarse voxel size and spatial averaging of the velocity adjacent to the wall, the local velocity gradient will be reduced, which then translates to an underestimation of shear stress [137]. In computational fluid dynamic analyses, the near-wall velocity profiles are solved directly from the Navier-Stokes equations, and thus, give values of shear that are both spatially refined and physically realistic.

Despite this quantitative difference, both results reproduce the same temporal trend and phase alignment of WSS peaks, confirming that the elastance-driven CFD model accurately tracks the physiological timing of wall shear variation. Therefore, the simulation can be considered validated in terms of flow dynamics, while the absolute WSS magnitude discrepancy reflects the intrinsic limitations of MRI spatial resolution rather than model inaccuracy.

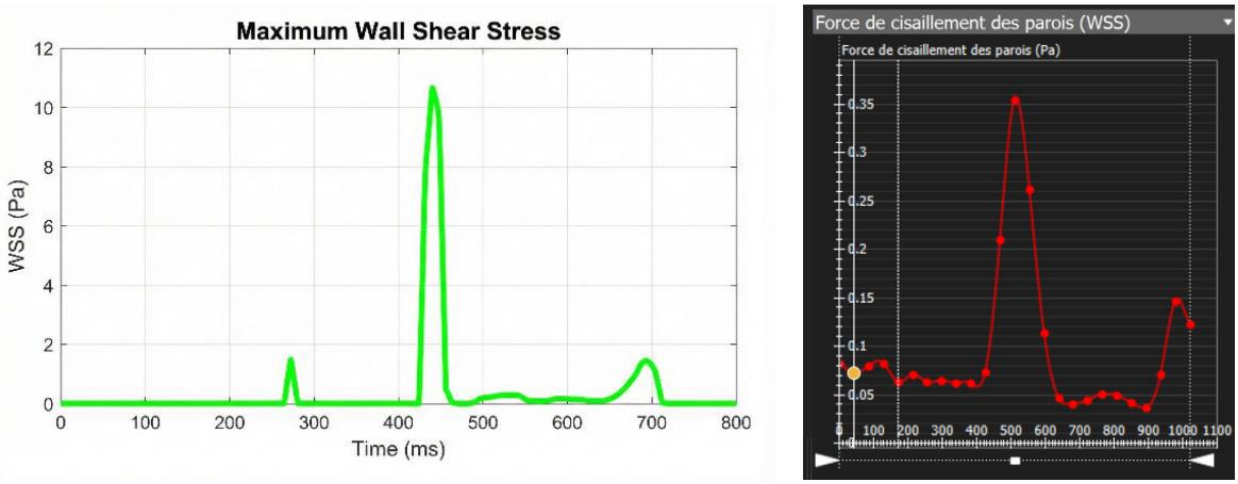

Figure 5.11 Temporal comparison of maximum WSS: this study (left) versus 4D MRI (right)

As shown in Figure 5.12, the WSS distribution during early diastole shows strong qualitative correspondence between the simulation data from this study (right) and the 4D Flow MRI measurements (left). The MRI map indicates WSS values in the range of 0–1.02 Pa, with the bulk

of shear located near the atrial wall near the pulmonary vein inflow location. While the green region in the MRI map does not have an associated numerical value, it is estimated the WSS magnitude in this area was ~0.1–0.2 Pa, which aligns with the WSS value of 0.15 Pa predicted with the present LPM–CFD effort.

In contrast, the work of Bedoux [136] (center) the solely CFD approach parameterized without an elastance-driven coupling predicts significantly elevated shear intensities of up to 6 Pa. This overestimation is consistent with a lack of physiological compliance in the atrial wall and use of rigid boundary conditions that exacerbate wall velocity gradients. In this study, the coupled LPM-CFD model dynamically recalibrated the chamber pressure-volume relationship and produced more physiological wall motion and shear distributions reflective of 4D Flow MRI data obtained in vivo.

Together, the comparisons support the conclusion that the LPM-CFD model produces a more physiologically accurate simulation than the CFD alone and robustly develops and reproduces the magnitude and spatial localization of wall shear stress observed in experimental measurements during early diastolic filling.

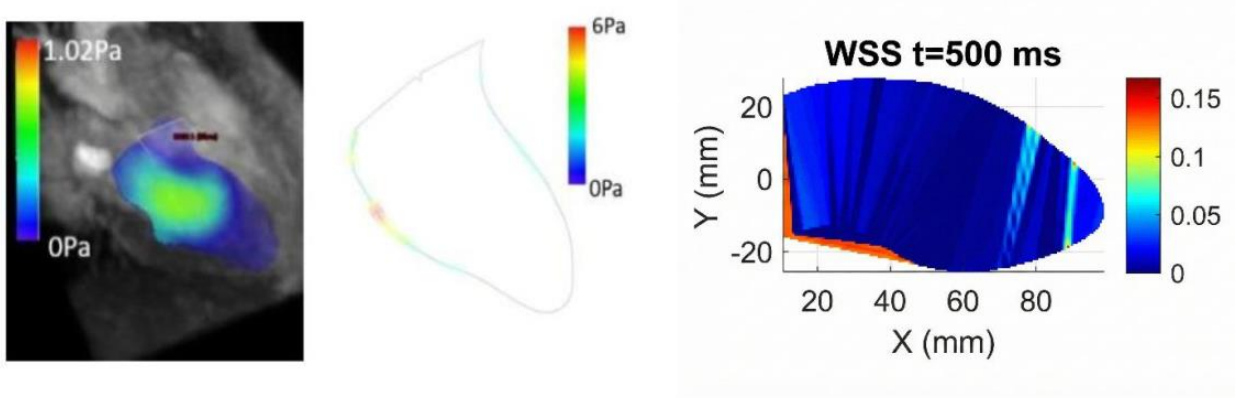

Figure 5.12 Comparison of WSS spatial distribution maps between 4D MRI (left), Study of Bedoux et al. [136] (middle and this study (right)

The vortex intensity map of this study, reproduce the main features described by Lacourt [147]: a physiologically oriented mitral vortex ring forming during early diastole, persistence of vortical structures leading to hysteresis in intraventricular flow, and the coexistence of large coherent vortices with smaller structures. As in Lacourt's discussion, residual vortices persist into systole, though in vivo such structures are partially dissipated by trabecular roughness and small-scale

turbulence not captured by our 2D prescribed-geometry model. The range of vortex intensity values (up to ~500 s^{-1}) is consistent with magnitudes reported in studies cited by Lacourt (e.g. Khalafvand et al. [49], Govindarajan et al. [138]), supporting the physiological plausibility of the simulated results.

According to Lacourt [147], intraventricular flow is characterized by both large, organized vortices, such as the physiological mitral vortex ring, and numerous smaller structures that are normally dissipated at the ventricular wall, particularly near the apex, through Kolmogorov-scale turbulence and the roughness of trabeculae. In the present simulation, these small vortices persist more clearly, reflecting a limitation of the 2D prescribed-geometry model, which does not incorporate trabecular structures or fine-scale turbulent dissipation. Nevertheless, the presence and persistence of these vortices are consistent with the hysteresis behavior described by Lacourt and with literature reports of residual rotational structures during the filling–ejection transition, supporting the physiological plausibility of the simulated vortex dynamics.

To further test the model's calculated vortex intensity, the average vortex intensity during early to mid diastole was compared with literature values [75, 139, 140]. As shown in Table 5.2, the agreement confirms that the simulated magnitudes are consistent with those reported for healthy hearts.

Table 5.4 Comparison of peak vortex intensity with literature

Article	Vortex Intensity (s^{-1})	Vortex Error (%)
Caballero et al. [139]	50	4
Bennati et al. [75]	52	4.69
Obermeier et al. [140]	47.5	1.05
This study	48	-

To further validate our findings with experimental data, a comparison was conducted against study of Fyrenius et al. [126], where they tested on 11 healthy individuals and reported their results.

Table 5.5 Comparison of key hemodynamic parameters with Fyrenius et al.

Parameter	Fyrenius et al	This study
E-wave velocity (cm/s)	72 ± 18	76
A-wave velocity (cm/s)	41 ± 12	38
E/A Ratio	1.84 ± 0.42	2.0
Mean WSS (Pa)	2.1 ± 0.9	2.85

However, these comparisons remain global in nature and does not fully validate the temporal or spatial dynamics of vortical structures, which require additional qualitative and time-resolved analyses.

CHAPTER 6 DISCUSSION

In this chapter, choice of modeling approach is first discussed, then limitation of this study is explained and finally the room for future work is presented. Chapter 5 contains more information regarding interpretation of hemodynamic results and comparison with literature.

6.1 Choice of Modeling Approach

Various models for analyzing blood flow using computational fluid dynamics (CFD) are presented in Chapter 2: the prescribed-geometry model, the fictitious fluid–structure interaction model, and the realistic fluid–structure interaction model [44, 49]. Given the advantages and limitations of these models, the prescribed-geometry model was selected for development. In this thesis, the primary focus is on fluid motion rather than on wall loading and its mechanical response. From this perspective, adding fluid–structure interaction would not provide any additional information relevant to the study. Furthermore, realistic FSI models are relatively complex to personalize, as they require knowledge of ventricular wall contractility, fiber orientation to apply that contractility, and the passive properties of the myocardium.

In contrast, the prescribed-geometry model is based on the extraction of the left ventricular geometry over time, obtained through medical imaging, and thus offers a faithful representation of the geometric variations in the fluid domain for each patient. In this sense, the model follows a fixed implementation framework but allows for a fluid domain geometry that is adaptable to each patient, hence, enabling patient-specific customization.

A second modeling decision was to conduct a 2D simulation, based on findings from the literature. Doost et al. (2017) [58] present an extensive list of 3D and 2D prescribed-geometry models and justify their choice of a 2D model for several reasons. First, the computation time for a 3D model is significantly longer, several days, compared to just a few hours for a 2D model. This represents a major obstacle to applying 3D modeling across a cohort of patients. Second, while the authors acknowledge that 3D simulations provide more realistic information about intraventricular hemodynamics, 2D modeling allows for easier visualization of intraventricular vortex formation and facilitates the extraction of analyzable and interpretable results. Finally, Khalafvand et al. (2015) [18] compared their 2D and 3D simulation results and observed very similar pressure

curves, along with consistent energy transfer characteristics and flow dynamics between the 2D and 3D models.

Lastly, this study opted for a quasi-steady multi-phase modeling of the heart, a choice that is based on the inherent physiological distinction between cardiac wall motion and fluid response timescales. In terms of patient-specific cardiac hemodynamics, the intrachamber fluid field stabilizes on a timescale of a few milliseconds, while the geometric deformation of the atrial and ventricular walls develops on a timescale of several hundred milliseconds. This makes it such that, at every MRI frame, the blood flow is in local dynamic equilibrium long before the next geometric configuration occurs. Given this inherent separation of time scales, each phase of the cardiac cycle can be treated as an independent quasi-steady state with a high level of accuracy. This quasi-steady multi-phase modeling strategy has been widely used in the cardiovascular CFD literature and validated in both experimental and numerical studies [141]. In this context, it is particularly appropriate when the goal is to describe velocity fields, pressure gradients, wall shear stress, and vortex structures at physiologically relevant time points, rather than to fully resolve the entire transient turbulent dynamics. Furthermore, the quasi-steady modeling strategy aligns well with MRI's 25-frames-per-second temporal resolution in which a transient CFD cannot be fully captured with this sampling rate. Attempting to carry out a continuous transient simulation would require making assumptions for intermediate geometries and wall velocities that cannot be directly observed from imaging data, which would introduce an inherent level of modeling uncertainty. Hence, the use of a quasi-steady model in this thesis is not a constraint, but rather a physiologically motivated and methodologically worthwhile approach for allowing us to reconstruct intrachamber flow phenomena in a meaningful way while keeping the expense of computation reasonably low, as well as being consistent with patient-specific (MRI-derived) geometry, and not harming the accurate estimation of local hemodynamic indices such as WSS and vorticity. This approach provides an appropriate trade-off for achieving physiologically realistic flow while balancing constraints associated with the feasibility of computation, which is at the core of this study.

6.2 Limitations of the Study

The research faces its main limitations because of the basic assumptions which were used to build the modeling framework. Chapter 4 explains all the assumptions which were needed to achieve simulation feasibility and maintain computational efficiency. The assumptions used in

cardiovascular modeling studies are standard, but their implementation creates model inaccuracies that reduce the results' physiological accuracy and restrict their use for individual patient conditions.

One important limitation of this study is the use of a fixed mitral valve resistance of 0.5 mmHg·s/mL. This is a standard value often applied in cardiovascular models, and it produces realistic filling dynamics, but it does not reflect the fact that valve resistance can vary from one person to another or under different physiological and pathological conditions. More advanced methods have been developed in the literature [118, 142, 143], such as models that let the valve open and close depending on pressure differences or that include both resistance and inertial effects. These approaches can reproduce valve behavior with greater fidelity but implementing them was beyond the scope of this study.

Another limitation is the assumption that blood behaves as a Newtonian fluid with constant viscosity (0.0035 Pa·s). This value corresponds to standard physiological conditions at 37°C and normal hematocrit and is widely applied in cardiac models of large vessels and chambers. Nevertheless, blood is in fact a non-Newtonian, shear-thinning fluid, and these rheological effects may become important in regions of low shear or abnormal flow conditions. The assumption of Newtonian blood rheology, while common in cardiac CFD, has been shown to introduce errors under certain conditions. Studies report that non-Newtonian effects become more pronounced in low-shear or reversed flow regions [144] and that Newtonian models may underestimate wall shear stress in diseased or stented vessels [145]. On the other hand, Lee and Steinman (2006) [146] showed that in normal vessels geometric uncertainty dominates over rheological choice, supporting the adequacy of Newtonian assumptions in baseline cardiac simulations such as the present work.

Numerous studies have shown that two-dimensional models systematically underestimate flow and stress patterns compared with full 3D approaches. For example, Gonzalez & Schoephoerster (1995) [147] demonstrated that abnormal wall motion and vortical structures are captured more realistically in 3D simulations, while Fontaine et al. (1996) [148] reported 10–20% underestimation of peak stresses in 2D analyses. These findings reinforce the fact that, although computationally efficient, the 2D framework used in this study cannot fully reproduce the three-dimensional complexity of left ventricular flow.

Similarly, elastance values for the left ventricle and left atrium were assumed based on literature ranges. LV elastance was varied between 0.5 mmHg/mL during diastole and 2.0 mmHg/mL during systole, while atrial elastance was kept constant at 0.5 mmHg/mL. These values are consistent with normal systolic function as reported in prior studies, but they do not capture inter-individual variability or pathological alterations. Moreover, by fixing atrial elastance, the contribution of atrial contraction to late ventricular filling is neglected, which has been shown to play a significant role in both healthy and diseased states.

The results presented in this study were derived from a single patient-specific geometry (HV01). While this dataset was sufficient to validate the stability and conservation properties of the coupled CFD–LPM framework, the specific hemodynamic observations, such as the precise location of vortex formation and the magnitude of Wall Shear Stress, are intrinsically linked to the specific anatomical features and physiological parameters of this individual. Consequently, the hemodynamic conclusions drawn here should be interpreted as a demonstration of the solver's capabilities rather than as generalized clinical findings for the healthy or pathological population. Future work will extend this framework to a larger cohort to establish statistical significance and investigate inter-patient variability.

Finally, valve dynamics were simplified by modeling flow as the ratio of pressure difference to resistance, without accounting for inertial and compliance effects. Although this approach is common in lumped models and sufficient for estimating global valve flows, it cannot reproduce the rapid transients and detailed fluid–leaflet interactions that occur in reality.

CHAPTER 7 CONCLUSION

Heart disease is still the leading cause of death around the world, so being able to spot problems in the heart early on is really important. The left side of the heart, including the atrium, ventricle, and mitral valve, does most of the work of pumping blood to the body, and for that reason it is often where functional problems first appear. Catheterization can provide very precise measurements of intracardiac pressures, but it is invasive, carries risk, and is not suitable for frequent use. Non-invasive imaging methods such as echocardiography and cardiac MRI are safer and widely used, but they do not always capture the full complexity of blood flow. In particular, quantities such as wall shear stress and the formation of vortices within the chambers are difficult to assess with these techniques. This gap motivated the present work: to develop a non-invasive, patient-specific approach for studying left heart blood flow that still provides detailed hemodynamic information.

In this work, two approaches were combined: a lumped-parameter elastance model (LPM) and a prescribed-geometry CFD solver. MRI scans from a healthy volunteer were used to obtain the actual shape of the heart chambers, while the elastance model provided realistic changes in chamber volumes over the cardiac cycle. By coupling these components, it was possible to compute blood flow fields, pressure distributions, wall shear stress, and vortex intensity in both the left atrium and left ventricle at rest. The goal was to find a balance: a model simple enough to run efficiently on a standard computer but detailed enough to reveal meaningful hemodynamic patterns. Compared with more complex frameworks that include full fluid–structure interaction, this approach is easier to implement while still capturing the key features of left heart blood flow.

The results showed that the model was able to reproduce the main flow patterns expected in the left heart. The flow fields followed the normal sequence, with ventricular filling driven by atrial inflow, followed by ventricular ejection. Vortex structures formed and dissipated in a way that was consistent with descriptions in the literature. Pressure and velocity values remained within normal physiological ranges, supporting the realism of the simulations. Wall shear stress maps and vorticity fields also varied over time and space in patterns that agreed with experimental data and previous simulations. Validation against 4D MRI data and other published benchmarks showed good agreement, indicating that the model can represent intraventricular flow dynamics in a realistic and reliable way.

Of course, this study also has clear limitations. To keep the model practical, several simplifying assumptions were made, for example, using a constant mitral valve resistance and modeling blood as a Newtonian fluid. These choices helped keep the simulations computationally manageable, but they also reduced the level of physiological detail that could be captured. Additionally, the two-dimensional nature of the work meant that some features associated with three-dimensionality, such as complex vortex structures or stresses acting out of the plane of the heart, were never captured. Nevertheless, the model provided important information about the function of the heart, and the results showed good agreement with both clinical observations and published work.

Looking forward, this work could be advanced in several directions. Full 3D simulations would allow us to investigate vortices, secondary flows, and wall shear stresses with level of detail that was unachievable in this work. Machine learning could also be incorporated into the workflow, not to replace CFD as outlined here, but as another tool to rapidly predict flow patterns or to automate one of the most labor-intense processes, which is you obtain an MRI scan and segmenting the results to use in a simulation. Another important step would be to simulate the heart function during exercise, because many heart conditions will only be detectable during exercise induced stress and unnoticed when the heart is at rest.

In conclusion, this thesis built and tested a patient-specific modeling framework that combines MRI-based heart geometry with an elastance-driven CFD approach to study blood flow in the left heart. The results showed that the model can reproduce realistic flow features, capture important hemodynamic parameters over space and time, and agree well with both experimental data and clinical observations. Even with these simplifications, the work shows that computational modeling can serve as a useful complement to existing diagnostic tools, particularly for the early detection and follow-up of cardiac dysfunction. Progress toward models that are more accurate, efficient, and practical in a clinical setting could help bring these techniques into routine use and ultimately support better diagnosis and management of patients with cardiovascular disease.

This study represents an initial step toward using non-invasive methods to investigate left heart hemodynamics, but several future directions could strengthen the framework and move it closer to clinical application.

A logical next step would be to extend the simulations from two dimensions to three. Unlike a 2D framework, a 3D model can resolve additional flow features such as secondary currents, more

complex intraventricular vortices, and regional variations in wall shear stress that are not visible in a single plane. The main drawback is the much higher computational cost in terms of both time and resources. However, with ongoing advances in high-performance computing and more efficient solvers, this type of simulation is becoming increasingly feasible. Moving to 3D would bring the numerical model closer to the true behavior of blood flow in the human heart.

Another promising direction is the integration of machine learning into this type of modeling. With sufficient patient data, machine learning could be used to rapidly estimate quantities such as blood flow patterns, vortex structures, or wall shear stress directly from imaging, instead of running a full CFD simulation for each case. It could also help accelerate and standardize MRI segmentation, which remains one of the most time-consuming and operator-dependent steps. In this way, machine learning would not replace CFD, but rather complement it, reducing workload and making the overall approach more practical for application to larger patient cohorts.

Extending the framework to simulate exercise conditions would make the results more clinically relevant. Under stress, the heart rate increases, contractions become stronger, and filling patterns change. These adjustments can reveal early dysfunction that may not be apparent at rest. Simulating exercise would therefore provide a more complete picture for diagnosis and help clinicians evaluate treatment options more effectively.

Finally, using this model to test new cardiac treatments could be another valuable application. By simulating blood flow under different medications or therapies, the model could provide additional insight for clinicians while also improving its ability to predict outcomes. For example, incorporating pharmacodynamic effects, such as vasodilation, changes in contractility, or variations in blood viscosity, could allow simulation of patient-specific responses after an intervention. Similarly, the framework could be adapted to assess hemodynamic changes following surgical procedures or device-based therapies (e.g., valve repair, left atrial appendage closure, pacemaker programming). In these scenarios, the model would evolve into a virtual testing environment for individualized treatment planning and decision support, linking computational modeling with clinical cardiology.

Taken together, these developments point toward a more accurate and practical framework that could eventually support patient-specific assessment and clinical decision-making.

REFERENCES

[1] L. Garber, S. Khodaei, and Z. Keshavarz-Motamed, "The critical role of lumped parameter models in patient-specific cardiovascular simulations," *Archives of computational methods in engineering*, vol. 29, no. 5, pp. 2977-3000, 2022.

[2] J. Bermejo, P. Martínez-Legazpi, and J. C. del Alamo, "The Clinical Assessment of Intraventricular Flows," (in English), *Annu Rev Fluid Mech*, vol. 47, pp. 315-342, 2015, doi: 10.1146/annurev-fluid-010814-014728.

[3] A. Kheradvar, C. Rickers, D. Morisawa, M. Kim, G. R. Hong, and G. Pedrizzetti, "Diagnostic and prognostic significance of cardiovascular vortex formation," *J Cardiol*, vol. 74, no. 5, pp. 403-411, Nov 2019, doi: 10.1016/j.jjcc.2019.05.005.

[4] R. L. Winslow, D. F. Scollan, A. Holmes, C. K. Yung, J. Zhang, and M. S. Jafri, "Electrophysiological modeling of cardiac ventricular function: from cell to organ," *Annu Rev Biomed Eng*, vol. 2, pp. 119-55, 2000, doi: 10.1146/annurev.bioeng.2.1.119.

[5] W. Liu and Z. Wang, "Current Understanding of the Biomechanics of Ventricular Tissues in Heart Failure," (in eng), *Bioengineering (Basel)*, vol. 7, no. 1, Dec 20 2019, doi: 10.3390/bioengineering7010002.

[6] T. Røe Å *et al.*, "Increased passive stiffness promotes diastolic dysfunction despite improved Ca2+ handling during left ventricular concentric hypertrophy," (in eng), *Cardiovasc Res*, vol. 113, no. 10, pp. 1161-1172, Aug 1 2017, doi: 10.1093/cvr/cvx087.

[7] J. E. Hall and M. E. Hall, *Guyton and Hall textbook of medical physiology*, 14th edition. ed. Philadelphia, PA: Elsevier, 2021, pp. xix, 1132 pages.

[8] P. P. Bourgouin and R. Madan, "Imaging of the Middle and Visceral Mediastinum," *Radiol Clin North Am*, vol. 59, no. 2, pp. 193-204, Mar 2021, doi: 10.1016/j.rcl.2020.11.004.

[9] J. Gupta. "Biology of the Heart." https://www.msdmanuals.com/home/heart-and-blood-vessel-disorders/biology-of-the-heart-and-blood-vessels/biology-of-the-heart (accessed.

[10] J. R. Mitchell and J. J. Wang, "Expanding application of the Wiggers diagram to teach cardiovascular physiology," *Adv Physiol Educ*, vol. 38, no. 2, pp. 170-5, Jun 2014, doi: 10.1152/advan.00123.2013.

[11] K. A. Y. J. Gordon Betts, James A. Wise, Eddie Johnson, Brandon Poe, Dean H. Kruse, Oksana Korol, Jody E. Johnson, Mark Womble, Peter DeSaix, *Anatomy and Physiology*. OpenStax, 2013.

[12] M. American College of Sports, D. Riebe, J. K. Ehrman, G. Liguori, M. Magal, and M. American College of Sports. (2018). ACSM's guidelines for exercise testing and prescription. Available: https://bibliu.com/users/saml/samlLeeds?RelayState=eyJjdXN0b21fbGF1bmNoX3VybCI6IiMvdmlldy9ib29rcy85NzgxOTc1MTUwMjExL2VwdWIvT0VCUFMvVGV4dC9Db250ZW50Lmh0bWwifQ%3D%3D

[13] A. M. Maceira, S. K. Prasad, M. Khan, and D. J. Pennell, "Normalized left ventricular systolic and diastolic function by steady state free precession cardiovascular magnetic

resonance," *J Cardiovasc Magn Reson,* vol. 8, no. 3, pp. 417-26, 2006, doi: 10.1080/10976640600572889.

[14] "Ejection Fraction Heart Failure Measurement." https://www.heart.org/en/health-topics/heart-failure/diagnosing-heart-failure/ejection-fraction-heart-failure-measurement?utm_source=chatgpt.com (accessed.

[15] A. d. l. s. p. d. Canada. "Hypertension." https://www.canada.ca/fr/sante-publique/services/maladies/sante-coeur/tension-arterielle-elevee.html (accessed.

[16] J. M. Norton, "Toward consistent definitions for preload and afterload," *Adv Physiol Educ,* vol. 25, no. 1-4, pp. 53-61, Dec 2001, doi: 10.1152/advances.2001.25.1.53.

[17] P. J. Kilner, G. Z. Yang, A. J. Wilkes, R. H. Mohiaddin, D. N. Firmin, and M. H. Yacoub, "Asymmetric redirection of flow through the heart," *Nature,* vol. 404, no. 6779, pp. 759-61, Apr 13 2000, doi: 10.1038/35008075.

[18] S. S. Khalafvand, T. K. Hung, E. Y. Ng, and L. Zhong, "Kinematic, Dynamic, and Energy Characteristics of Diastolic Flow in the Left Ventricle," *Comput Math Methods Med,* vol. 2015, p. 701945, 2015, doi: 10.1155/2015/701945.

[19] T.-K. HUNG, S. S. KHALAFVAND, and E. Y.-K. NG, "FLUID DYNAMIC CHARACTERISTICS OF SYSTOLIC BLOOD FLOW OF THE LEFT VENTRICLE," *Journal of Mechanics in Medicine and Biology,* vol. 15, no. 03, p. 1550047, 2015, doi: 10.1142/s0219519415500475.

[20] K. Courchaine and S. Rugonyi, "Quantifying blood flow dynamics during cardiac development: demystifying computational methods," *Philos Trans R Soc Lond B Biol Sci,* vol. 373, no. 1759, Sep 24 2018, doi: 10.1098/rstb.2017.0330.

[21] M. Midgett, K. Thornburg, and S. Rugonyi, "Blood flow patterns underlie developmental heart defects," *Am J Physiol Heart Circ Physiol,* vol. 312, no. 3, pp. H632-H642, Mar 1 2017, doi: 10.1152/ajpheart.00641.2016.

[22] P. M. Arvidsson *et al.*, "Left and right ventricular hemodynamic forces in healthy volunteers and elite athletes assessed with 4D flow magnetic resonance imaging," *Am J Physiol Heart Circ Physiol,* vol. 312, no. 2, pp. H314-H328, Feb 1 2017, doi: 10.1152/ajpheart.00583.2016.

[23] J. Eriksson, J. Zajac, U. Alehagen, A. F. Bolger, T. Ebbers, and C. J. Carlhall, "Left ventricular hemodynamic forces as a marker of mechanical dyssynchrony in heart failure patients with left bundle branch block," *Sci Rep,* vol. 7, no. 1, p. 2971, Jun 7 2017, doi: 10.1038/s41598-017-03089-x.

[24] S. S. Khalafvand, L. Zhong, and E. Y. Ng, "Three-dimensional CFD/MRI modeling reveals that ventricular surgical restoration improves ventricular function by modifying intraventricular blood flow," *Int J Numer Method Biomed Eng,* vol. 30, no. 10, pp. 1044-56, Oct 2014, doi: 10.1002/cnm.2643.

[25] T. Lapinskas *et al.*, "The Intraventricular Hemodynamic Forces Estimated Using Routine CMR Cine Images: A New Marker of the Failing Heart," *JACC Cardiovasc Imaging,* vol. 12, no. 2, pp. 377-379, Feb 2019, doi: 10.1016/j.jcmg.2018.08.012.

[26] G. Pedrizzetti, A. R. Martiniello, V. Bianchi, A. D'Onofrio, P. Caso, and G. Tonti, "Cardiac fluid dynamics anticipates heart adaptation," *J Biomech,* vol. 48, no. 2, pp. 388-91, Jan 21 2015, doi: 10.1016/j.jbiomech.2014.11.049.

[27] Y. Tayyabah, D. George, and P. Marios, "Chapter Two - Advances in MRI Methodology," in *Imaging in Movement Disorders: Imaging Methodology and Applications in Parkinson's Disease*, vol. 141, P. Marios Ed., no. International Review of Neurobiology): Academic Press, 2018, pp. 31-76.

[28] S. Majumdar and H. K. Genant, "A review of the recent advances in magnetic resonance imaging in the assessment of osteoporosis," *Osteoporos Int,* vol. 5, no. 2, pp. 79-92, Mar 1995, doi: 10.1007/BF01623308.

[29] L. Huang *et al.*, "Using multi-parametric quantitative MRI to screen for cardiac involvement in patients with idiopathic inflammatory myopathy," *Sci Rep*, vol. 12, no. 1, p. 9819, Jun 14 2022, doi: 10.1038/s41598-022-13858-y.

[30] K. K. Wong, R. M. Kelso, S. G. Worthley, P. Sanders, J. Mazumdar, and D. Abbott, "Noninvasive cardiac flow assessment using high speed magnetic resonance fluid motion tracking," *PLoS One*, vol. 4, no. 5, p. e5688, May 25 2009, doi: 10.1371/journal.pone.0005688.

[31] V. Russo, L. Lovato, and G. Ligabue, "Cardiac MRI: technical basis," *La radiologia medica,* vol. 125, no. 11, pp. 1040-1055, 2020/11/01 2020, doi: 10.1007/s11547-020-01282-z.

[32] B. Lucas and T. Kanade, "An Iterative Image Registration Technique with an Application to Stereo Vision (IJCAI)," presented at the [No source information available], 04, 1981.

[33] K. K. Wong, Z. Sun, and J. Tu, "Medical imaging and computer-aided flow analysis of a heart with atrial septal defect," *Journal of Mechanics in Medicine and Biology,* vol. 12, no. 05, p. 1250024, 2012.

[34] J. Rizk, "4D flow MRI applications in congenital heart disease," *Eur Radiol,* vol. 31, no. 2, pp. 1160-1174, Feb 2021, doi: 10.1007/s00330-020-07210-z.

[35] K. Jacobs, L. Hahn, M. Horowitz, S. Kligerman, S. Vasanawala, and A. Hsiao, "Hemodynamic Assessment of Structural Heart Disease Using 4D Flow MRI: How We Do It," *AJR Am J Roentgenol*, vol. 217, no. 6, pp. 1322-1332, Dec 2021, doi: 10.2214/AJR.21.25978.

[36] M. H. Moosavi, N. Fatouraee, H. Katoozian, A. Pashaei, O. Camara, and A. F. Frangi, "Numerical simulation of blood flow in the left ventricle and aortic sinus using magnetic resonance imaging and computational fluid dynamics," (in English), *Comput Method Biomec,* vol. 17, no. 7, pp. 740-749, May 19 2014, doi: 10.1080/10255842.2012.715638.

[37] B. T. Chan, E. Lim, K. H. Chee, and N. A. Abu Osman, "Review on CFD simulation in heart with dilated cardiomyopathy and myocardial infarction," (in English), *Comput Biol Med,* vol. 43, no. 4, pp. 377-385, May 1 2013, doi: 10.1016/j.compbiomed.2013.01.013.

[38] M. Markl, A. Frydrychowicz, S. Kozerke, M. Hope, and O. Wieben, "4D flow MRI," (in English), *J Magn Reson Imaging,* vol. 36, no. 5, pp. 1015-1036, Nov 2012, doi: 10.1002/jmri.23632.

[39] F. M. Callaghan, J. Karkouri, K. Broadhouse, M. Evin, D. F. Fletcher, and S. M. Grieve, "Thoracic aortic aneurysm: 4D flow MRI and computational fluid dynamics model," (in English), *Comput Method Biomec,* vol. 18, pp. 1894-1895, Oct 9 2015, doi: Doi 10.1080/10255842.2015.1069559.

[40] J. O. Mangual *et al.,* "Comparative numerical study on left ventricular fluid dynamics after dilated cardiomyopathy," (in English), *J Biomech,* vol. 46, no. 10, pp. 1611-1617, Jun 21 2013, doi: 10.1016/j.jbiomech.2013.04.012.

[41] P. Soni, S. Kumar, B. V. R. Kumar, S. K. Rai, A. Verma, and O. Shankar, "A comprehensive review on CFD simulations of left ventricle hemodynamics: numerical methods, experimental validation techniques, and emerging trends," (in English), *J Braz Soc Mech Sci,* vol. 46, no. 5, May 2024, doi: ARTN 301

10.1007/s40430-024-04875-1.

[42] Q. Long, R. Merrifield, X. Y. Xu, P. Kilner, D. N. Firmin, and G. Z. Yang, "Subject-specific computational simulation of left ventricular flow based on magnetic resonance imaging," (in English), *P I Mech Eng H,* vol. 222, no. H4, pp. 475-485, May 2008, doi: 10.1243/09544119jeim310.

[43] B. J. Bellhouse, "Fluid Mechanics of a Model Mitral-Valve and Left Ventricle," (in English), *Cardiovasc Res,* vol. 6, no. 2, pp. 199-+, 1972, doi: DOI 10.1093/cvr/6.2.199.

[44] S. N. Doost, D. Ghista, B. Y. Su, L. Zhong, and Y. S. Morsi, "Heart blood flow simulation: a perspective review," (in English), *Biomed Eng Online,* vol. 15, Aug 25 2016, doi: ARTN 101

10.1186/s12938-016-0224-8.

[45] D. Lopes, H. Puga, J. Teixeira, and R. Lima, "Blood flow simulations in patient-specific geometries of the carotid artery: A systematic review," (in English), *J Biomech,* vol. 111, Oct 9 2020, doi: ARTN 110019

10.1016/j.jbiomech.2020.110019.

[46] H. Azhari, M. Buchalter, S. Sideman, E. Shapiro, and R. Beyar, "A conical model to describe the nonuniformity of the left ventricular twisting motion," *Ann Biomed Eng,* vol. 20, no. 2, pp. 149-65, 1992, doi: 10.1007/BF02368517.

[47] J. A. Vierendeels, K. Riemslagh, E. Dick, and P. R. Verdonck, "Computer simulation of intraventricular flow and pressure gradients during diastole," *J Biomech Eng,* vol. 122, no. 6, pp. 667-74, Dec 2000, doi: 10.1115/1.1318941.

[48] B. Baccani, F. Domenichini, G. Pedrizzetti, and G. Tonti, "Fluid dynamics of the left ventricular filling in dilated cardiomyopathy," *J Biomech,* vol. 35, no. 5, pp. 665-71, May 2002, doi: 10.1016/s0021-9290(02)00005-2.

[49] S. S. Khalafvand, E. Y. K. Ng, and L. Zhong, "CFD simulation of flow through heart: a perspective review," (in English), *Comput Method Biomec,* vol. 14, no. 1, pp. 113-132, 2011, doi: 10.1080/10255842.2010.493515.

[50] Q. Long, R. Merrifield, X. Y. Xu, P. Kilner, D. N. Firmin, and Y. G-Z, "Subject-specific computational simulation of left ventricular flow based on magnetic resonance imaging,"

Proc Inst Mech Eng H, vol. 222, no. 4, pp. 475-85, May 2008, doi: 10.1243/09544119JEIM310.

[51] N. R. Saber, A. D. Gosman, N. B. Wood, P. J. Kilner, C. L. Charrier, and D. N. Firmin, "Computational flow modeling of the left ventricle based on in vivo MRI data: initial experience," *Ann Biomed Eng,* vol. 29, no. 4, pp. 275-83, Apr 2001, doi: 10.1114/1.1359452.

[52] T. Schenkel, M. Malve, M. Reik, M. Markl, B. Jung, and H. Oertel, "MRI-based CFD analysis of flow in a human left ventricle: methodology and application to a healthy heart," *Ann Biomed Eng,* vol. 37, no. 3, pp. 503-15, Mar 2009, doi: 10.1007/s10439-008-9627-4.

[53] R. Hvid, M. B. Stuart, J. A. Jensen, and M. S. Traberg, "Intra-Cardiac Flow from Geometry Prescribed Computational Fluid Dynamics: Comparison with Ultrasound Vector Flow Imaging," (in English), *Cardiovasc Eng Techn,* Jun 15 2023, doi: 10.1007/s13239-023-00666-2.

[54] M. Rajat *et al.*, "Computational modeling of cardiac hemodynamics: Current status and future outlook," *Journal of Computational Physics,* vol. 305, pp. 1065-1082, 2016, doi: https://doi.org/10.1016/j.jcp.2015.11.022.

[55] S. Krittian, U. Janoske, H. Oertel, and T. Böhlke, "Partitioned Fluid-Solid Coupling for Cardiovascular Blood Flow," (in English), *Ann Biomed Eng,* vol. 38, no. 4, pp. 1426-1441, Apr 2010, doi: 10.1007/s10439-009-9895-7.

[56] T. B. Le and F. Sotiropoulos, "On the three-dimensional vortical structure of early diastolic flow in a patient-specific left ventricle," (in English), *Eur J Mech B-Fluid,* vol. 35, pp. 20-24, Sep-Oct 2012, doi: 10.1016/j.euromechflu.2012.01.013.

[57] D. Lopes *et al.*, "Analysis of finite element and finite volume methods for fluid-structure interaction simulation of blood flow in a real stenosed artery," (in English), *Int J Mech Sci,* vol. 207, Oct 1 2021, doi: ARTN 106650

10.1016/j.ijmecsci.2021.106650.

[58] S. N. Doost, L. Zhong, B. Su, and Y. S. Morsi, "Two-dimensional intraventricular flow pattern visualization using the image-based computational fluid dynamics," *Comput Methods Biomech Biomed Engin,* vol. 20, no. 5, pp. 492-507, Apr 2017, doi: 10.1080/10255842.2016.1250891.

[59] A. M. Bavo *et al.*, "Patient-specific CFD models for intraventricular flow analysis from 3D ultrasound imaging: Comparison of three clinical cases," (in English), *J Biomech,* vol. 50, pp. 144-150, Jan 4 2017, doi: DOI 10.1016/j.jbiomech.2016.11.039.

[60] Y. Alharbi *et al.*, "Fluid structure computational model of simulating mitral valve motion in a contracting left ventricle," (in English), *Comput Biol Med,* vol. 148, Sep 2022, doi: ARTN 105834

10.1016/j.compbiomed.2022.105834.

[61] L. Christierson *et al.*, "Validation of fluid-structure interaction simulations of the opening phase of phantom mitral heart valves under physiologically inspired conditions," *Comput Biol Med,* vol. 171, p. 108033, Mar 2024, doi: 10.1016/j.compbiomed.2024.108033.

[62] V. Bryon, S. V. Wifstad, T. Gronli, J. Hu, and L. Lovstakken, "Automated Patient-Specific Left Ventricular Simulations for Cardiac Function Evaluation Using Image-Based Computational Fluid Dynamics and Color Flow Imaging," in *2023 IEEE International Ultrasonics Symposium (IUS), 2023*, Piscataway, NJ, USA, 2023: IEEE, in 2023 IEEE International Ultrasonics Symposium (IUS), pp. 1-4, doi: 10.1109/IUS51837.2023.10307878. [Online]. Available: http://dx.doi.org/10.1109/IUS51837.2023.10307878

[63] S. A. Esfahani, K. Hassani, and D. M. Espino, "Fluid-structure interaction assessment of blood flow hemodynamics and leaflet stress during mitral regurgitation," (in English), *Comput Method Biomec,* vol. 22, no. 3, pp. 288-303, Feb 17 2019, doi: 10.1080/10255842.2018.1552683.

[64] Y. H. Loke, F. Capuano, E. Balaras, and L. J. Olivieri, "Computational Modeling of Right Ventricular Motion and Intracardiac Flow in Repaired Tetralogy of Fallot," (in English), *Cardiovasc Eng Techn,* vol. 13, no. 1, pp. 41-54, Feb 2022, doi: 10.1007/s13239-021-00558-3.

[65] V. Kannojiya, A. K. Das, and P. K. Das, "Effect of left ventricular assist device on the hemodynamics of a patient-specific left heart," (in English), *Med Biol Eng Comput,* vol. 60, no. 6, pp. 1705-1721, Jun 2022, doi: 10.1007/s11517-022-02572-6.

[66] X. W. Zuo *et al.*, "Co-simulation of hypertensive left ventricle based on computational fluid dynamics and a closed-loop network model," (in English), *Comput Meth Prog Bio,* vol. 216, Apr 2022, doi: ARTN 106649

10.1016/j.cmpb.2022.106649.

[67] P. R. Leinan *et al.*, "Comparison of ultrasound vector flow imaging and CFD simulations with PIV measurements of flow in a left ventricular outflow trackt phantom- Implications for clinical use and in silico studies," (in English), *Comput Biol Med,* vol. 146, Jul 2022, doi: ARTN 105358

10.1016/j.compbiomed.2022.105358.

[68] A. Zingaro *et al.*, "A Geometric Multiscale Model for the Numerical Simulation of Blood Flow in the Human Left Heart," (in English), *Discrete Cont Dyn-S,* vol. 15, no. 8, pp. 2391-2427, Aug 2022, doi: 10.3934/dcdss.2022052.

[69] F. Xu and S. Kenjeres, "Numerical simulations of flow patterns in the human left ventricle model with a novel dynamic mesh morphing approach based on radial basis function," (in English), *Comput Biol Med,* vol. 130, Mar 2021, doi: ARTN 104184

10.1016/j.compbiomed.2020.104184.

[70] P. R. Chen *et al.*, "Blood flow patterns estimation in the left ventricle with low-rate 2D and 3D dynamic contrast-enhanced ultrasound," (in English), *Comput Meth Prog Bio,* vol. 198, Jan 2021, doi: ARTN 105810

10.1016/j.cmpb.2020.105810.

[71] J. Lantz *et al.*, "Impact of prosthetic mitral valve orientation on the ventricular flow field: Comparison using patient-specific computational fluid dynamics," (in English), *J Biomech,* vol. 116, Feb 12 2021, doi: 10.1016/j.jbiomech.2020.110209.

[72] K. Itatani *et al.*, "New imaging tools in cardiovascular medicine: computational fluid dynamics and 4D flow MRI," (in English), *Gen Thorac Cardiovas,* vol. 65, no. 11, pp. 611-621, Nov 2017, doi: 10.1007/s11748-017-0834-5.

[73] S. K. Dahl, J. Vierendeels, J. Degroote, S. Annerel, L. R. Hellevik, and B. Skallerud, "FSI simulation of asymmetric mitral valve dynamics during diastolic filling," (in English), *Comput Method Biomec,* vol. 15, no. 2, pp. 121-130, 2012, doi: 10.1080/10255842.2010.517200.

[74] L. Bennati *et al.*, "Turbulent blood dynamics in the left heart in the presence of mitral regurgitation: a computational study based on multi-series cine-MRI," (in English), *Biomech Model Mechan,* vol. 22, no. 6, pp. 1829-1846, Dec 2023, doi: 10.1007/s10237-023-01735-0.

[75] L. Bennati *et al.*, "An Image-Based Computational Fluid Dynamics Study of Mitral Regurgitation in Presence of Prolapse," (in English), *Cardiovasc Eng Techn,* vol. 14, no. 3, pp. 457-475, Jun 2023, doi: 10.1007/s13239-023-00665-3.

[76] L. Y. Feng, H. Gao, N. Qi, M. Danton, N. A. Hill, and X. Y. Luo, "Fluid-structure interaction in a fully coupled three-dimensional mitral-atrium-pulmonary model," (in English), *Biomech Model Mechan,* vol. 20, no. 4, pp. 1267-1295, Aug 2021, doi: 10.1007/s10237-021-01444-6.

[77] I. Fumagalli *et al.*, "An image-based computational hemodynamics study of the Systolic Anterior Motion of the mitral valve," *Comput Biol Med,* vol. 123, p. 103922, Aug 2020, doi: 10.1016/j.compbiomed.2020.103922.

[78] S. Miyauchi, T. Yamada, K. Hosoi, T. Hayase, and K. Funamoto, "Numerical analysis of the blood flow in the left ventricle with internal structures: Effect of trabeculae carneae models and atrial fibrillation," *AIP Advances,* vol. 9, no. 10, 2019, doi: 10.1063/1.5124730.

[79] F. Sacco *et al.*, "Left ventricular trabeculations decrease the wall shear stress and increase the intra-ventricular pressure drop in CFD simulations," *Frontiers in Physiology,* vol. 9, p. 458, 2018.

[80] T. Yamada, T. Hayase, S. Miyauchi, and K. Funamoto, "Numerical analysis of the effect of trabeculae carneae models on blood flow in a left ventricle model constructed from magnetic resonance images," *Journal of Biomechanical Science and Engineering,* vol. 13, no. 2, pp. 17-00597-17-00597, 2018.

[81] H. Gao, L. Feng, N. Qi, C. Berry, B. E. Griffith, and X. Luo, "A coupled mitral valve—left ventricle model with fluid–structure interaction," *Medical engineering & physics,* vol. 47, pp. 128-136, 2017.

[82] A. Imanparast, N. Fatouraee, and F. Sharif, "Comprehensive computational assessment of blood flow characteristics of left ventricle based on in-vivo MRI in presence of artificial myocardial infarction," *Mathematical Biosciences,* vol. 294, pp. 143-159, 2017.

[83] A. Imanparast, N. Fatouraee, and F. Sharif, "The impact of valve simplifications on left ventricular hemodynamics in a three dimensional simulation based on in vivo MRI data," *J Biomech,* vol. 49, no. 9, pp. 1482-1489, 2016.

[84] S. N. Doost, L. Zhong, B. Su, and Y. S. Morsi, "The numerical analysis of non-Newtonian blood flow in human patient-specific left ventricle," *Comput Meth Prog Bio,* vol. 127, pp. 232-247, 2016.

[85] S. Boyang *et al.*, "Cardiac MRI based numerical modeling of left ventricular fluid dynamics with mitral valve incorporated," *J Biomech,* vol. 49, no. 7, pp. 1199-1205, 2016, doi: https://doi.org/10.1016/j.jbiomech.2016.03.008.

[86] T. Otani, A. Al-Issa, A. Pourmorteza, E. R. McVeigh, S. Wada, and H. Ashikaga, "A Computational Framework for Personalized Blood Flow Analysis in the Human Left Atrium," *Ann Biomed Eng,* vol. 44, no. 11, pp. 3284-3294, Nov 2016, doi: 10.1007/s10439-016-1590-x.

[87] L. Alinezhad, F. Ghalichi, M. Ahmadlouydarab, and M. Chenaghlou, "Left atrial appendage shape impacts on the left atrial flow hemodynamics: A numerical hypothesis generating study on two cases," *Comput Methods Programs Biomed,* vol. 213, p. 106506, Jan 2022, doi: 10.1016/j.cmpb.2021.106506.

[88] D. Federico and P. Gianni, "Intraventricular vortex flow changes in the infarcted left ventricle: numerical results in an idealised 3D shape," *Comput Method Biomec,* vol. 14, no. 1, pp. 95--101, 2011, doi: 10.1080/10255842.2010.485987 , note = PMID: 21271416.

[89] C. Chnafa, S. Mendez, and F. Nicoud, "Image-based simulations show important flow fluctuations in a normal left ventricle: What could be the implications? accepted for publication in Ann. of Biomed," ed: Eng, 2016.

[90] B. Su, X. Wang, F. Kabinejadian, C. Chin, T. T. Le, and J. M. Zhang, "Effects of left atrium on intraventricular flow in numerical simulations," *Comput Biol Med,* vol. 106, pp. 46-53, Mar 2019, doi: 10.1016/j.compbiomed.2019.01.011.

[91] A. Zingaro *et al.*, "A geometric multiscale model for the numerical simulation of blood flow in the human left heart," *arXiv preprint arXiv:2110.02114,* 2021.

[92] S. K. Dahl, "Numerical simulations of blood flow in the left side of the heart," 2012.

[93] R. Koizumi *et al.*, "Numerical analysis of hemodynamic changes in the left atrium due to atrial fibrillation," *J Biomech,* vol. 48, no. 3, pp. 472-8, Feb 5 2015, doi: 10.1016/j.jbiomech.2014.12.025.

[94] S. M. M. Ali, M. F. N. Nashron, W. N. W. Ab Naim, and M. J. M. Mokhtarudin, "Haemodynamics in Left Ventricular Remodelling using Cardiovascular Lumped-Parameter Model," *Sciences (IEICES),* vol. 10, pp. 767-772, 2024.

[95] S. S. Simakov, "Lumped parameter heart model with valve dynamics," *Russian Journal of Numerical Analysis and Mathematical Modelling,* vol. 34, no. 5, pp. 289-300, 2019.

[96] A. Di Molfetta *et al.*, "Tailoring the hybrid palliation for hypoplastic left heart syndrome: A simulation study using a lumped parameter model," *Medical Engineering & Physics,* vol. 37, no. 9, pp. 898-904, 2015.

[97] S. Shimizu *et al.*, "Lumped parameter model for hemodynamic simulation of congenital heart diseases," *The journal of physiological sciences,* vol. 68, no. 2, pp. 103-111, 2018.

[98] Y. Vassilevski, M. Olshanskii, S. Simakov, A. Kolobov, and A. Danilov, *Personalized Computational Hemodynamics: Models, Methods, and Applications for Vascular Surgery and Antitumor Therapy*. Academic Press, 2020.

[99] J. K. Li, *The arterial circulation: physical principles and clinical applications*. Springer Science & Business Media, 2000.

[100] S. Zhou *et al.*, "A review on low-dimensional physics-based models of systemic arteries: application to estimation of central aortic pressure," *Biomed Eng Online*, vol. 18, no. 1, p. 41, 2019.

[101] N. Westerhof, F. Bosman, C. J. De Vries, and A. Noordergraaf, "Analog studies of the human systemic arterial tree," *J Biomech*, vol. 2, no. 2, pp. 121-143, 1969.

[102] N. Stergiopulos, B. E. Westerhof, and N. Westerhof, "Total arterial inertance as the fourth element of the windkessel model," *American Journal of Physiology-Heart and Circulatory Physiology*, vol. 276, no. 1, pp. H81-H88, 1999.

[103] B. Deswysen, A. Charlier, and M. Gevers, "Quantitative evaluation of the systemic arterial bed by parameter estimation of a simple model," *Medical and Biological Engineering and Computing*, vol. 18, no. 2, pp. 153-166, 1980.

[104] W. C. Rose and A. A. Shoukas, "Two-port analysis of systemic venous and arterial impedances," *American Journal of Physiology-Heart and Circulatory Physiology*, vol. 265, no. 5, pp. H1577-H1587, 1993.

[105] H. F. Frasch, J. Y. Kresh, and A. Noordergraaf, "Two-port analysis of microcirculation: an extension of windkessel," *American Journal of Physiology-Heart and Circulatory Physiology*, vol. 270, no. 1, pp. H376-H385, 1996.

[106] A. Di Molfetta *et al.*, "Application of a lumped parameter model to study the feasibility of simultaneous implantation of a continuous flow ventricular assist device (VAD) and a pulsatile flow VAD in BIVAD patients," *Artificial organs*, vol. 41, no. 3, pp. 242-252, 2017.

[107] E.-j. Kim and M. Capoccia, "Synergistic model of cardiac function with a heart assist device," *Bioengineering*, vol. 7, no. 1, p. 1, 2019.

[108] E. Benevento, A. Djebbari, Z. Keshavarz-Motamed, R. Cecere, and L. Kadem, "Hemodynamic changes following aortic valve bypass: a mathematical approach," *PloS one*, vol. 10, no. 4, p. e0123000, 2015.

[109] S. M. Shavik, C. Tossas-Betancourt, C. A. Figueroa, S. Baek, and L. C. Lee, "Multiscale modeling framework of ventricular-arterial bi-directional interactions in the cardiopulmonary circulation," *Frontiers in physiology*, vol. 11, p. 2, 2020.

[110] J. T. Ottesen, M. S. Olufsen, and J. K. Larsen, *Applied mathematical models in human physiology*. SIAM, 2004.

[111] A. Marone *et al.*, "Modeling of the hemodynamics in the feet of patients with peripheral artery disease," *Biomedical Optics Express*, vol. 10, no. 2, pp. 657-669, 2019.

[112] B. Li, W. Wang, B. Mao, and Y. Liu, "A method to personalize the lumped parameter model of coronary artery," *International Journal of Computational Methods*, vol. 16, no. 03, p. 1842004, 2019.

[113] E. Ben-Assa *et al.*, "Ventricular stroke work and vascular impedance refine the characterization of patients with aortic stenosis," *Science translational medicine,* vol. 11, no. 509, p. eaaw0181, 2019.

[114] Y. Shi, P. Lawford, and R. Hose, "Review of zero-D and 1-D models of blood flow in the cardiovascular system," *Biomed Eng Online,* vol. 10, no. 1, p. 33, 2011.

[115] E. Jung and W. Lee, "Lumped parameter models of cardiovascular circulation in normal and arrhythmia cases," *Journal of the Korean Mathematical Society,* vol. 43, no. 4, pp. 885-897, 2006.

[116] J. W. Holmes and J. Lumens, "Clinical applications of patient-specific models: The case for a simple approach," *Journal of cardiovascular translational research,* vol. 11, no. 2, pp. 71-79, 2018.

[117] Z. Keshavarz-Motamed *et al.*, "Mixed valvular disease following transcatheter aortic valve replacement: quantification and systematic differentiation using clinical measurements and image-based patient-specific in silico modeling," *Journal of the American Heart Association,* vol. 9, no. 5, p. e015063, 2020.

[118] J. Mynard, M. Davidson, D. Penny, and J. Smolich, "A simple, versatile valve model for use in lumped parameter and one-dimensional cardiovascular models," *International journal for numerical methods in biomedical engineering,* vol. 28, no. 6-7, pp. 626-641, 2012.

[119] H. Suga, K. Sagawa, and A. A. Shoukas, "Load independence of the instantaneous pressure-volume ratio of the canine left ventricle and effects of epinephrine and heart rate on the ratio," *Circulation research,* vol. 32, no. 3, pp. 314-322, 1973.

[120] P. Segers, N. Stergiopulos, N. Westerhof, P. Wouters, P. Kolh, and P. Verdonck, "Systemic and pulmonary hemodynamics assessed with a lumped-parameter heart-arterial interaction model," *Journal of engineering mathematics,* vol. 47, no. 3, pp. 185-199, 2003.

[121] X. Xie, M. Zheng, D. Wen, Y. Li, and S. Xie, "A new CFD based non-invasive method for functional diagnosis of coronary stenosis," *Biomed Eng Online,* vol. 17, no. 1, p. 36, 2018.

[122] S. Zhou *et al.*, "A review on low-dimensional physics-based models of systemic arteries: application to estimation of central aortic pressure," *Biomed Eng Online,* vol. 18, no. 1, p. 41, Apr 2 2019, doi: 10.1186/s12938-019-0660-3.

[123] T. Korakianitis and Y. Shi, "Numerical simulation of cardiovascular dynamics with healthy and diseased heart valves," *J Biomech,* vol. 39, no. 11, pp. 1964-1982, 2006.

[124] M. Aissiou, D. Périé, F. Cheriet, N. S. Dahdah, C. Laverdière, and D. Curnier, "Imaging of early modification in cardiomyopathy: the doxorubicin-induced model," *The international journal of cardiovascular imaging,* vol. 29, no. 7, pp. 1459-1476, 2013.

[125] E. Heiberg, J. Sjögren, M. Ugander, M. Carlsson, H. Engblom, and H. Arheden, "Design and validation of Segment - freely available software for cardiovascular image analysis," *BMC Medical Imaging,* vol. 10, no. 1, p. 1, 2010/01/11 2010, doi: 10.1186/1471-2342-10-1.

[126] A. Fyrenius, L. Wigström, T. Ebbers, M. Karlsson, J. Engvall, and A. F. Bolger, "Three dimensional flow in the human left atrium," *Heart,* vol. 86, no. 4, pp. 448-455, 2001.

[127] K. P. Owashi, A. Hubert, E. Galli, E. Donal, A. I. Hernández, and V. Le Rolle, "Model-based estimation of left ventricular pressure and myocardial work in aortic stenosis," *PLoS One,* vol. 15, no. 3, p. e0229609, 2020.

[128] N. Westerhof, J.-W. Lankhaar, and B. E. Westerhof, "The arterial windkessel," *Med Biol Eng Comput,* vol. 47, no. 2, pp. 131-141, 2009.

[129] W. L. Maughan, A. A. Shoukas, K. Sagawa, and M. L. Weisfeldt, "Instantaneous pressure-volume relationship of the canine right ventricle," *Circulation research,* vol. 44, no. 3, pp. 309-315, 1979.

[130] F. Sotiropoulos, T. B. Le, and A. Gilmanov, "Fluid mechanics of heart valves and their replacements," *Annual Review of Fluid Mechanics,* vol. 48, no. 1, pp. 259-283, 2016.

[131] S. Armfield and R. Street, "An analysis and comparison of the time accuracy of fractional-step methods for the Navier–Stokes equations on staggered grids," *International Journal for Numerical Methods in Fluids,* vol. 38, no. 3, pp. 255-282, 2002.

[132] V. Ahanathapillai, J. J. Soraghan, and P. Sonecki, "Delaunay triangulation based image enhancement for echocardiography images," in *2009 17th European Signal Processing Conference*, 2009: IEEE, pp. 1878-1882.

[133] C. Loudon and A. Tordesillas, "The use of the dimensionless Womersley number to characterize the unsteady nature of internal flow," *Journal of theoretical biology,* vol. 191, no. 1, pp. 63-78, 1998.

[134] E. Aune, M. Bækkevar, O. Rødevand, and J. E. Otterstad, "Reference values for left ventricular volumes with real-time 3-dimensional echocardiography," *Scandinavian Cardiovascular Journal,* vol. 44, no. 1, pp. 24-30, 2010.

[135] E. Aune, M. Baekkevar, J. Roislien, O. Rodevand, and J. E. Otterstad, "Normal reference ranges for left and right atrial volume indexes and ejection fractions obtained with real-time three-dimensional echocardiography," *European Journal of Echocardiography,* vol. 10, no. 6, pp. 738-744, 2009.

[136] D. Périé-Curnier, A. Bedoux, P. Dubois, and S. Leclaire, "MRI-based analysis of the blood flow in the left ventricle: 2D geometry-prescribed Cine-MRI based model versus 4D-Flow CMR," presented at the ISMRM & ISMRT annual Meeting & Exhibition, Singapore, 2024. [Online]. Available: https://doi.org/10.58530/2024/0099.

[137] M. M. Bissell *et al.,* "4D Flow cardiovascular magnetic resonance consensus statement: 2023 update," *Journal of Cardiovascular Magnetic Resonance,* vol. 25, no. 1, p. 40, 2023.

[138] V. Govindarajan *et al.,* "Synergy between diastolic mitral valve function and left ventricular flow aids in valve closure and blood transport during systole," *Scientific reports,* vol. 8, no. 1, p. 6187, 2018.

[139] A. Caballero, W. Mao, R. McKay, C. Primiano, S. Hashim, and W. Sun, "New insights into mitral heart valve prolapse after chordae rupture through fluid–structure interaction computational modeling," *Scientific reports,* vol. 8, no. 1, p. 17306, 2018.

[140] L. Obermeier *et al.,* "CT-based simulation of left ventricular hemodynamics: a pilot study in mitral regurgitation and left ventricle aneurysm patients," *Frontiers in Cardiovascular Medicine,* vol. 9, p. 828556, 2022.

[141] H.-H. Vu and C.-H. Hsu, "Quasi-Steady Flow Dynamics Study of Human Aortic Valve with Numerical Techniques," *Journal of Mechanics*, vol. 28, no. 4, pp. 637-646, 2012.

[142] K. Hemalatha, M. Manivannan, and S. Thanikachalam, "Numerical simulation of cardiac valve flow velocity patterns in normal and abnormal conditions," in *2010 international conference on communication control and computing technologies*, 2010: IEEE, pp. 536-539.

[143] J. Wolfe, G. Szabo, T. Radovits, and L. Waite, "Using a mathematical model for diastolic filling through the mitral valve to determine cardiac properties," *Biomedical Sciences Instrumentation*, vol. 48, pp. 493-500, 2012.

[144] H. Wei, A. L. Cheng, and N. M. Pahlevan, "On the significance of blood flow shear-rate-dependency in modeling of Fontan hemodynamics," *European Journal of Mechanics-B/Fluids*, vol. 84, pp. 1-14, 2020.

[145] J. Mejia, R. Mongrain, and O. F. Bertrand, "Accurate prediction of wall shear stress in a stented artery: Newtonian versus non-Newtonian models," 2011.

[146] S.-W. Lee and D. A. Steinman, "On the relative importance of rheology for image-based CFD models of the carotid bifurcation," *J Biomech*, vol. 39, p. S283, 2006.

[147] E. Gonzalez and R. T. Schoephoerster, "A simulation of three-dimensional systolic flow dynamics in a spherical ventricle: effects of abnormal wall motion," *Ann Biomed Eng*, vol. 24, no. Suppl 1, pp. 48-57, 1995.

[148] A. A. Fontaine, J. T. Ellis, T. M. Healy, J. Hopmeyer, and A. P. Yoganathan, "Identification of Peak Stresses in Cardiac Prostheses: A Comparison of Two-Dimensional: Versus: Three-Dimensional Principal Stress Analyses," *ASAIO journal*, vol. 42, no. 3, pp. 154-163, 1996.

[147] Lacourt, A. (2025). *Patient-specific 4D simulation of blood flow in the left heart under stress using cardiac MRI* (master's thesis). École Polytechnique, Montréal, QC, Canada.